Microfluidic Devices for Single Molecule Detection and On-Chip Pressure Measurement

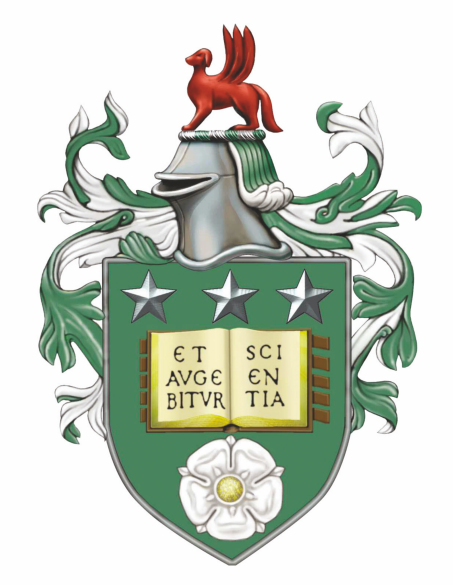

Liam Hunter

School of Physics and Astronomy

The University of Leeds

Submitted in accordance with the requirements for the degree of Doctor of Philosophy

September 2018

Declaration

The candidate confirms that the work submitted is his own and that appropriate credit has been given where reference has been made to the work of others. This copy has been supplied on the understanding that it is copyright material and that no quotation from the thesis may be published without proper acknowledgement.

Acknowledgements

I would like to thank my PhD supervisors, Dr Jung-uk Shim and Prof Stephen Evans for the opportunity to undertake this PhD. Thank you to Jung-uk for guiding me through this project, making sure I came out of the other side and introducing me to the wonderful world of microfluidics. Many thanks to Steve for support and guidance throughout my PhD (as well as being an excellent personal tutor during undergraduate), especially when things began to get difficult.

I have to thank Jinyang Chung especially, working tirelessly alongside me during our first year to tackle what science had to throw at us. I also want to thank Mark Tarn and Grace Porter, as well as being valued members of Dr Shim's research team, they housed me as I wrote this thesis up and I will be forever grateful.

Molecular and Nanoscale Physics has been a brilliant research group to work in for the past 4 years and I thank each and every one of you for making this experience a good one. Whether it's discussing science or enjoying the Fenton on a Friday, I am grateful for all of you, there are too many people to name and stories to tell that I couldn't possibly fit you all in here. To Jamie, Twig, Ellen and Ashley I would say that we had a pretty decent cohort!

Thanks to the wonderful housemates who I have lived with throughout this

PhD, the Knowle Road Crew: Beth, Ellen, Godwin, Simon, Adam, Lucien and Danielle. We've managed to keep each other going.

To my family, who have encouraged me in everything that I do. Mam, Dad, Ashleigh, I wouldn't have made it here without you, thank you.

Abstract

Lab-on-a-chip technologies have been employed in many fields of research. Molecular analysis, microelectronics, chemical and biological assays, cellular studies and environmental monitoring are a few examples in a large and varied list of microfluidic applications. This thesis covers areas from soft matter polymer physics to cancer diagnosis and super resolution microscopy.

The first topic is immunoassay or the detection of cancer biomarkers on chip. The importance of early cancer detection lies in the massive increase in treatment effectiveness the sooner it is administered. In this thesis, the detection of Prostate Specific Antigen (PSA) is investigated using on-chip immunoassay. The components of the immunoassay have been characterised from enzyme reporters to microfluidic droplet generation mechanisms. Single molecules of enzyme can be detected paving the way for on-chip cancer diagnosis.

Many microfluidic devices are manufactured from polydimethylsiloxane (PDMS), a soft polymer. The material has many advantages in microfluidics from optical transparency, low cost, ease of handling, gas permeability and biocompatibility. Due to its elastic properties, PDMS is prone to deformation when placed under high pressures. A novel method of pressure measurement is presented. Along with pressure measurements, the interaction between PDMS and molecules that diffuse into it are studied. The infiltration of molecules changes local mechanical properties which effects the internal pressure of a channel. Raman spectroscopy allows visualisation of the dynamics of material ingress.

Expansion microscopy is a method of encasing a biological sample in a gel matrix, removing the sample and leaving behind a fluorescent ghost image. This gel swells isotropically in water so the fluorescent markers move further apart and can be resolved through super resolution microscopy. This requires delicate handling and the development of devices shown here may assist in containing the entire protocol.

Publications

Refereed Journals

L. Hunter, J. Gala de Pablo, A.C. Stammers, S.D. Evans and J. Shim Pressure-induced Deformation of Microfluidic channels due to Absorption of Mineral oil *Microfluidics and Nanofluidics* - In preparation

T. M. D. Sheard, M. E. Hurley, J. Colyer, E. White, R. Norman, E. Pervolaraki, K. K. Narayanasamy, Y. Hou, H. M. Kirton, Z. Yang, **L. Hunter**, J. Shim, A. H. Clowsley, A. J. Smith, D. Baddeley, C. Soeller, M. A. Colman, I. Jayasinghe. Three-Dimensional and Chemical Mapping of Intracellular Signaling Nanodomains in Health and Disease with Enhanced Expansion Microscopy *ACS Nano* 2019, 13, 2143-2157

List of abbreviations

Abbreviations

AFM	Atomic force microscope
AP	Alkaline phosphatase
BSA	Bovine serum albumin
FDG	Fluorescein di-β-galactopyranoside
HRP	Horseradish peroxidase
IL	Interleukin
LOD	Limit of detection
MITOMI	Mechanically induced trapping of molecular interactions
NOA-81	Norland Optical Adhesive 81
PC	Polycarbonate
PDMS	Polydimethylsiloxane
PET	Polyethylene terephthalate
PMMA	Poly(methyl methacrylate)
PSA	Prostate specific antigen
PVC	Poly vinylchloride
TNF-α	Tumour necrosis factor alpha
UV/Vis	Ultraviolet-visible spectroscopy

Contents

List of Tables

List of Figures

Chapter 1

Introduction

1.1 Microfluidics and micro total analysis systems (μTAS)

Microfluidics is the technology behind the study and manipulation of small liquid volumes confined to channels or structures that are typically tens to hundreds of microns in dimension[4,5]. In 1990, Manz et. al. proposed a device for liquid chromatography whereby the reduction of length scales in the device can theoretically enhance chromatographic separations, speed up electrophoretic separation and shorten transport times of reagents[6]. The inclusion of sample preparation, transport, detection and signal evaluation led to Manz coining the term micro total analysis system (μTAS/microTAS) for such a device. Integrating many components onto these μTAS devices can replace larger, more conventional bench based systems for many of these tasks.

This idea led to the birth of microfluidic technologies and the coining of the term 'lab-on-a-chip'[7]. Lab-on-a-chip technologies have been employed in many fields of research. Molecular analysis, microelectronics[8–11], chemical and biological assays[12–14], cellular studies[15–18] and environmental monitoring[19] are a few examples in a large and varied list of microfluidic applications. The use of microfluidics over conventional larger scale methods leads to a few advantages. The manipulation of small volumes of fluid allow the same operation to be performed that would require much larger volumes in conventional systems. The use of these small volumes, on the scale of nanolitres and below can be advantageous in lowering the cost of reagents as well as reducing risk with the use of potentially dangerous materials[20]. The reduction in the reaction space also adds a benefit to such microfluidic systems. Reagents must diffuse shorter distances when confined in the channels where the dimensions are generally on the order tens to hundreds of microns, increasing reaction probability[21]. Small channels are effective when the reaction is to take place on a surface as reactants have less distance to travel before encountering the surface but also can be replenished quickly while simultaneously flushing the system of previously unused reactants. Heat transfer in confined geometries is also enhanced as high surface area to volume ratios enable rapid heat transfer from or to the reaction or process[21].

The behaviour of fluid flow in microfluidic systems also lends itself to desir-

able experimental parameters. Flow is laminar, lacking turbulence, where the fluid flows in well defined parallel layers with little disruption between them[22]. This leads to precise control of flow and predictable behaviour in a given geometry[23]. Very little mixing takes place in the laminar flow regime, which may be an issue depending on the required reactions (see section 1.1.2.2). This keeps reagents on a defined path throughout the microfluidic device, which can be advantageous for detection positions. An example of this is droplet or particle sorting, where droplets flowing down a channel will encounter a laser spot in a single file fashion[2] enabling no change in set up once experimentation begins.

Many different components can be integrated into a single device allowing for complex procedures to be undertaken without the need for larger equipment. Some components are integrated through geometrical means such as mixers, separators, particle traps[17,24], pumps[25,26], filters[3] and droplet generators[27,28]. Others can be added to the device through techniques such as atomic layer deposition, chemical wet etching or even conventional adhesion techniques (glue or tape) to add features such as electrodes, magnetic components or chemical sensors[29–32]. The integration of many components into a single device increases portability, allowing easy transport to the field or to a patient's bedside for quicker testing. Depending on the required procedure, devices can be passive, only requiring the application of a droplet of sample that is drawn into the device through capillary action to encounter some previously

placed reagents[33–35]. This miniaturisation, ease of use and rapid results acquisition is a motivation for the continued development of microfluidic systems.

Fabrication of microfluidic devices can be fairly low cost once the initial infrastructure is in place, which can lead to rapid replication of devices once the design has been finalised. The rapid prototyping of devices gives an advantage whereby the production of multiple prototypes can be done in parallel, for example, multiple designs incorporated onto one photomask or multiple designs drawn by laser writing (see section 2.2 for a thorough explanation). This allows for many variables such as channel size or droplet nozzle width to be assessed. Once a final design is complete, mass production can be relatively simple. In terms of commercialisation, there are often issues with scaling up production of a particular solution, which can lead to further troubleshooting. With microfluidic devices it is fairly simple to multiplex devices through parallel connections to increase throughput[36].

1.1.1 Microfabrication

The material choice for a microfluidic chip depends on the desired properties and function of a device. Early development of microfluidic systems used silicon as a substrate and used techniques similar to that used in semiconductor fabrication[37]. These devices require hazardous chemical processes and are generally difficult to handle due to the brittle nature of silicon. Glass is a popular

choice due to its optical transparency and resistance to chemicals[29]. The manufacture of glass chips uses photolithography techniques (described in detail in section 2.2) after which the glass is etched to form the channel depths[38–40].

Thermoplastics such as PMMA (Poly(methyl methacrylate), polycarbonate (PC), polystyrene, polyethylene terephthalate (PET) and polyvinyl chloride (PVC) can be used to create devices through moulding, although there are several disadvantages. The moulds required are generally metal or silicon meaning multiple changes in device design during prototyping is difficult (although mass production is easier). These plastics are incompatible with most organic solvents and not permeable to gas, which makes them unsuitable for applications such as long term cell culture where gas exchange is required. Bonding of thermoplastics can be difficult but is achieved through glue assisted bonding or by mechanical clamping of channels to a manifold[41].

Soft polymer elastomers consist of crosslinked polymer chains, which exhibit elastic properties when put under mechanical stress[36]. The most popular of these is polydimethylsiloxane (PDMS)[29,36,38,42,43]. PDMS is low cost and easy to fabricate with, making it a staple in many microfluidic labs. The liquid polymer cures between 40 - 70 °C and is cast using impression moulding capable of copying nanometre resolution templates[29]. After casting (a technique named soft lithography, described in section 2.4) the device can be reversibly or irreversibly bonded to a substrate (usually glass) by simple contact or exposure

to oxygen plasma respectively. Multilayer channels can be created by stacking PDMS mounds on top of each other with cylindrical connectors to connect different layers[44]. If the membrane between multiple layers is sufficiently thin, the high elasticity of PDMS can be used to create valve structures that actuate through the introduction of pressure into a channel. These valves have small dead volumes and can be very densely packed onto a chip[45–47].

1.1.2 Microfluidic Flow

1.1.2.1 Laminar Flow and Reynolds Number

Fluid flow in microfluidic devices is laminar whereas in bulk systems the flow is predominantly turbulent[22]. This turbulence enable fluids to mix together without external influence. The mixing in laminar flow only occurs due to diffusion between streams of fluid in contact with each other. Laminar flow occurs when viscous forces dominate the inertial forces in a system[21,48–51]. To determine whether a flow is laminar or turbulent, the Reynolds number can be calculated which is a ratio of the inertial forces to viscous forces in a flow.

$$Re = \frac{\rho u D_H}{\mu} \tag{1.1}$$

where ρ = density (kg m^{-3}), u = average fluid velocity (m s^{-1}), D_H =

A comparison of materials for microfluidic device production, adapted from Ren et al. [37]

Property	Silicon/Glass	Soft Polymer	Thermoplastics	Paper
Young's Modulus	130-180/50-90	0.0005	1.4-4.1	0.003-0.0025
Fabrication Technique	Photolithography	Casting	Thermomoulding	Photolithoigraphy/Printing
Minimum Channel Size	< 100 nm	$< 1\mu$m	100 nm	200 μm
Multilayer ability	Hard	Easy	Easy	Easy
Thermostability	Very High	Medium	High	Medium
Solvent Compatibility	Very High	Low	High	Medium
Optical Transparency	No/High	High	High	Low

Table 1.1: A comparison of materials for the fabrication of microfluidic devices.

hydraulic diameter of the channel (m) and μ = fluid viscosity (kg m^{-1} s^{-1}). The hydraulic diameter of a channel depends on the area of the channel and its wetted perimeter[48] shown in equation 1.2

$$D_H = \frac{4A}{P} \tag{1.2}$$

At Reynolds number less than 2300, flow is predicted to be laminar and generally microfluidic devices operate at Reynold numbers less than 1[22,52–54].

Diffusion of molecules is determined with the Einstein-Smoluchowski equation shown in equation 1.3[21,55].

$$x = \sqrt{2Dt} \tag{1.3}$$

where x = diffusion distance (m), D = diffusion coefficient (m^2s^{-1}) and t = time (s). Diffusion arises due to concentration gradients of molecules within a system. An example of the importance of this relation in regards to microfluidics can be seen in the diffusion of haemoglobin in water. Haemoglobin has a diffusion coefficient D = 7 x 10^{-7} m^2s^{-1} therefore takes 10^6 s to travel 1 cm but only 1 second to diffuse 10 μm[21]. In a microfluidic channel, the high concentration of fluid compared to the surrounding material causes diffusion into that material and, due to the small length scales characteristic in microfluidic

devices, can be a significant effect [22].

The resistance of a microfluidic channel can be shown in a way analogous to electronic circuitry [56]. Ohm's law states that R=V/I for resistance, voltage and current which is analogous to a microfluidic flow described by

$$Q = \frac{\Delta P}{R} \tag{1.4}$$

where Q = volumetric flow rate (m^3s^{-1}), ΔP is the pressure drop of a channel from beginning to end (Pa) and R = hydraulic resistance of the channel ($Pam^{-3}s$). When analysing microfluidic designs, these analogies are useful as series and parallel rules still apply. Series channel resistances are summed and parallel channels calculate resistance with:

$$\frac{1}{R_T} = \frac{1}{R_1} + \frac{1}{R_2}... \tag{1.5}$$

The hydraulic resistance of the channel is dependent on the geometry of the channel and is derived from analytical solutions to the Navier-Stokes equation [22]. The resistance of a circular channel is given in equation 1.6 where μ is fluid viscosity (kg m^{-1} s^{-1}), L is the length of the channel (m), and r is the radius (m). Generally, when manufacturing microfluidic devices, the resulting channels are rectangular. The resistance of a rectangular channel is given

equation 1.7[49] where h is the channel height and w the width (This equation is valid for channels where w $\gg$ h).

$$R = \frac{8\mu L}{\pi r^4} \tag{1.6}$$

$$R = \frac{12\mu L}{wh^3(1 - 0.63h/w)} \tag{1.7}$$

1.1.2.2 Mixing on chip

When performing reactions on chip, it may be necessary to enhance the mixing within a microfluidic channel. Turbulence only occurs at Re $>$ 2000 and requires high flow rates to achieve[48]. To improve the mixing performance of channels, serpentine sections can be added. Song et al.[57] observed the mixing in straight and serpentine channels with a 3 phase water droplet in a polyfluorodecaline (PFD) stream. One water stream contained a solution of ferrothiocyanate as a red dye. The plugs were formed at a t-junction where the shear force of the PFD broke the water solution off into 100 μm long plugs. When the channel is straight, the plugs encounter steady recirculating flow due to interaction with the channel wall but does not mix between phases. When a serpentine channel is used, the offset in symmetrical forces from the wall due to curvature causes the plug to be thoroughly mixed. The serpentine was injected with a

calcium sensitive fluorescent dye and a calcium solution and imaged showing fluorescence evolution over time[57]. This geometry was used in immunoassay experiments in this thesis to provide reactant mixing.

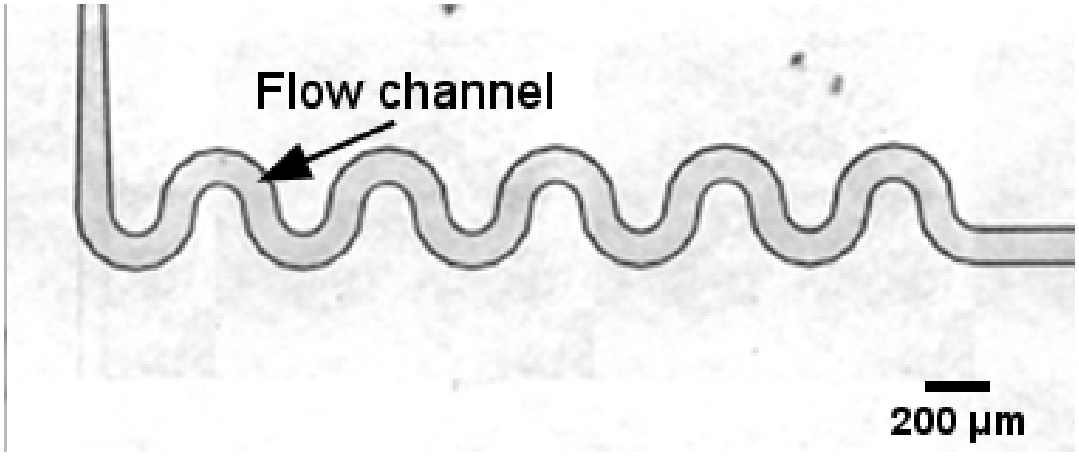

Figure 1.1: A serpentine from the immunoassay device used in this thesis. This mixer is placed directly after a droplet generation nozzle to evenly distribute reactants.

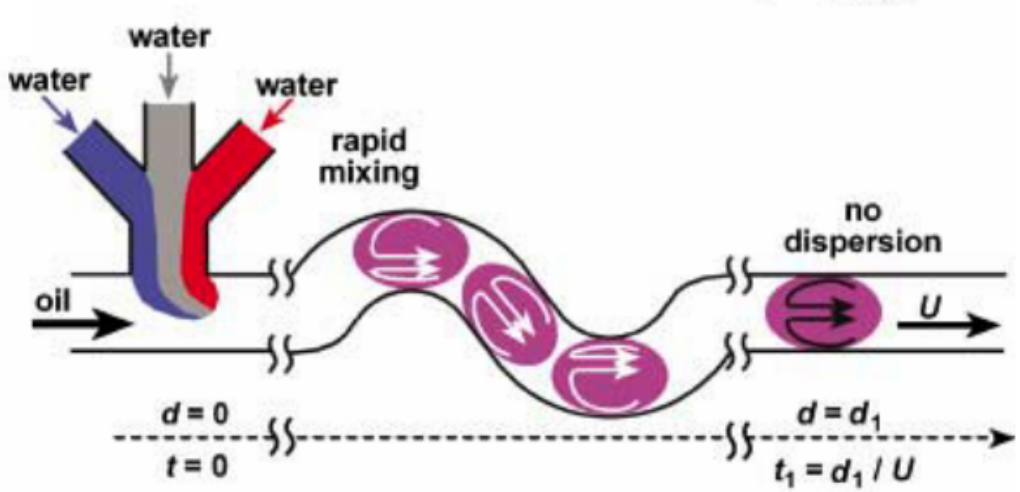

Figure 1.2: A serpentine causes offset in circulating flows within droplets causing mixing. Adapted from Song et al.[57]

1.1.2.3 Microfluidic Valves

Microfluidic valves were described in section 1.1.1 and are useful for controlling flow patterns within a microfluidic device. The valves are fabricated from multiple layers of PDMS containing channels. Shown in figure 1.4, the horizontal flow channel lays above a perpendicular vertical channel. Figure 1.5 shows the working principle of a microfluidic valve from a side view. Spin coating the PDMS onto the bottom layer allows fine control of the membrane thickness between the channels to tune the valve properties. Unger and Quake developed the method of preparing these valves and demonstrated their blocking abilities[45]. In the microfluidics community these features have become known as "Quake Valves". The valves are actuated by a pressurised air supply on the order 100 kPa and close in a time on the order of 1 ms as the thin membrane deforms up into the channel above. Rectangular valves may not create a perfect seal with the channel above but are sufficient for the diversion of particles or droplets within microfluidic systems. Sequential valves along a channel were shown to act as a peristaltic pump on chip by selective activation of a sequence of valves. The ability to form high density areas of valves makes then favourable for large scale and complex systems such as that displayed by Thorsen et al.[47]. The large system was analogous to a binary computer system where individual droplets of water were accessible for transfer between trap areas of merging with other droplets.

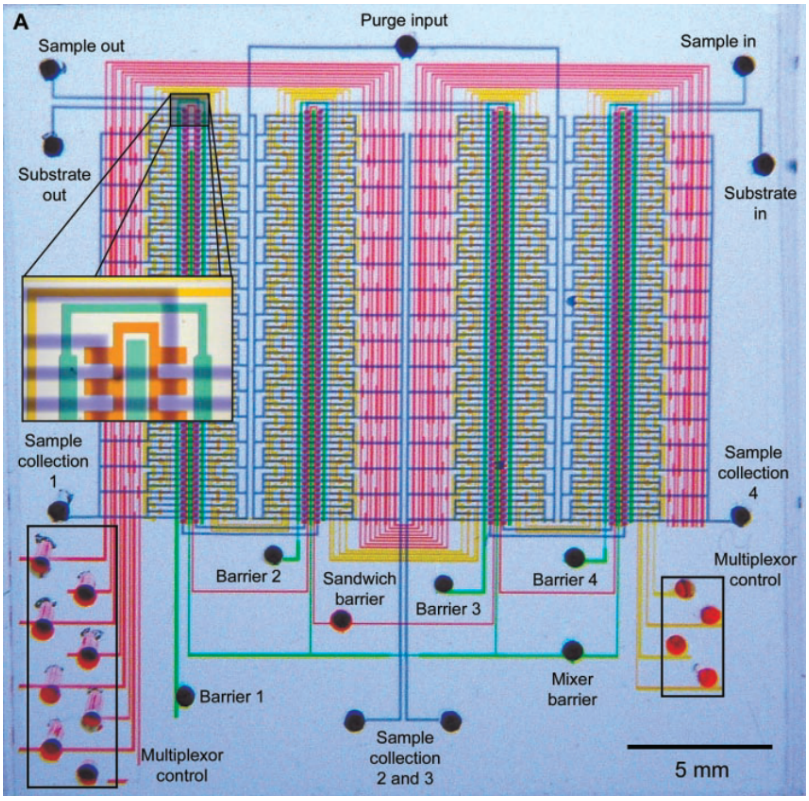

Figure 1.3: Combining large banks of microfluidic valves allows for the movement of discrete liquid plugs around the chip. Shown is a chip designed to mimic computer logic using different colours to represent logical states. Taken from [47].

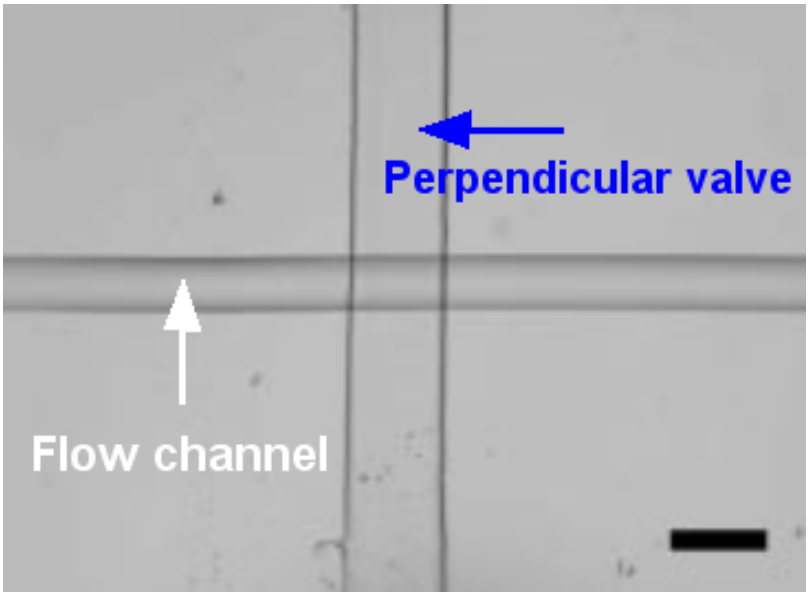

Figure 1.4: The layering of soft polymer PDMS microfluidic channels with 15 μm membranes between allows for the formation of flow control valves. Scale bar = 200. Taken from μm[45]

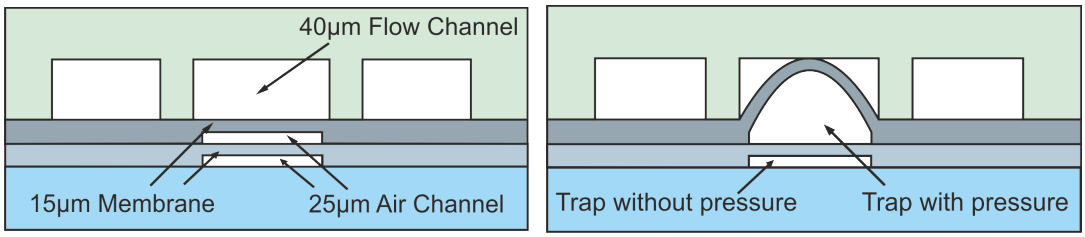

(a) **(b)**

Figure 1.5: a) A microfluidic valve system in a 3-layer PDMS device. b) when air is injected, the membrane deforms and blocks the channel above.

Although PDMS is a common choice for construction of microfluidic valve structures, alternative materials such as 3D printed resins[58] and acrylic glass[59] have been shown to operate on the same principle. In a study by Guevara-Pantoja et al.[59] poly(ethylene diacrylate) was 3D printed at a thickness between 10 - 25 μm and the application of 20 - 40 kPa of pressure was sufficient to close the valve. These valves were also shown to be integrated into large scale devices by designing an array of 64 valves similar to the Thorsen et al. system[47] and building peristaltic pumps from multiple valves. Milling of acrylic glass to 100 μm membranes were suitable to be actuated by 17 kPa of pressure to seal channels.

1.2 Droplet Microfluidics

The final microfluidic component to be described is the droplet generating nozzle. Droplet microfluidics differ from continuous flow systems in that they are used to generate uniform, discrete volumes of fluid within a second immiscible fluid[60]. Generation of monodisperse droplets in the nanometre to micrometre diameter range can be achieved at rates up to MHz[3,61,62].

The generation of droplets is governed by the capillary number, Ca. This value describes the relative importance of viscous forces (shear stress) against the interfacial tension between the two immiscible fluids at the interface. Ca

predicts the droplet formation regime under which the discontinuous phase is pinched off into the continuous phase[63].

$$Ca = \frac{\mu v}{\gamma} = \frac{\mu Q}{\gamma A} \tag{1.8}$$

Equation 1.8 describes the capillary number where μ is the fluid viscosity (kg m^{-1} s^{-1}), v is the fluid velocity (ms^{-1}, γ is the interfacial tension (N m^{-1}), Q is the volumetric flow rate (m^3s^{-1}) and A is the channel area (m^2). Ca is calculated for both of the phases however the continuous phase plays a greater role in defining the regime[64]. The Weber number (We) defines the relative importance of inertial forces against interfacial tension acting across the interface of two immiscible fluids and is given in equation 1.9 where d_0 is the diameter of the discontinuous phase (m). The Weber number is typically calculated in reference to the discontinuous phase. The Weber number aids predictions for geometries where the inertial forces are no longer negligible (We $\geq$ 1). However, in devices described in this thesis, We $<$ 1 therefore Ca is considered[51,53,65].

$$We = \frac{\rho d_0 Q^2}{\gamma A^2} \tag{1.9}$$

There are three main geometries of droplet generation in microfluidics, coax-

ial, flow focusing and cross flow (T-junction) each of which are shown in figure 1.6. Coaxial flow is set-up so the inlet of the discontinuous phase is inside a channel of the continuous phase, this can be achieved by inserting a capillary into a wider channel. Flow focusing joins the two phases at a geometric restriction or nozzle in a common flow direction and cross flow employs a T-junction where the discontinuous phase is introduced perpendicular to the continuous phase.

In a T-junction, the discontinuous phase enters the channel of the continuous phase and an interface is formed. The shear forces generated by the continuous phase and pressure gradient cause the discontinuous phase to elongate into the main channel until the elongation thins enough for breakup to occur. Droplet size is controlled by relative flow rates, channel dimensions and relative fluid viscosity[60]. In flow focussing, the phases are forced through a local constriction in geometry[3,60,66,67]. The discontinuous phase is symmetrically sheared by the continuous phase enabling controlled and stable droplet generation[60]. A flow focussing nozzle creates a single point of high shear at the narrowest region of the nozzle in which all droplets are produced. This forms uniform monodisperse droplets.

Figure 1.6 shows the different regimes depending on the Ca. Low Ca predicts the dripping regime where the discontinuous phase is held at the nozzle and packets of the discontinuous phase rapidly shear off the tip. A high Ca

predicts a jetting regime, where the continuous phase travels through the nozzle and destabilises into droplets a distance downstream of the nozzle. This Rayleigh-Plateau instability can be explained in several ways. One is that the large surface area of the jet is thermodynamically unfavourable so to reduce its energy, the surface tension drives the formation of droplets with the same total volume but lower surface area[68]. A second description uses the Laplace pressure, or pressure between two phases due to the presence of a curved interface. As the jet travels down the channel, the curvature and Laplace pressure increases. This pressure squeezes the jet to form droplets[68]. At higher Ca the interfacial forces are no longer overcome and the phases exist in a stable, laminar coflow regime[69]. When using a flow focusing geometry, capillary numbers of Ca = $< 10^{-1}$, $> 10^{-1}$ and $\gg 10^{-1}$ predict dripping, jetting and coflow respectively[51].

The co-flow mechanism can be used to generate double emulsions using a microfluidic device[68,70]. Glass capillaries can be nested within each other to produce oil-water-oil (O/W/O) or water-oil-water (W/O/W) emulsions. The layout of such a device is shown in figure 1.7. These double emulsions have been shown to be useful in the formation of spherical hydrogels[71] and protein crystallization[72]

The stability of droplets in the continuous phase can be improved through the use of surfactants[73]. Droplets without interfacial stabilisation will coalesce

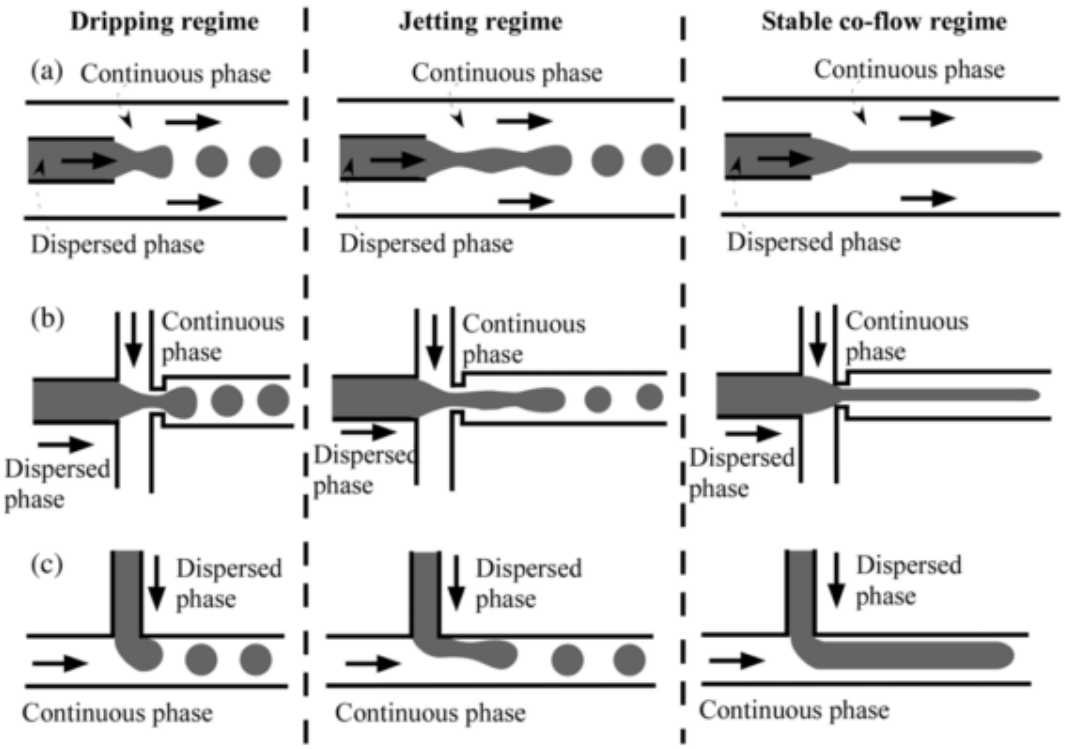

Figure 1.6: Microcapillary generation of double emulsions uses two co-flow jets. The outer fluid is immiscible with the middle and the middle with the inner.

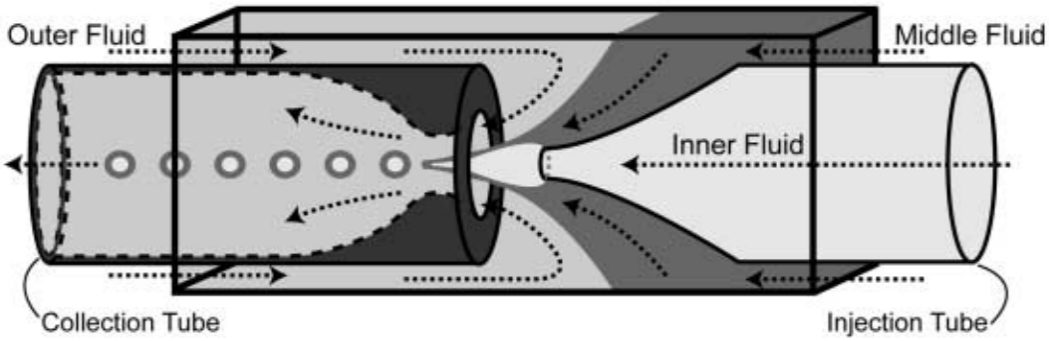

Figure 1.7: Capillary number effect on droplet formation regimes of the three most common droplet generation geometries, (a) coaxial, (b) flow focussing and (c) T-junction. Taken from [51]

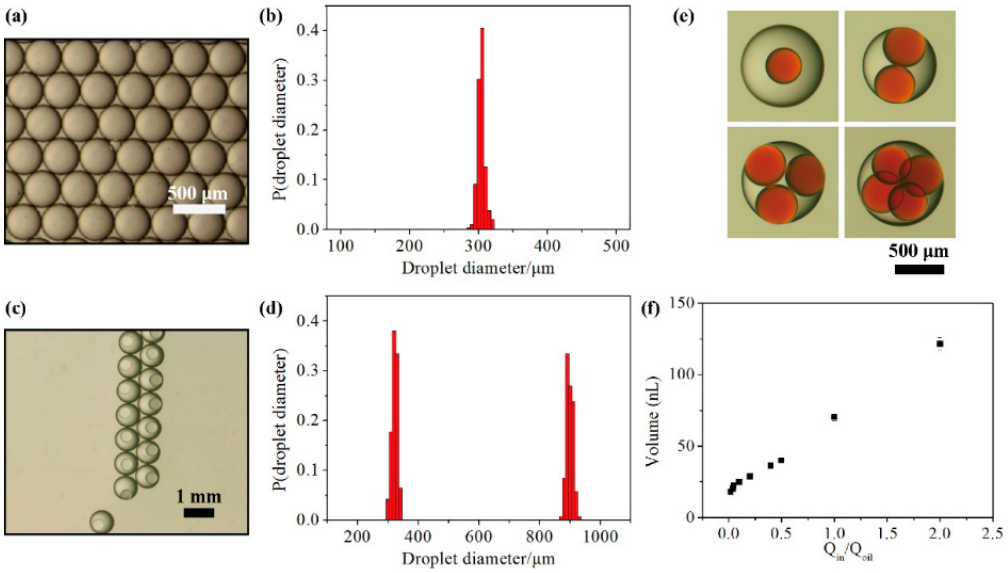

Figure 1.8: From Zhu et al.[72], generation of W/O/W emulsions. a,c) Optical microscopy images of single and double emulsions produced using FC-40 fluorinated oil and DI water. b,d) Performance of the nested capillary device used to generate the single and double emulsions. e)Double emulsions are tunable to generate single or multi core droplets. f) The ratio of inner aqueous flow rate to middle oil phase flow rate causes volume variation of the innermost phase.

on contact and form larger droplets. This is a disadvantage when trying to generate discrete monodisperse reaction vessels when high droplet densities are required[3]. Surfactants are amphiphilic molecules with affinities for different immiscible phases. This drives the molecules to the interface and the surface tension is decreased[73]. The decrease is given by the Gibbs adsorption isotherm for dilute solutions:

$$\Gamma = -\frac{c}{RT}\frac{d\gamma}{dc} \tag{1.10}$$

where Γ is the surface concentration, c is the surfactant bulk concentration, γ is the surface tension, R is the gas constant and T temperature. Common surfactants include Triton- X-100 or SDS in silicon oil[74–76], Span 20/80 in hydrocarbon oils[77–81] and fluorosurfactants (block chain copolymers such as PEG – PFPE) in fluorinated oils[3,73,82–85]

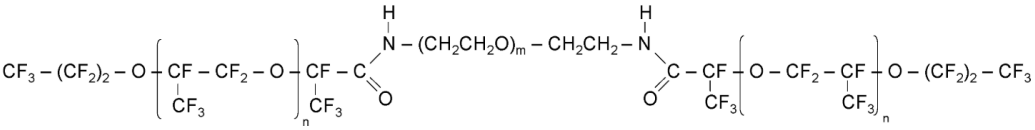

Figure 1.9: Block co-polymer surfactant used in the droplet formation experiments of this thesis, Krytox 157 FSL Jeffamine ED-600 disalt

Droplet microfluidics has a wide range of applications as droplets are used as high throughput reaction vessels for biological[86–88] and chemical[89–94] analysis. Biological applications include single cell analysis[95–101] where droplets containing cells can have genome analysis, cell matrix interactions and biomarker pro-

duction observed[16]. The detection of biomarkers and more specifically cancer biomarkers are the motivation behind chapter 3 of this thesis.

Droplets within microfluidic devices can be manipulated depending on their contents[2,102–104]. Droplets can be sorted by size or through some external field such as electrophoresis, examples of which are shown in figure 1.10. These sorting methods can allow for concentration of targets or removal of unwanted droplets within a system. Another example of droplet sorting involves the measurement of a fluorescent product within droplets as the pass a laser and if a detectable signal is read, an electrode is activated diverting that particular droplet elsewhere on chip[2]. An example of sorted droplets is shown in figure 1.11.

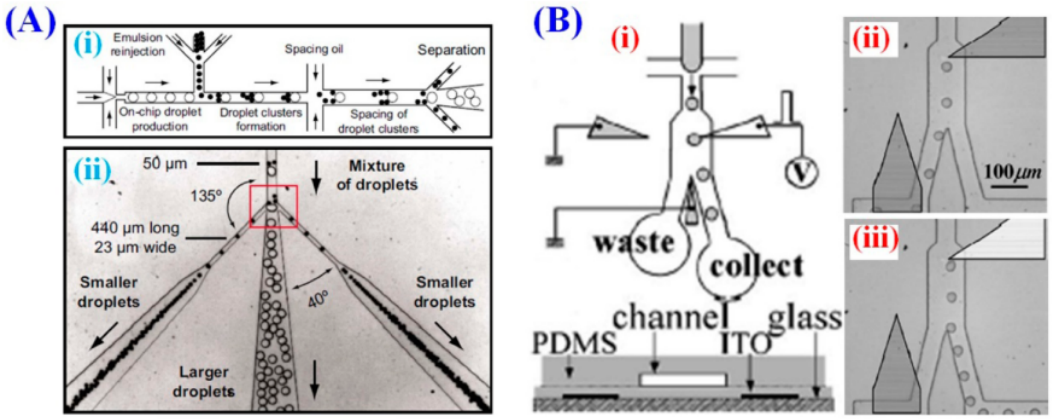

Figure 1.10: Droplet sorting in a microfluidic device. a) Passive sorting can be achieved where droplets arrange by size in the channel due to the flow profile. b) Active sorting through electrophoresis where the electric field is inactive ii) and active iii). Taken from[1].

The trapping of droplets is a useful tool for time-dependant observation of a process as well as keeping track of particular droplets. Shown in figure 1.12,

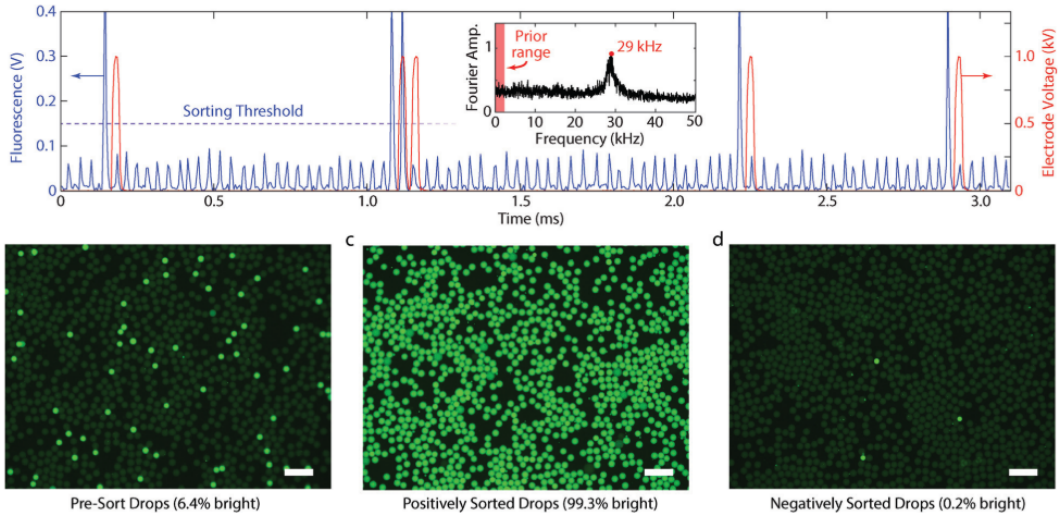

Figure 1.11: Active droplet sorting in a microfluidic device. a) A large increase in fluorescent signal causes the activation of an electrode to divert a droplet. Droplets before b) and after c,d) sorting show that on 0.2% of rejected droplets have a positive fluorescence signal. Taken from [2].

single droplets can be trapped within pockets built into a channel. Large arrays of these traps allow single occupancy traps with the possibility of reversing the flow to release them [1].

Larger scale traps can trap many droplets in a monolayer and allow observation over a number of minutes to hours [3]. In figure 1.13 from Shim et al. 10^4 droplets of diameter 4 μm are trapped in a 300 μm trap that uses a monolithic microfluidic valve to keep the droplets contained.

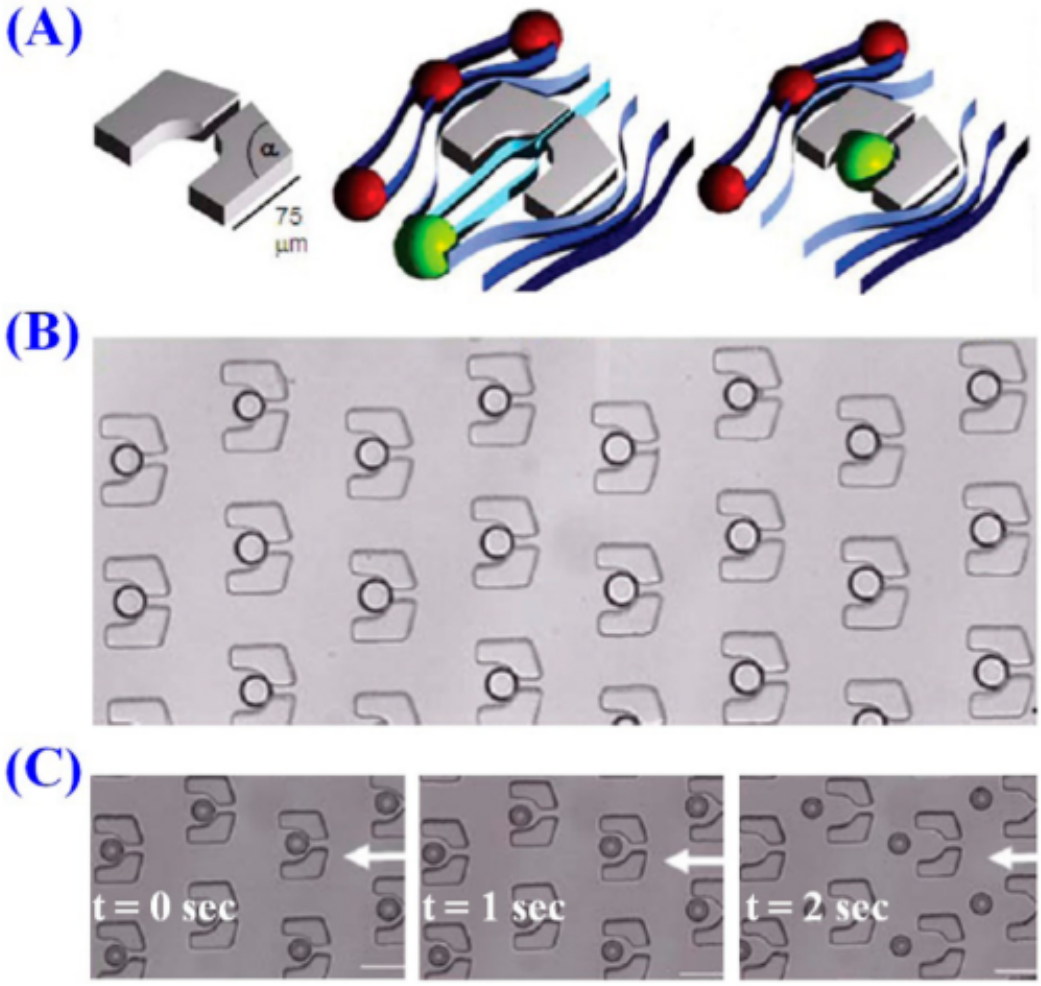

Figure 1.12: Droplet trapping in a microfluidic device. a) The flow profile around a trap encouraged droplets to enter. Once occupies the remaining droplets flow around. b) Microscope image of a trap array showing single droplet occupancy. c) Droplets can be released by inverting flow within the array. Taken from [1]

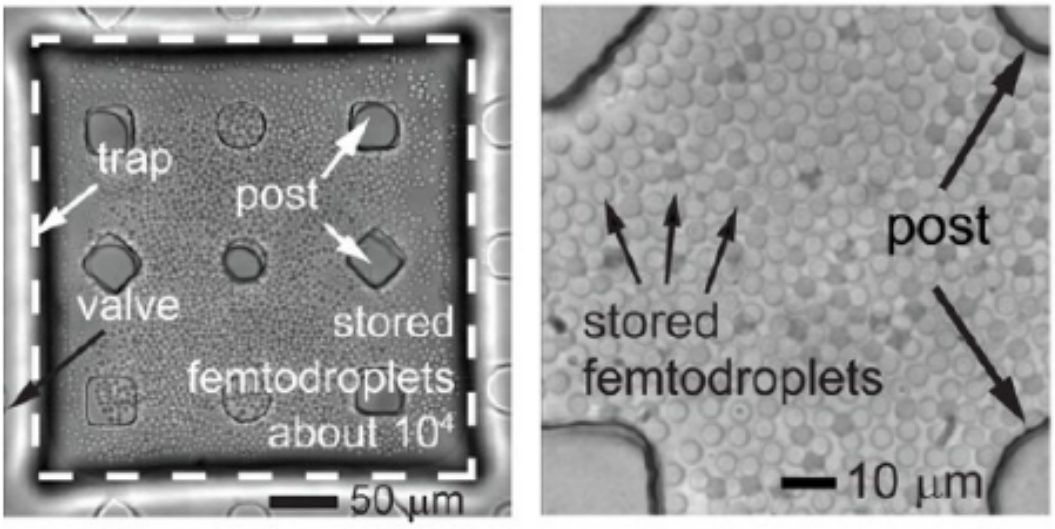

Figure 1.13: 10^{4} droplets are trapped in a monolayer in a 5 μm thick channel. These droplets were trapped for 10 minutes to observe the formation of a fluorescent product. Taken from [3]

1.3 Immunoassay on Chip

Cancer is a group of diseases that are characterised by abnormal growths of cells and tissue which can invade healthy organs and cause death [105]. The need to detect and diagnose such conditions during early stages is important in order to apply effective curative interventions before the disease progresses too far [106]. Imaging techniques are useful for diagnosing these abnormal growths, or tumours, but rely on the size being sufficient to detect, and scans can also be interpreted as a false positive [107]. Blood tests have become more popular due to the increasing sensitivity of screening for cancer biomarkers [31]. A cancer biomarker is defined as a substance or activity that can be objectively measured and evaluated as indicator for a normal biological process, pathogenic process or pharmacological response to a therapeutic environment [108]. Can-

cer biomarkers are present in tumour environments and can be a wide range of biological molecules including cell receptors, enzymes, proteins, DNA/RNA, transcription factors and other small metabolites[109]. Detection methods of cancer biomarkers traditionally include electrophoresis, surface plasmon resonance (SPR)[110–112], surface enhanced Raman spectroscopy (SERS)[113–117], polymerase chain reaction (PCR)[118] and enzyme-linked immunoassay assay (ELISA)[34,35,119,120].

Microfluidic systems for bioanalytical applications have been developed rapidly over the last decade and bridge the gap between simple use lateral flow type systems and laboratory based analytical techniques[87]. Lateral flow systems are generally paper based and only require the application of a sample to a sample pad. Upon application, the sample migrates along the paper through capillary flow towards a test area loaded with an indicator. A classic example of a lateral flow device is a pregnancy test, where urine is introduced to the sample pad which migrates towards an area containing antibodies for the hormone human chorionic gonadotropin (hCG) that have been conjugated with coloured beads. The conjugated antibodies bind to the hCG, if present, in the sample and migrate to a "Test" line where they will bind to a secondary antibody for hCG. The accumulation of complexes of hCG and colour-conjugated antibodies give rise to the band seen on a positive test. Lack of hCG in the urine sample causes no accumulation of antibody at the test line and therefore

a negative test[121]. A schematic of this process is shown in figure 1.14. The advantages of lateral flow devices include the rapid readout time, ease of use, single step operation, portability and qualitative results. The tests can rapidly indicate a positive test for a sample analyte but lateral flow devices generally struggle to yield qualitative results, especially at low concentrations[121].

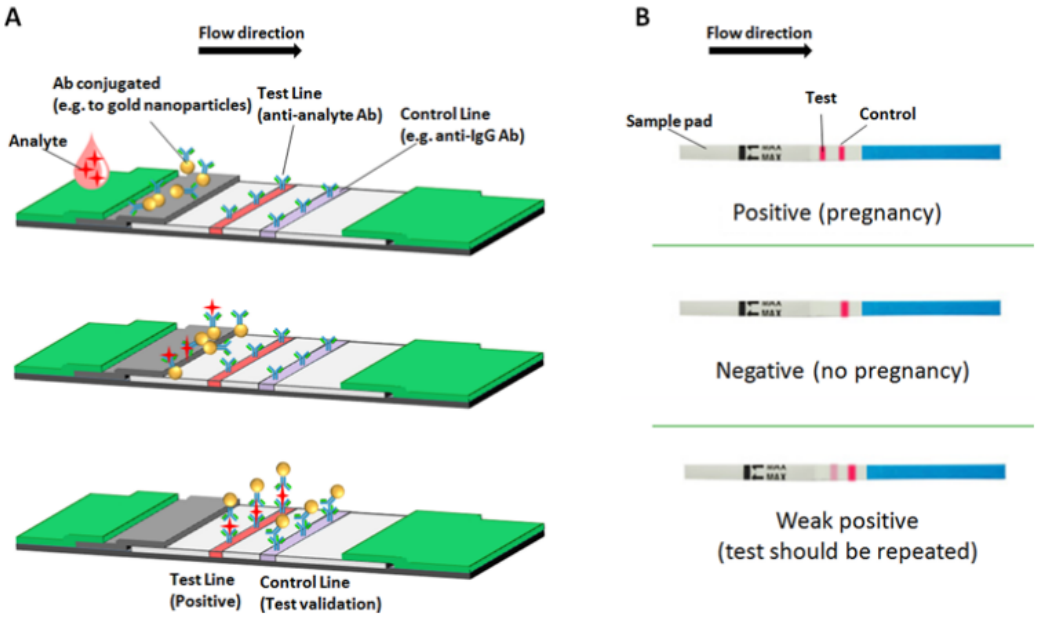

Figure 1.14: A) Schematic of a lateral flow assay. Top: a sample is added to the sample pad and migrated towards the conjugated antibodies through capillary action. Middle: Target analyte binds with the conjugated antibodies and (bottom) migrates to the test line where bound targets are captured. B)This lateral flow assay is applicable to pregnancy tests where possible outcomes are shown. Taken from[121].

Building on these simple lateral flow assays, microfluidic devices have developed to provide sensitive quantitative measurement of analyte concentrations. The majority of these developments use a heterogeneous sandwich immunoassay for biomarker detection. ELISA is considered a gold standard for the detection

of proteins in physiological samples[122] and is used to detect a wide variety of cancer biomarkers[123,124]. In traditional bulk ELISA methods, a signal is generated (usually colourmetric or fluorescent) to indicate a concentration of target analyte bound to a signalling mechanism[119]. Colourmetric assays use the conversion of a substrate from colourless to a coloured molecule through enzyme activity. The intensity of the produced coloured molecule is then measured through absorbance spectroscopy techniques[119]. Figure 1.15 shows the schematic of an ELISA system. A capture antibody with affinity for the target biomarker is bound to a surface, usually a 96 well plate. The target sample is then introduced where the biomarker binds to the antibody. The wells are washed and a secondary detection antibody is introduced which also binds to the target analyte. This second antibody is tagged with biotin so that when a solution of streptavidin conjugates enzyme is introduced, they bind, forming an immunocomplex. Introduction of a substrate for the enzyme to react with will result in the production of an observable product that can be measured by absorption and fluorescence. The most common detection enzymes used are horseradish peroxidase (HRP), alkaline phosphotase (AP) and β-galactosidase (β-Gal)[119] as a large range of substrates are available depending on the detection method. Detectable concentration limits using these enzyme systems is between 25 - 200 ng ml^{-1}[119]. There is still an unmet clinical need for the detection of biomarkers of neurodegenerative diseases and cancers that are present in biological fluids at concentrations of 10^{-12}-10^{-16}M[106,125]. This section will

discuss examples microfluidic based immunoassays and discuss the different techniques used with their advantages and disadvantages. A summary of the performance and format of microfluidic immunoassays is provided in table 1.2.

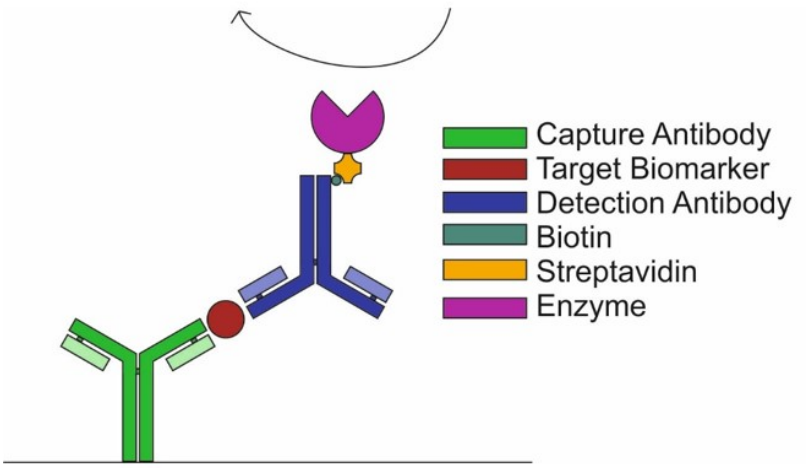

Figure 1.15: Schematic of sandwich ELISA. A capture antibody bound to a surface captures the target biomarker after the introduction of a sample (blood, saliva etc.). A detection antibody binds to the target and provides a binding site for the reporting mechanism, here shown as a streptavidin conjugated enzyme. The enzyme turns over a substrate to develop a detectable signal.

To develop a feasible microfluidic platform for biomarker detection, it is important to determine the limit of detection (LOD). The LOD describes the minimum concentration of target analyte that can be distinguished from the background signal of the detection method. The minimum signal that is defined as detectable has a signal to noise ratio of 3 which is equivalent to a blank signal + 3σ where σ is the standard deviation of the blank signal. This LOD is crucial when developing assays for different disease biomarkers where clinically relevant concentrations can differ by several orders of magnitude[123,126]. The blank measurement of an assay can vary depending on the sample type and

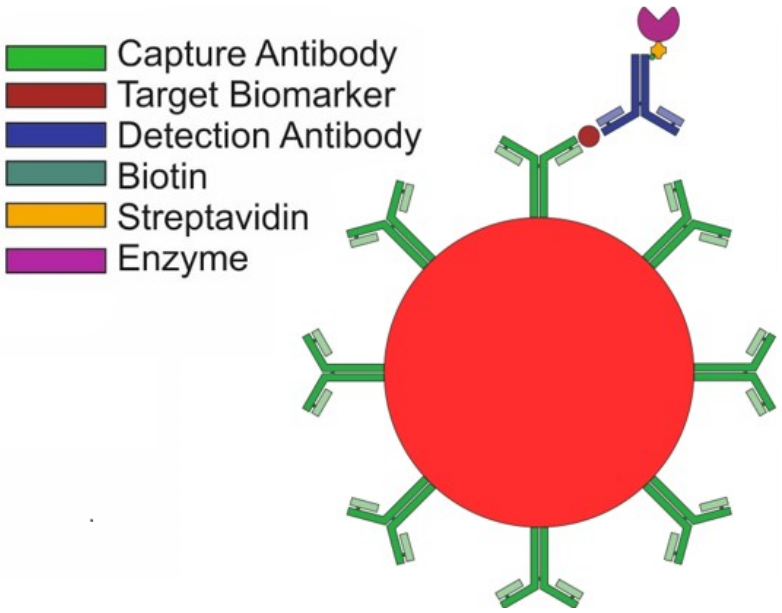

Figure 1.16: Schematic of sandwich ELISA where an immunocomplex is formed on a bead as opposed to on a surface in traditional ELISA.

composition due to the presence of other biological molecules other than that of interest in the sample matrix. Interactions between the biomolecules present and the assay sensing components within a device can cause unwanted positive results[127].

Sandwich immunoassays begin with the immobilisation of an antibody to a solid phase followed by the blocking of remaining binding sites. In a microfluidic device, it is important to consider the surface characteristics of the devices being designed. The simplest method of binding antibodies is through a passive adsorption[87] where non-polar regions of the antibody bind to hydrophobic surfaces such as plastic. This method is used in the traditional well plate based assays[128]. A simple microfluidic approach to this method shown by Fan et al. immobilized antibodies in strips on a PDMS surface and intro-

duced samples perpendicular to these strips to form an array of squares where chemiluminescence could be observed[129]. A schematic is shown in figure 1.17. This system detected α fetoprotein, a biomarker for hepatocellular carcinoma, at concentrations of between 12.5 - 200 ng mL^{-1}. This method is simple to perform but is limited in terms of sample number and concentration limit, in this study 36 samples were observed. A similar approach by Wang et al. (shown in figure 1.18) measured testosterone concentrations between 0.03 and 30 ng mL^{-1} [130]. In this study, the antigen was bound to the surface before the addition of a primary and secondary labelled antibody. This is known as indirect ELISA[119].

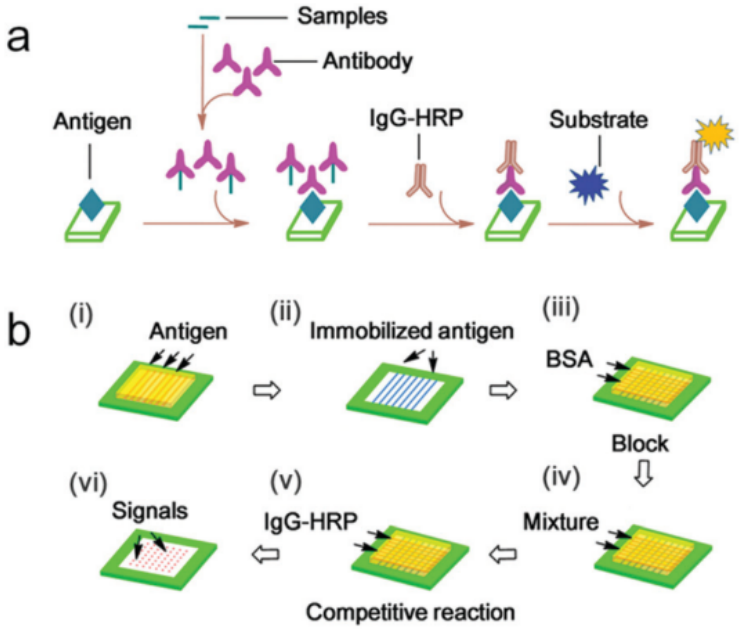

Figure 1.18: a) The formation of an indirect ELISA where antibodies bind to an immobilised antigen. b) Similar to Fan et al.[129], stripes of immobilized molecules are formed before the introduction of detection molecules perpendicular creates an array of signals. Taken from[130].

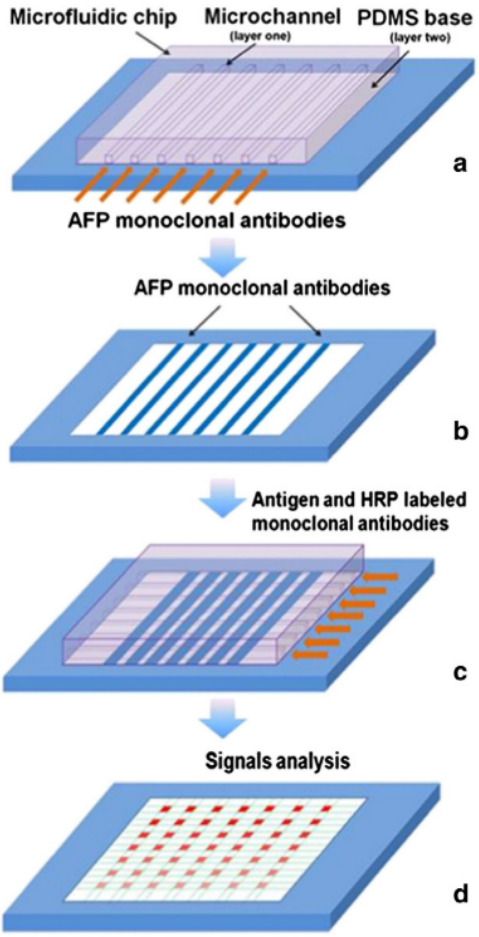

Figure 1.17: Schematic of an α fetoprotein immunoassay. a) Antibodies are immobilized on a PDMS surface using a row of channels as a guide forming antibody strips b). The PDMS guide is removed, washed and placed perpendicular to the strips c) where antigen and secondary antibodies are injected. The enzyme substrate for HRP was added and chemiluminescent signal measured d). Taken from [129]

Chip Material	Target Analyte	Sample Type	Time	Detection Range	Ref
PDMS	Testosterone	Serum & Urine	100 min	0.03-30 ng mL^{-1}	[130]
PDMS	α Fetoprotein	Commercial	N/A	12.5-200 ng ml^{-1}	[129]
PDMS	TNF-α	Commercial	N/A	N/A	[131]
PDMS	Multiple protein	Cell lysates	N/A	Dynamic	[132]
PDMS	Protein nucleic acids	Cell lysates	20 min	Dynamic	[133]
PDMS	HIV Oligonucleotide	Serum	75 min	Dynamic	[134]
Glass	IgG	Commercial	N/A	0-68 ng ml^{-1}	[135]
Paper	IgG	Serum	30 min	Dynamic	[136]
PMMA & Paper	Hepatitis B antigen	Serum	$<$ 60 min	3.4 x 10^2 - 3.4 x 10^8 pg ml^{-1}	[137]
PDMS	β-galactosidase	Commercial	8 mins	$>$ 10 nM	[138]
Optical Fibres	β-galactosidase	Commercial	Not stated	72 fM	[139]
Optical Fibres	TNF-α & PSA	Plasma	6 hours	2.5 fg mL^{-1} TNF-α & 0.014 pg ml^{-1} PSA	[126]

PDMS	PSA	Commercial	30 min	2 aM - 100 fM	[140]
PDMS	PSA	Commercial	10 min	1.2 - 140 pg mL^{-1}	[3]
PDMS	anti Ebola IgG	Commercial	15 mins	10 nM - 100 fM	[88]

Table 1.2: A comparison of material, sample type and performance of microfluidic immunoassay systems.

The initial step for designing a microfluidic droplet based ELISA is to develop the detection method. Microfluidics offers an advantageous detection platform to detect biomarkers at lower concentrations than traditional ELISA[31,141]. At low biomarker concentrations, the observed signal is so diminished that it cannot be distinguished from background noise. This can be visualised when considering tens to hundreds of target biomarkers within a sample. In a 96 well plate, the volume is typically around 300 μl and such small numbers of enzyme product molecules within this volume are not sufficient for detection. The use of nano-femtolitre droplets provide smaller volumes where these small number of molecules are contained generating a higher effective concentration. Detection can be achieved either in flow[142–144] or in discrete reaction units. Rondalez et al. developed a microfluidic device with 5 μm wide hemispherical chambers that were simply placed on a slide containing enzyme solution[138]. A schematic can be found in figure 1.19 This created discrete volumes of 1.4 fl on the slide surface. Mixtures of horseradish peroxidase enzyme (HRP) and β-galactosidase were mixed with a fluorescent substrate and trapped in the wells. Continuous monitoring of a selection of droplets over time led to three bands of intensity increase indicating the presence of zero, one or two enzymes within. This is an important feature as the detection of single enzymes leads to the possibility of single biomarker detection through ELISA.

The advantage of this system lies in the single molecule detection but the

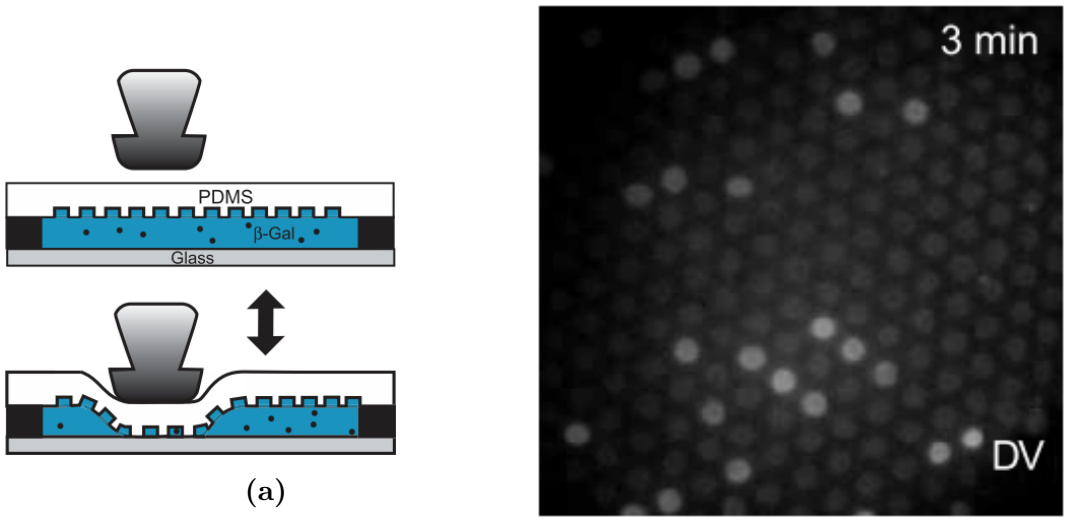

(a) **(b)**

Figure 1.19: a) A PDMS mould was created with 5 x 5 μm chambers which were placed on a glass slide with a droplet of sample. When pushed from above, the PDMS formed a 1.4 fl chamber in which the reaction of β-galactosidase enzyme and fluorescent substrate was observed (b). Taken from [138].

disadvantage is in the number of observable chambers. Rissin et al. developed an array of wells by sealing an optical fibre bundle to a slide containing enzyme solution, similar to Rondalez et al. Again, single enzyme behaviour was observed in these chambers (2.5 x 10^5 individual femtolitre wells of volume 46 fL), at concentrations of 72 fM [139]. This technique was refined by etching the optical fibre to customise the chamber dimensions [139,145,146]. This ability to change the reaction volume is advantageous as it can increase the limit of detection due to larger volumes enabling a higher probability of capturing a single molecule in a more dilute solution. The fibre array has its disadvantages in the number of observed reactions. In order to further decrease the LOD, there is a requirement to observe more of the sample solution. Increasing the volume of the reaction vessel comes at a trade off as the amount of time required

for a detectable signal to be generated by a single enzyme molecule increases. Another way to combat this is to add fibres to the array. The volume of the reaction is set at the beginning of an experiment and may, depending on the concentrations being investigated, require multiple attempts to fine tune the required volume.

Trapping single molecules in wells or droplets is governed by Poissonian statistics[3,126]. The ratio of trapping wells to target molecules dictates the probability of different numbers of molecules being captured in one well. The Poission equation describes these probabilities and is shown in equation 1.11 where $P(k)$ is the probability of k events of a capture event with average success λ. When detecting single enzymes (digital counting) the concentrations are made low so that the probability of one enzyme being present is low and the probability of two is so low that it is statistically unlikely. Table 1.3 shows the probabilities of zero, one and two molecules being captured when the average occupancy is 0.1, 0.01 and 0.001. This shows that if an experiment is observing 1000 individual reaction vessels at 10 % occupancy, there will be on average 4.5 where 2 molecules are trapped. This must be taken into consideration when observing single molecule reactions.

$$P(k) = e^{-\lambda}\frac{\lambda^k}{k!} \tag{1.11}$$

Mean	P(0)	P(1)	P(2)
0.1 (9.4 pM)	90%	9%	0.45%
0.01 (0.94 pM)	99%	0.99%	0.005%
0.001 (94 fM)	99%	0.099%	$\ll$1%

Table 1.3: Poission probabilities for 3 droplet occupancies.

The use of droplets as enzyme detection vessels has advantages over previously mentioned techniques. The ability to control droplet size through flow rates requires no changes to device design as would be the case in fibre optic or cast well designs[138,139,147]. Courtois et al.[148] investigated the use of droplets as enzyme reactors and the leaking of small molecules from droplets into the continuous phase. Stabilisation of droplets with Abil EM 90, a silicon based polymeric surfactant, and a 5 % Bovine Serum Albumin (BSA) solution reduced leakage of fluorescent products from droplets into neighbouring empty droplets. Showing this stability paved the way to translating ELISA from a bulk technique to a valid detection system. A schematic of the device used is shown in figure 1.20. The device generates droplets and lead to a storage area where the droplets are incubated for several hours. The storage system is simple, once stable droplet generation is achieved, the tubing connecting the syringe drivers to the chip were cut. However, this interruption of flow causes instability in the channel pressure and the final produced droplets are typically larger than they were in the previous stable formation. This is evident in figure

1.21 where there is a polydispersity. Although the use of a stabiliser and BSA solution reduced the leakage of fluorescenct molecules into neigbouring droplets, it did not eliminate it. The confinement of fluorescent molecules in the droplet they were produced in is key in single molecule detection as transfer into other droplets produces false positive readings.

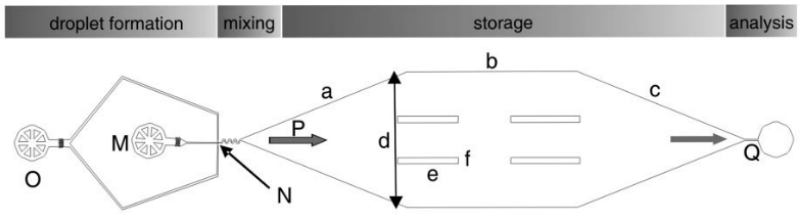

Figure 1.20: This microfluidic device generates droplets for observation in a storage area. Channel height = 25 μm. Enzyme/substrate solution was injected into an aqueous inlet (M) where it joins an oil inlet (O) at a flow focussing junction (N, 10 μm) to generate droplets. A serpentine mixer leads into a reservoir (P) where a = 7.72 mm, b = 7.3 mm, c = 7.2 mm, d = 5.78 mm. This contains four pillars (e = 3 mm, f = 300 μm) and a 30 μm outlet channel. Taken from [148].

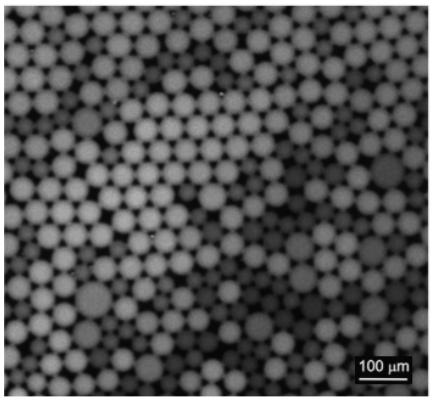

Figure 1.21: Droplets generated by the chip in figure 1.20 after 6 hours of incubation show the production of a fluorescent signal. Fluorescent molecules have leaked from the brighter droplets into the darker population. Taken from [148].

Rissin et al.[126] displayed the ability to detect prostate cancer biomarker (PSA) at concentrations of 0.4 fM using a similar method to their previous studies with bunched fibre optics[139]. The immunocomplex traditionally formed on

a surface in ELISA was translated to a bead based ELISA. Shown in figure 1.22, primary antibodies were conjugated onto 2.7 μm diameter beads to act as the surface. The beads were mixed with a solution of PSA at concentrations so that, under Poissonian statistics, only one target biomarker would bind to the bead. The beads were washed and the detection antibody/enzyme complex was bound. This solution was placed under the fibre bundle after mixing with the enzyme substrate and fluorescently imaged after an incubation time of 2.5 minutes. The ratio of the number of fluorescent chambers to the total number of beads (of known concentration) can be used to infer bulk biomarker concentration. This work showed that the ELISA process is transferable to a confined droplet system and that concentrations of biomarker below that which a standard ELISA test can detect are possible to measure. The key advantage of sub-ELISA concentration detection of PSA is monitoring of patients who have undergone a prostatectomy as a treatment for prostate cancer. This operation removes the prostate and should halt the production of PSA within the body. An increase of PSA levels post operation can indicate a biochemical recurrence of cancer[122,149–151] and affects approximately 35% of prostatectomy patients[152]. The lower the limit of detection, the earlier this increase can be detected.

Bead based ELISA was demonstrated by Kim et al.[140] where bead solutions were injected into a device containing etched wells formed from a hydrophobic

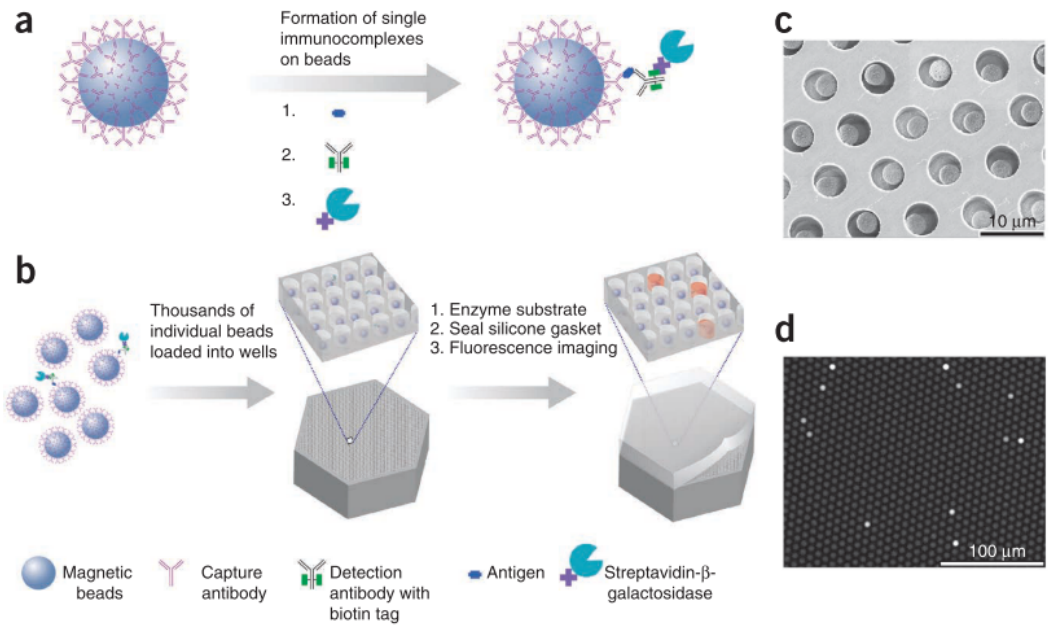

Figure 1.22: Digital ELISA of PSA with femtolitre fibre optic wells. a,b) Single protein molecules are captures on antibody coated beads with standard ELISA reagents. These are loaded into wells and sealed with a gasket before incubation and imageing. c) Scanning electron microgrpah of beads within wells. d) Fluorescence of beads after detectable signal was generated. Taken from [126].

fluoropolymer in an open storage area where the beads settled before slowly replacing the fluid above the wells with a flow of oil. This produced discrete droplets that were measured in a similar way to that which has been previously described, achieving a 2 aM detection limit of prostate specific antigen with 3 droplets fluorescing in an array of 5593 droplets [140]. A schematic of this method is shown in figure 1.23 Magnetic beads have also been used in a similar fashion to Kim et al. where the beads are actively transported to the wells through magnetism rather than gravitational effects [153]. This device is capable of observing 1 million beads with a bead capture efficiency of around 23% of injected beads. This small efficiency could lead to loss of many enzyme

conjugated beads at lower concentrations making lowering LOD difficult. The throughput of the system is also slow due to the necessity to ensure all beads have been removed from the patterned surface before a second sample can be measured. This may limit screening of multiple biomarkers in a short space of time with this system.

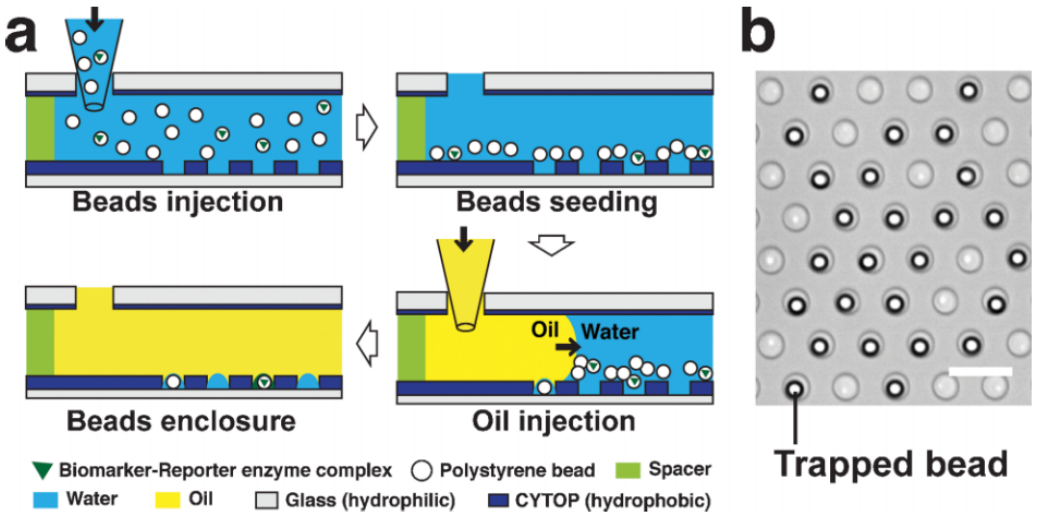

Figure 1.23: a) A solution of ELISA beads and enzyme substrate are injected into a channel containing a micro-patterned surface with 5 μm circular wells. After settling, the excess aqueous solution is displaced with an oil phase to form droplets in each well. After incubation, these are observed using fluorescence. b) 3 μm beads are trapped in water in oil droplets immobilized on the hydrophilic surface. Taken from [140].

Shim et al. showed the detection of PSA using femtolitre water in oil droplets of diameter 4 μm generated at a frequency of up to 1 MHz [3]. These droplets mixed the bead based immunocomplex and fluorescent enzyme substrate at the droplet generating flow focusing nozzle as shown in figure 1.24. Using integrated monolithic microfluidic valves, the droplets were trapped in 40 arrays of up to 5600 droplets each. This system was able to detect PSA at a

level of 46 fM. The advantages of such a droplet based system include the high throughput measurement as well as the ability to adapt the rector volume to tune experimental conditions. Due to the high rate of droplets production, after a sample has been measured the valve controlling the droplet storage area is released and new droplets can flow in, minimising time between measurements. The disadvantage of the device design is that many droplets are wasted while the current sample is incubating. The bead capture efficiency of this system was reported to be on the order of 10 % limiting the number of measurable beads and therefore the limit of detection.

The level of PSA in a healthy patient is high enough to saturate typical digital counting microfluidic ELISA systems. Piraino et al. combined digital counting immunoassay with traditional ELISA to create a device capable of spanning 5 orders of magnitude in detectable concentrations[88]. The traditional ELISA element comprises of 200 μm wide x 15 μm high chambers where neutravidin had been attached to the bottom surface after which primary antibodies were conjugated. The digital chambers were of the same dimension but incorporates a pressure actuated button containing 5 μm x 5 μm chambers which pressed down into the chamber forming discrete wells. These wells are named MITOMI (mechanically induced trapping of molecular interactions) The schematic in figure 1.25 shows the two separate systems working together in one device. 16 chambers are available to perform different immunoassays

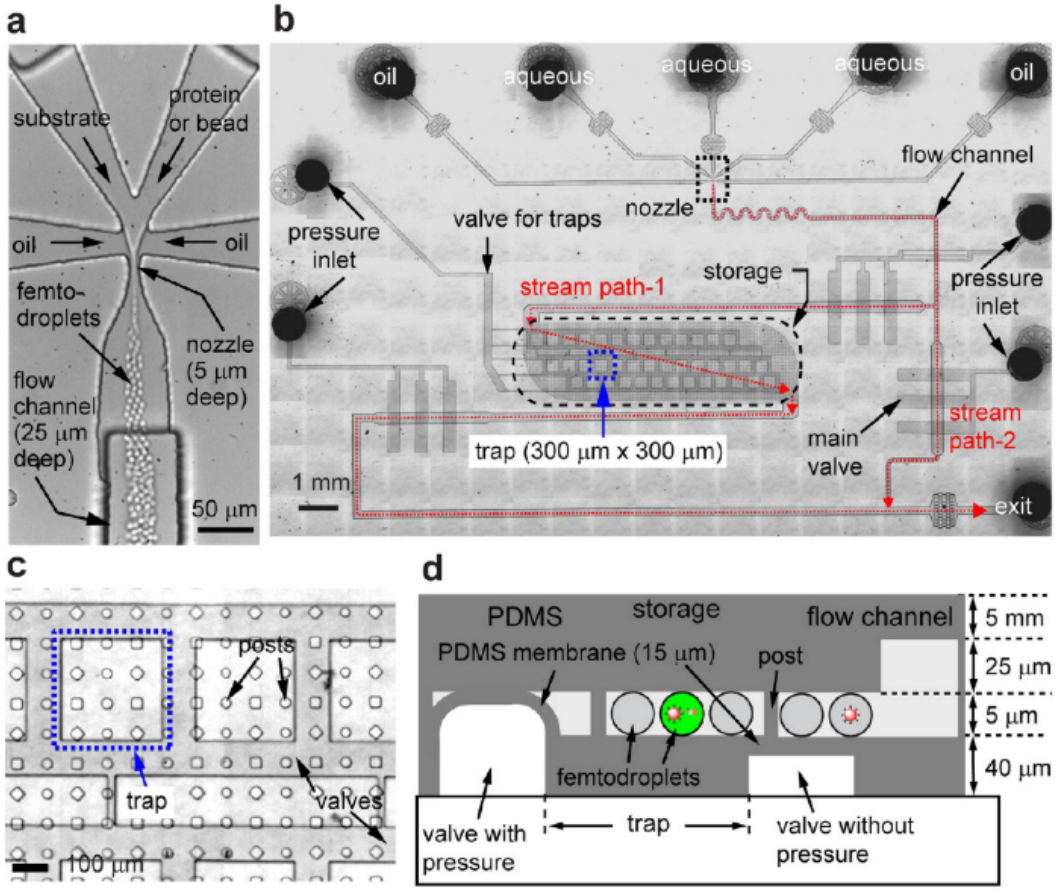

Figure 1.24: a) Femtodroplets are generated with a 10 x 5 μm flow focussing nozzle combining an ELISA-bead prepared off chip with FDG substrate. b) The device contains two layers, one for flow and one for control. After generation, the droplets can be redirected using valves into a storage area with 300 x 300 μm traps (c,d) capable of storing 5000 droplets. Taken from [3].

allowing for multiplexed detection. This device was integrated with a USB camera and shown to have potential applications in field based scenarios or low resource settings. The operation of the device can be complicated as the network of pressure control channels is complex. This device was used to detect anti-Ebola IgG from 10 nM down to 100 fM. The ability to detect this large range with individual chambers allows for the multiplexing of multiple target biomarkers where the clinically relevant concentrations differ by many orders of magnitude.

Multiplexed immunoassay is the detection of multiple targets in the same measurement[115,116,154–156]. This can be useful if a disease presents with multiple biomarkers or multiple diseases are being screened[157]. Piraino's analogue-digital device was shown to be able to differentiate three different anti-Ebola IgG strains[88]. Rissin et al. showed the detection of four different proteins, tumour necrosis factor α (TNF-α), Interleukin - 6 (IL-6), Interleukin - 1α (IL-1α) and Interleukin - 1β (IL-1β)[158]. These proteins are involved in signalling within the immune system and can indicate the presence of a multitude of diseases[159]. This was achieved by labelling the beads used during the immunoassay so they could be differentiated with fluorescence imaging. This approach increases the number of detectable species during measurement but multiplies the minimum detectable concentration during multiplex by the number of targets. During full four way multiplex the limit of detection of the proteins was

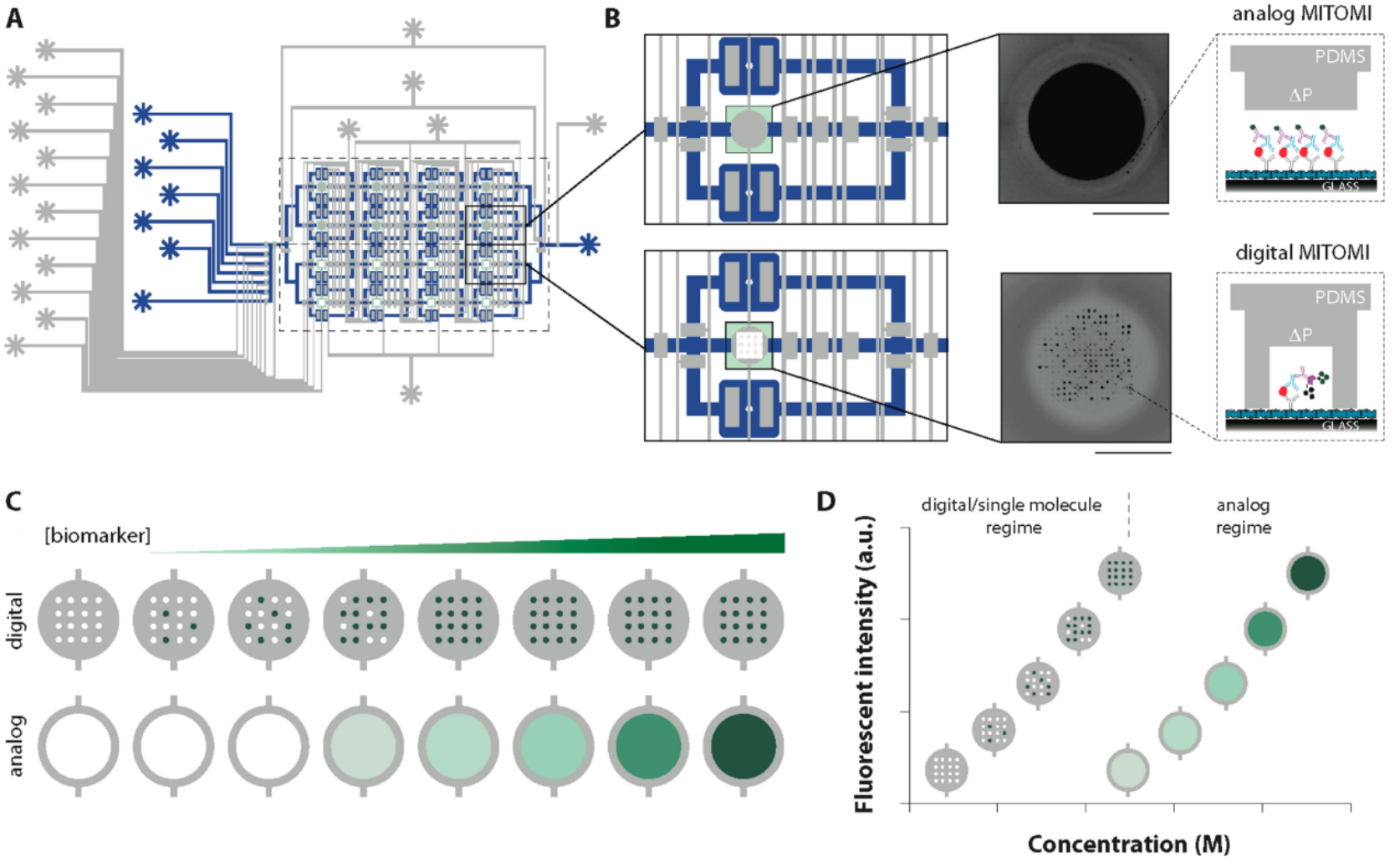

Figure 1.25: Analogue-digital immunoassay device. A) The device comprises of 16 individual immunoassay units with flow (blue) and control (grey) channels. B) Each immunoassay unit comprises of two reagent chambers, an assay chamber, isolation valves and a MITOMI button. A cross section shows the different contents of an analogue and digital chamber. C) Increased biomarker concentration leads to a saturation of the digital immunoassay but the analogue measurement shows an increase in signal. D) The combination of analogue and digital shows how a broad dynamic range can be achieved. Taken from [88].

between 1.2 and 3.9 fM. Individual detection lowered the limit of detection to 0.2 - 0.6 fM. The Simoa HD - 1 analyser is a commercially available multiplexing immunoassay device that has been theorised to be capable of multiplexing 10 proteins at once[160]. Derived from fibre optic well devices previously described[126,145,147,160,161], the device contains many of the elements described in this introduction. Testing has shown the 3-plex systems can be measured but the reality of 10-plex may not be achieved due to interactions of biological targets with antibodies and detection molecules meant for other targets. The footprint of this machine is quite large and is proposed to be a fixed laboratory item.

The challenges involved with microfluidic immunoassay vary. In static systems such as mechanically induced arrays or micropatterend surfaces, the size and geometry of the reaction volume is set before experimentation and may be difficult to adapt without changing large parts of the devices. Generation of droplets as reaction vessels through methods such as flow focussing can overcome this due to the ability to change volume easily. Due to the incubation times associated with single enzyme reactions being on the order of 10 minutes, droplets are generated and wasted while measurable signal is being generated. The rate of generation is large (MHz), a way to take advantage of these droplets would not only enhance the LOD of a system, but also massively increase the throughput of measurement. The time for a signal to be present in a droplet

is so long that methods such as single droplet measurements in flow with a laser, for example, are not feasible. Storage of droplets in monolithic valve type structures are easily scaled up, the production of a device with multiple banks of storage compartments may allow for the utilisation of some of the wasted droplets.

The detection of cancer biomarkers is common in microfluidic immunoassays although sometimes consideration is not taken into clinically relevant levels of these molecules. PSA is a popular cancer biomarker to be measured in these systems. Usually the motivation calls for monitoring of post prostatectomy levels as a health human PSA level is 10's of nM and these assays are, at their extremes, detecting attomolar concentrations. The development of the immunoassays to multiplex biomarker detection may not be clinically relevant for the target biomarkers, but development with a known system is key before diverging and seeking new molecules to detect [31,106].

1.4 Pressure Drops in Deformable Channels

PDMS is an elastic solid and under pressure driven flow the microchannels it forms can deform significantly. This behaviour has been used as an advantage in some microfluidic devices as valves, cell sorting devices, pumps and droplet formation [45,47,102–104,162–165]. The large deformation of channels leads to increased

surface area and reduced pressure drop throughout the system which can be overlooked in device design. Efforts to model the flow in collapsible tubes have been proposed[166], 3D compliant models were developed to study viscous flow in a compliant tube by applying steady three dimensional Stokes equations to analyse the flow[167]. Holden et al. observed the bulging of a PDMS channel through fluorescence microscopy while modifying a theory of convection and diffusion within microfluidic devices originally applied to rigid glass[168]. Hosokawa et al. developed a device that used a deformable diffraction grating to monitor the internal pressure of the channel[169]. Cellular and protein shear flow assays are examples of applications where the actual flow profile is required to infer shear[170]. Sensing techniques that require known distances such as SPR can be affected by changes in local geometry[102,171]. The deformation of channels has been proposed to be a critical parameter in the simulation of blood vessels for the study of vascular disease[172]. The understanding of pressure induced deformation can lead to adaptations of devices to match behaviours seen in vascular systems to model blood flow in compromised biological systems more accurately.

Gervais et al. performed scaling analysis and computational fluid dynamics simulations coupled with material deformation models to explain the elastic deformation of a channel when placed under pressure driven flow[170].

For a rectangular channel, the pressure drop as a function of distance along

the channel (p(z)) is linearly proportional to the flow rate into the channel, Q.

$$-\frac{\partial p(z)}{\partial z} = \frac{12\mu}{h^3 W} Q \tag{1.12}$$

where μ = fluid viscosity, W = channel width and h = channel height[22].

There is a cubic dependence on channel height therefore small changes in height can lead to significant changes in pressure. In most cases this is advantageous as it allows soft polymer devices to operate at higher flow rates without the risk of leakage or device breakdown.

Rearranged to make height a function of pressure:

$$-h^3(p)\frac{\partial p(z)}{\partial z} = \frac{12\mu}{W} Q \tag{1.13}$$

In the model, it is assumed that the fourth wall of the device is rigid (glass) and sealed which provides a zero displacement boundary condition on the PDMS/glass interface. Above the channel, the PDMS is generally on the order of 5 mm thick and can therefore be considered a semi infinite medium.

A scaling approximation is used to estimate the deformation experienced by the channels. Beginning at Hooke's law $\epsilon = \sigma/E$ where σ is stress, ϵ is strain and E is the material Young's modulus. Since the stress is proportional to the

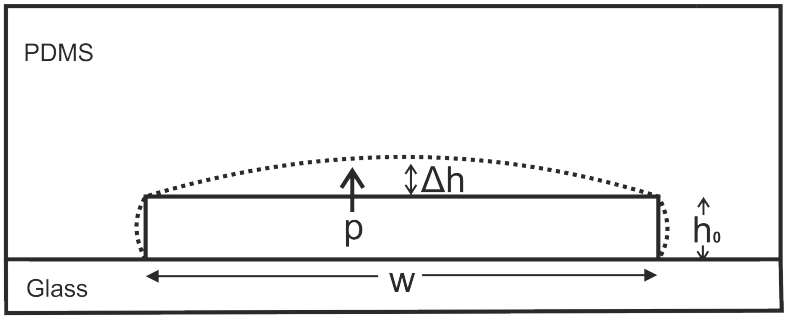

Figure 1.26: Channel cross section normal to flow. Pressure causes an increase in channel area and reduces resistance.

pressure, vertical strain becomes

$$\epsilon_{vertical} \sim \frac{\Delta h}{W} \sim \frac{p}{E} \tag{1.14}$$

and by analogy

$$\epsilon_{lateral} \sim \frac{\Delta W}{h} \sim \frac{p}{E} \tag{1.15}$$

Lateral deformation can be neglected when W $\gg$ h and the only surface of the channel experiencing significant displacement is the ceiling. At any position along the channel, the height variation is

$$\Delta \frac{h_{max}}{h_0} = c_1 \frac{pW}{Eh_0} \tag{1.16}$$

Where c_1 is a proportionality constant dependant on channel mechanical

properties as well as geometry. The top wall of the channel is assumed to deflect in a parabolic manner therefore the channel averaged height is approximately 2/3 the maximum deformation. The channel height is expressed as:

$$h(z) = h_0 \left(1 + \alpha \frac{p(z)W}{Eh_0}\right) \tag{1.17}$$

where h_0 is the channel height under no deformation and α=2/3c_1. Substituting this into eqn 1.13 and integrating over the length of the device, L:

$$Q = \frac{h_0^4 E}{48\alpha\mu(L-z)} \left[\left(1 + \alpha \frac{p(z)W}{Eh_0}\right)^4 + 1\right] \tag{1.18}$$

The proportionality constant α has not yet been determined for arbitrary channel geometries. Christov et. al. derived an expression for α which assumes the deformation of the top wall is smaller than the top wall thickness which is in turn smaller than the channel width[173]. Other models decompose α for channel geometries of aspect ratio close to unity[174]

During Gervais' experimentation it was noted that the deformation was much greater at the inlet of the device compared to the prediction given by the theory[170]. This was due to a rapid tapering of the channel before the measured section causing an unconstrained displacement boundary condition at that point. It was stated that this effect disappears after a few channel

widths down the length and therefore will not impact the equation if the first measurement point is sufficiently far into the device.

Hardy et al. applied the theory devised by Gervais et al. to fluorescence microscopy images of channels without confocal imaging[172]. The channel height was inferred from fluorescence intensity of an x-y image of a channel and the pressure was measured at the same points with pressure transducers. The acquired height measurements agreed with Gervais' model for deformed channel heights for devices where the bulk PDMS thickness above the channel was 3 mm. However, when the thickness was reduced to 1.5 mm, the semi-infinite approximation broke down and the obtained values deviated from the model. The pressure drop of channels that have thin ceilings on the order of 100 μm have been investigated by Raj and Christov developing their own models where the fitting parameter α that was required to be calculated for each geometry is removed and the model contains no free parameters[173,175]. The derivation of the new model assumes this top wall as a membrane rather than a plate and is valid for channels where the width of the channel is greater than the membrane thickness, which in turn is greater than the channel height. During this thesis the thickness of the bulk PMDS was kept at 5 mm or above so Gervais' semi-infinite medium approach applies.

The motivations for exploring on-chip pressure measurements start with the fact that in the literature described, the channel lengths used are generally be-

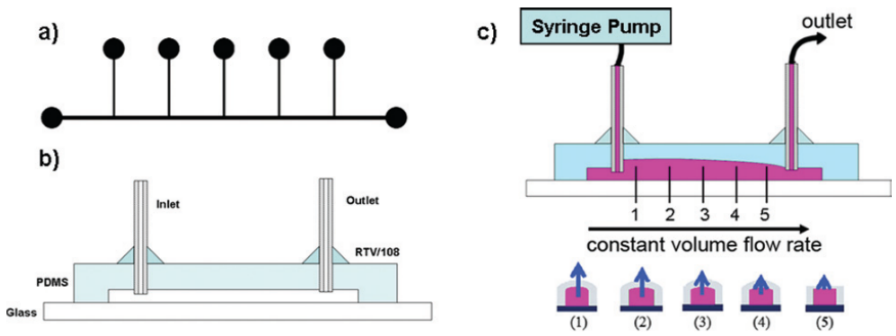

Figure 1.27: a) Hardy et al. used a 5 mm long channel of width 500 μm with 5 pressure measurement ports. b) A cross sectional view shows the interfacing of the straight channel. c) This schematic shows the pressure variation expected along the channel as a function of distance both on the side plane and across a cross-section. Figure adapted from Hardy at al.[172].

tween 10 - 50 mm and usually comprise of a straight section of channel, see figure 1.27. As microfluidic technology continues to develop, the size and complexity of the structures involved are ever increasing and the theories provided so far in the literature require testing to find if they are suitable to describe pressure/flow relations in such large devices. Although often overlooked, the knowledge of pressures built up in microfluidic systems are key when deciding materials to use for device construction[12]. PDMS is still a very popular and widely used material for device fabrication and through plasma bonding with glass can withstand pressures of up to 50 PSI[43]. However, if the proposed device will exceed these pressures within PDMS, an alternative material may have to be proposed.

In chapter 4, as well as pressure induced deformation of PDMS, material transport into bulk PDMS is investigated. As microfluidics is used in a wide variety of biological applications[1,86,176] it is important to understand how fluids

within the channels react with their surrounding microfluidic structures. PDMS is known to allow small molecules to diffuse into the bulk[177,178] with Wang et al. showing a 90% drop in estrogen concentration after 24 hours incubation in 40 mm of channel[178]. Due to the fact that cell culture on chip can take days[97], the loss of these molecules can have a severe impact on the cell growth and biological processes. The investigation in this thesis looks at the diffusion of molecules into bulk PDMS and aims to show how this can affect material properties of PDMS.

1.5 Expansion Microscopy

Expansion microscopy is a relatively new technique that couples the expansion of a hydrogel scaffold with super resolution microscopy techniques[179,180]. The aim of the expansion is to enable the resolution of components within a sample that could not usually be resolved. The development of expansion microscopy is described by Chen et al. and involved the use of sodium acrylate, a component in super-absorbent materials, a co-monomer acrylamide and a crosslinking agent N-N'-methylenebisacrylamide[181]. The components were polymerised by the initiation of a free radical reaction using ammonium persulphate (APS) and an accelerator tetramethylethylenediamine (TEMED). A block of gel polymerised this way experiences a 4.5 fold increase isotropic expan-

sion when immersed in water. To image biological sample, a fluorescent anchor was devised to link the target of interest to the gel matrix. This consists of a primary antibody followed by an oligo bearing secondary antibody to tag the biological site. A fluorophore with complimentary oligo strand and methacryloyl group anchors the antibody tag to the gel matrix. After this anchoring, the biological sample is digested away with a buffer so only the anchors remain. This leaves behind a fluorescent ghost image that is a perfect representation of the sample that was embedded in the gel. When water is applied, the gel isotropically expands and the fluorophores move apart in space. This movement allows for the features to be resolved if this was not possible before expansion. Chen et al. imaged a brain slice of a mouse and was able to resolve synaptic interfaces with STORM super resolution microscopy[182]. Tilberg et al. characterised many fluorescent tags for use in expansion microscopy and multiplexed imaging[183,184] while maintaining the swollen state[185]. A schematic of the first reported protocol for expansion microscopy is shown in figure 1.28

In the expansion microscopy chapter of this thesis (chapter 5), microfluidic devices were created to attempt to translate the expansion microscopy protocol on chip. The subject of the expansion is mouse cardiomyocytes (heart cells). Dr Jayasinghe (Faculty of Biological Sciences, University of Leeds) is currently investigating ryanodine receptors in cardiomyocytes which are responsible for contractions of heart muscle[186]. When the mouse is placed into a heart failure

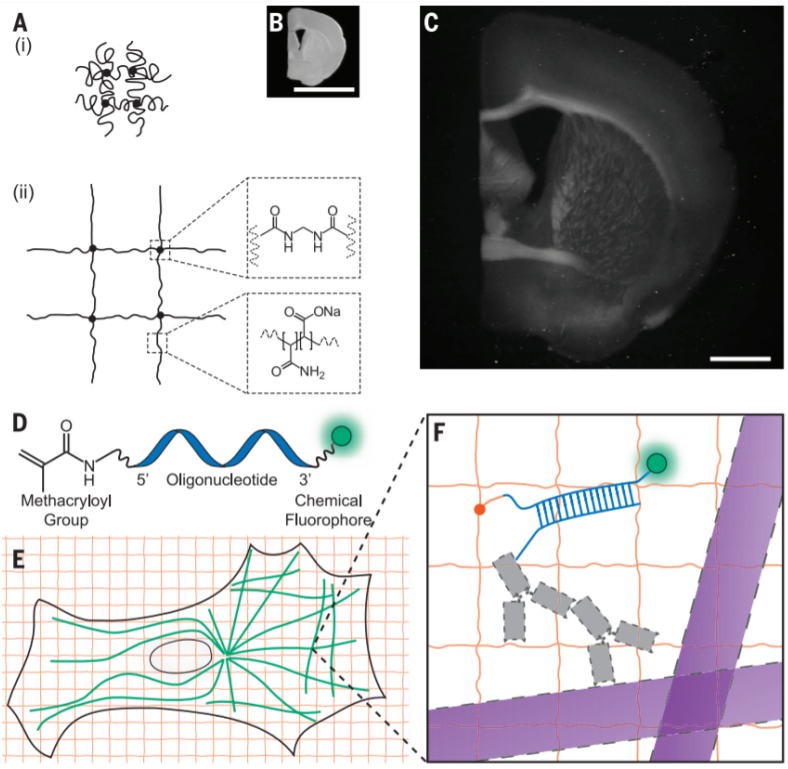

Figure 1.28: Schematic of expansion microscopy presented by Tilberg et al. in Science in 2015. A) i) Schematic of a collapsed hydrogel network comprising of crosslinker (dot) and polymer chain (line) and ii) expanded network after the addition of H_2O. B) Photograph of a mouse brain slice used in the initial report of expansion microscopy. C) Post expansion microscopy photograph of the slice shown in B) (both scale bars in B) and C) = 5 mm). D) The label that is anchored to the gel at the site of a target biomolecule. E) Schematic of target microtubules (green) within the polymer network (orange). F) The label D) hybridized to an oligo-bearing secondary antibody (top grey) bound to a primary antibody (bottom grey) to target microtubules (purple). The orange dot represents the link between the label and the polymer network which remains after the cell is digested. Digestion removes the microtubules as well as the targeting antibodies. Figure adapted from Chen at al.[181].

condition, calcium ions (Ca^{2+}) that would usually be released from ryanodine receptors is decreased. The receptors are present in clusters and are difficult to image conventionally as the individual units of the cluster can be as low as 40 nm apart. The use of expansion microscopy enhances the resolution and allows the clusters to be resolved [187,188]. The acrylamide gel used in expansion microscopy is fragile, especially in a swollen state due to the high water content [185], so a proposal for integrating all components of the protocol on chip was created. The iterations of chip design and issues encountered will be described. The aim of the project was to lay the foundations of a versatile platform for the expansion and imaging of various biological samples. If a microfluidic device of tunable chamber size can be created, the amount of expansion can be tuned. Currently the standard recipe for expansion microscopy allows for an expansion of 4X although current innovations are pushing the expansion to 10X and above [189].

1.6 Aims and Motivations of the Project

1.6.1 Single Molecule Detection of the Enzyme β-galactosidase and Prostate Specific Antigen

Chapter 3 shows the charaterisation of a femtolitre droplet generating device along with the investigation of single enzyme detection and ELISA of PSA on

chip. Based on the work of Shim et al.[3], this work intends to expand the usage of the device proposed in the previous study to enable lower concentrations of target biomarker to be detected. To achieve this lower LOD, the implementation of larger storage areas or the utilisation of wasted droplets was considered. Larger storage means more droplets can be observed and therefore lowers LOD. With such high droplet generation rates, many droplets are wasted while enzyme/substrate reactions are taking place in stored droplets. Although ultimately not achieved, these issues were the motivation to develop the microfluidic immunoassay platform. The system uses fluorescence as a detection mechanism which is becoming cheaper and easier to integrate into microfluidic templates[190]. Other methods using Raman spectroscopy, SERS, SPR, redox detection or micro-QCMD[191] require the use of sensitive and potentially expensive measurement equipment, whereas fluorescence has the potential to become cheap and portable and in some cases not requiring a microscope[190]. This could pave the way for the creation of a portable, field-based device based on current designs.

Also proposed is the multiplexing of biomarker detection within the device to screen for multiple targets. PSA is used as a model system as it is well understood within the single molecule immunoassay community as a platform to detect other biomolecules. Currently the detection of PSA at such low concentrations using these methods may not be completely suitable for diag-

nostic purposes but the model system can lead to the discovery of potential new biomolecules of interest. In this chapter it is shown that single molecules of enzyme are able to be detected but the target biomarker remained elusive.

1.6.2 Pressure Induced Deformation of Channels after Mineral Oil Absorption

The aims of the investigation during chapter 4 were to develop a method of measuring pressure on chip without the use of pressure transducers but instead using a pressurised air supply to equilibrate the flow. The use of PDMS swelling liquid is investigated and its effect on the pressure characteristics and mechanical properties of the polymer are shown. The understanding of pressure within a microfluidic device can help to assist in device design where the mechanisms being integrated onto a chip may cause excess pressure to be present. Building on current models for relatively short channels (10 - 50 mm) this work will demonstrate the measurement of pressure within channels of length up to 470 mm and showing that these models do hold for such geometries. The absorption of molecules into bulk PDMS can be an issue for biological systems on microfluidic chips as key signalling or stimulant molecules can be lost into the bulk[192]. Using Raman spectroscopy, it is shown how molecules from a mineral oil permeate into the bulk and the associated time scales involved. This also leads to an investigation of how these absorbed molecules induce a mechani-

cal property change in the PDMS through change of Young's modulus. This change then influences the pressure within the channel.

1.6.3 Chip Development for Expansion Microscopy Imaging of Cardiomyocytes

Chapter 5 shows the developmental stages of a device to capture cardiomyocytes within an acrylamide gel for the purpose of performing expansion microscopy on chip. The first four iterations of the device are described and initial experimentation shown. The process of expansion microscopy requires the handling of delicate hydrogels that are prone to damage during transportation to various steps of the protocol. The use of a microfluidic device has been proposed to enable the protocol to be carried out without the need for such transport, enabling an easier protocol for such delicate samples. The proposed system could be scaled to accommodate cells of varying size after characterisation of the process is completed. As of writing, the cardiomyocyte cells have been successfully captured in the acrylamide gel and the future steps involve digesting and expanding the samples.

Chapter 2

Materials and methods

This chapter provides an overview of the experimental techniques used in this thesis. These include microfluidic manufacturing techniques, preparation of samples for single molecule detection and optical microscopy/spectroscopy techniques.

2.1 Device Design

The device used to perform immunoassay experiments is shown in figure 2.1. The device is made up of two layers, a layer that contains the two immiscible fluids that form and transport generated droplets (from here, the flow layer) and a layer containing valve structures to manipulate the flow directions of fluids

within the flow layer (from here, the control layer). The flow layer comprises of channels that are 25 μm in height and 100 μm wide. This device was designed and used in an article previously published before the work of this thesis [3].

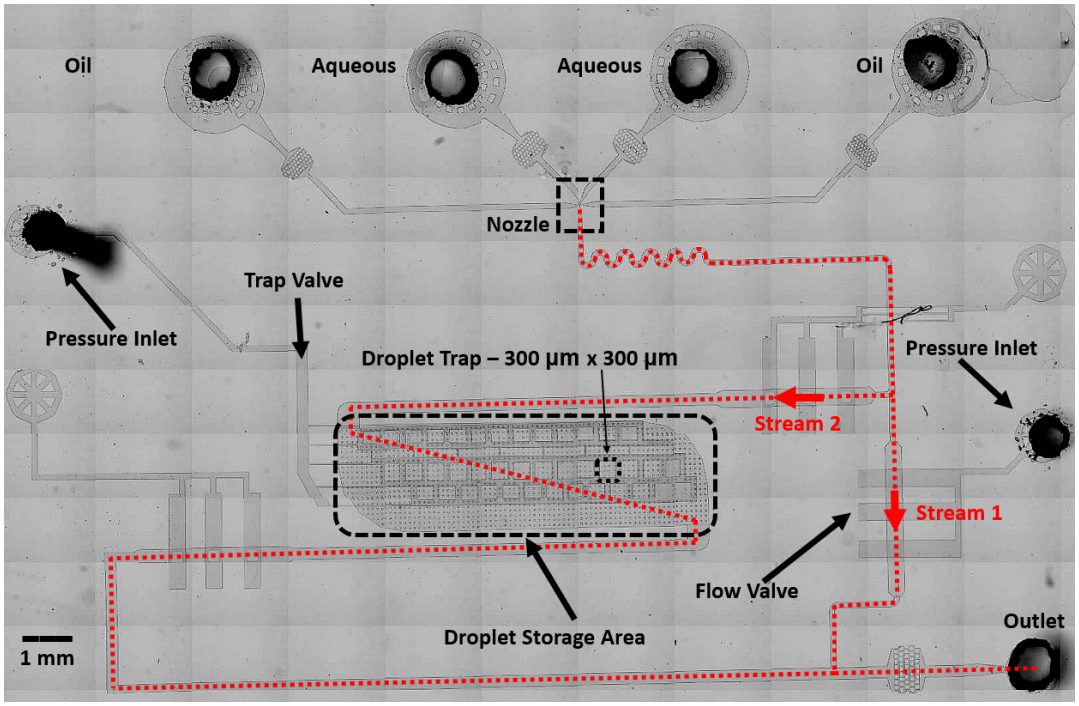

Figure 2.1: The PDMS chip used to perform single enzyme detection/PSA experiments. The upper layer consists of a nozzle (5 μm high and 10 μm at its narrowest width), flow channels (25 μm x 100 μm) and droplet storage area (2 mm x 7 mm, 5 μm in height). The control layer contains monolithic microfluidic valves actuated by pressure to control droplet flow and activate traps. After generation, droplets can bypass the storage area and leave the device (stream 1) or be diverted with the flow valve into the storage area for trapping and observation (stream 2).

2.2 Photolithography

The device consists of four fluid injection ports, two for oil and two for aqueous solutions. The fluids meet at the flow focusing nozzle, shown in figure 2.2. At

the nozzle, the aqueous solution is sheared against the oil and monodisperse droplets are formed. The theory describing this droplet production can be found in section 1.2.

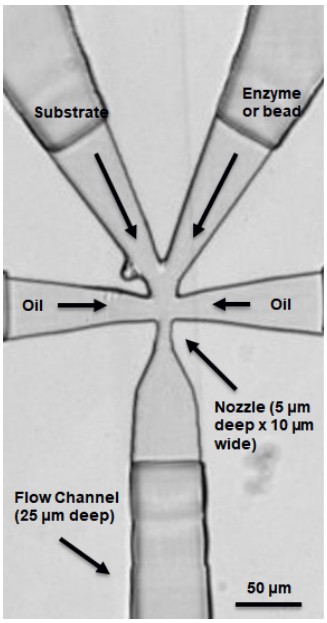

Figure 2.2: The nozzle of the PDMS device where aqueous droplets of diameter typically 4 μm are generated. Fluid inlets are 25 μm in height and 100 μm in width before reducing to a height of 5 μm. At its narrowest, the nozzle width is 10 μ wide where the droplets are generated.

After droplet production, the droplets flow through a serpentine mixer (the function of which is described in section 1.1.2.2) to ensure the reagents are thoroughly mixed. The control layer of the device is positioned below the flow layer with a thin 15 μm PDMS membrane. The application of pressure to these channels causes the flow channel above to become blocked, as described in section 1.1.2.3.

After mixing, the droplets reach a junction in the channel (shown by the red arrows in figure 2.1). With no pressure applied in the flow diversion valve,

the droplets travel down the flow channel and out of the outlet. With pressure applied, the flow is diverted into the droplet storage area. Upon entering this area, the channel height reduces to 5 μm and the droplets spread into a monolayer. The application of pressure into the trap valve causes 40 square traps to rise, confining the droplets. Trapped droplets can be released after measurement by removing the pressure, causing the droplets to flow out of the device and be replaced by freshly generated samples.

The first step in creating the microfluidic device was to design the device layout through a computer aided design (CAD) program such as AutoCAD (Autodesk). This design was then transferred onto a substrate through a photolithography process. A microfluidic master was created through lithography of SU-8 photoresist (MicroChem), a photosensitive material that is selectively exposed to UV light to cause crosslinking of desired patterns. The mechanism of SU-8 crosslinking begins with UV exposure. The UV activates triarylsulfonium salts to produce an acid which acts as a catalyst for the epoxy crosslinking of SU-8[193]. This epoxy crosslinking occurs during the post exposure bake[40,194].

3 inch silicon wafers (Pi-KEM) were cleaned with acetone followed by isopropanol, after which they were baked in an oven at 150 °C for 15 minutes to dry. SU-8 photoresist (from here referred to as resist) was deposited onto the wafer by spin coating where the speed of spinning determines the resulting thickness[193]. Devices used in this thesis had features that varied from 5 - 25

μm in height. These heights were measured using a Dektak XT surface profiler (Bruker), a stylus-based profilometer instrument after lithography was completed. To achieve these heights, 2 different varieties of SU-8 were used: SU-8 2005 (less viscous therefore thinner film thickness) for the 5 μm features and SU-8 2025 for the 25 μm. After spin coating, the wafer was baked by ramping the temperature of the wafer on a hot plate from room temperature to 55 °C, held for 30 minutes and then brought back down to room temperature. This temperature ramp reduced thermal stress within the resist film and prevents wrinkling. The purpose of this bake was to reduce the solvent concentration within the SU-8 and partially cure the film.

After the resist has been baked, there were two methods of UV exposure. The resist can be exposed using a UV lamp to flood the wafer with light of the correct wavelength while a mask containing the device design blocks areas outside of the design. SU-8 is most sensitive to 365 nm UV light which is usually emitted by a mercury lamp. Mercury lamps emit high intensity light at 3 spectral points that are useful for photolithography, 365 nm, 405 nm and 436 nm (these are know as the i-line, h-line and g-line respectively [195]). The masks used were printed on plastic transparencies of size A4 containing six 3 inch designs. This process takes place on a mask aligner (Model 200, OAI). The second method of exposure, the Direct Writing Laser (DWL) system (Microwriter 2, Durham Magneto Optics), uses a 375 nm laser to effectively draw the design.

This method removes the need for a mask as the machine only requires the CAD file as an input but increases the time of exposure from a few seconds to many hours. More complex device designs can take from 18-24 hours to expose. An advantage of the DWL system is that it is possible to quickly adjust designs without the need to order new masks at high cost.

For exposure using a mask, the following protocol was used. The baked wafer was placed on a vacuum stage after which the mask containing the required design was placed on top of the wafer. The wafer and mask were brought into contact with a piece of glass to provide tight contact. The mask and wafer were then exposed to UV light from a lamp filtered to provide 365 nm UV. Exposure time of the wafer depends on the thickness of the resist, 25 μm films require 150 mJ/cm^2 whereas 5 μm films require 100 mJ/cm^2.

Using the DWL system, the wafer is placed on a vacuum stage within the machine. The laser is then focused on the wafer surface before the design file is uploaded. The laser is of wavelength 375 nm so the exposure energy must be increased for similar exposure to the mask aligner. For example, for a 25 μm film, an exposure energy of 300 mJ/cm^2 was used. The DWL has resolution options ranging from "Fastest" to "Highest" that can be adjusted depending on the X-Y resolution of the features. A channel of width 100 μm can be exposed on "Fastest" with no degradation of the feature, however smaller features such as 10 μm flow-focusing nozzles must be exposed on "Highest". The DWL will

then perform a focus lock measurement, which can detect variations in the surface height of the resist ensuring consistent focus throughout the exposure. The laser then rasters in the X-axis, selectively exposing the resist where the design file dictates.

After exposure, regardless of method, the wafer was baked using the same protocol as the soft bake. This post exposure bake (PEB) enhances the photo-initiated crosslinking of the resist. The wafer was then developed in a solution of EC Solvent (ethyl lactate, MicroChem) which removed the areas of resist that had not been exposed revealing the desired pattern on the wafer. Depending on the feature size/exposure conditions, the resist may show some surface cracks. In order to anneal these, the wafer was placed in an oven at 210 °C for 30 minutes (hard bake).

After height verification using the Dektak XT, the wafer was coated with trimethylchlorosilane to assist in de-moulding PDMS in the soft lithography process. The master was then used in the soft lithography process.

2.3 Multilayered Devices

If the device requires multiple heights in the design, multiple layers of resist were used. The photolithography process remains the same except that after the development of the first layer, a second layer was spin coated onto the

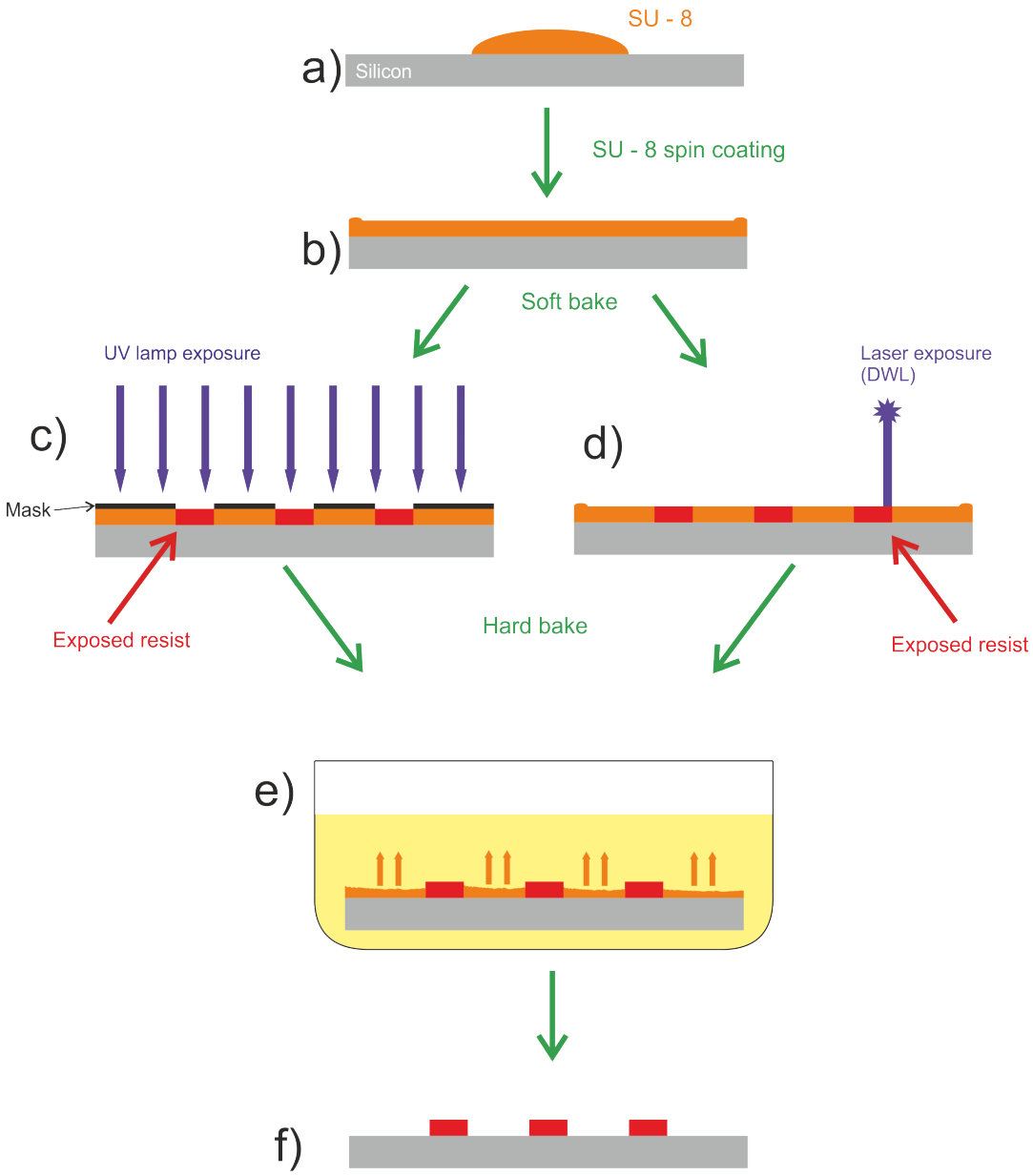

Figure 2.3: Schematic of master fabrication using SU-8. a) Su-8 is spin coated on silicon before being baked b). The wafer is then exposed to UV light by c) Mask aligner or d) DWL. e) After a hard bake the wafer is submerged in ethyl lactate solvent to dissolve unexposed resist. f) The wafer is ready for soft lithography.

wafer. After the soft bake the layers must be aligned, the method of which depends on the exposure technique. When using the mask aligner, the mask of the second layer remains stationary while the wafer was moved on the vacuum stage using micrometers to align with alignment marks on the wafer and on the mask. Using the DWL, marker points were defined using the coordinate system of the design file to correct for X-Y displacement as well as rotation. After exposure of the second layer, the process was the same as for single layer wafers.

2.4 Soft Lithography

For single layer devices, PDMS monomer was mixed thoroughly with crosslinker at a 10:1 ratio (Sylgard 184 elastomer kit, DOWSIL). The mix was centrifuged at 4000 RPM for 1 minute to remove bubbles formed during mixing. The cleared solution was poured over the master wafer inside a 90 mm petri dish to a height of 5 mm. The wafer was placed in a vacuum desiccator to remove any further bubbles before baking in an oven at 75 °C for 30 minutes. The now solid PDMS was cut from the wafer revealing channel patterns. Fluid inlet and outlet holes were punched using 1 mm biopsy punches (Kai Medical) and gas inlets punched with 0.573 mm outer diameter (23 American Wire Gauge (AWG)) needles to interface with tubing (interfacing with the device is explained in section 2.8.

At this point the channels were 3 sided and require sealing. The devices and glass slides were placed in an oxygen plasma generator (Femto low-pressure plasme cleaner, Diener) for 2 minutes, which reacts with the surface of both components converting -Si-CH_3 groups to -Si-O-H. When brought into contact, the surfaces covalently (therefore irreversibly) bond through a condensation reaction forming Si-O-Si bridges between the layers with H_2O as a byproduct[42]. The completed devices were baked at 75 °C for 30 minutes before use. Experiments in chapter 4 where the modulus of the PDMS should be controlled, all baking times were 30 minutes and the devices were used in experiments immediately to avoid changes in modulus through further baking. Devices for immunoassay experiments were left in an oven at 75 °C until required and were fully functional after multiple days in the oven.

For multi-layered devices, the first layer (top) was manufactured in the same was as described until the inlets/outlet had been punched. The second layer (bottom) was made by spin coating PDMS onto the master wafer at a height usually 15 μm higher than the height of the SU-8 features. This was achieved by spinning 10:1 PDMS/Crosslinker according to the spin curves shown in figure 2.5. The wafers were left to settle for up to 90 minutes at room temperature to smooth the PDMS before being baked at 95 °C for 10 minutes on a hot plate. The two layers were then aligned and bonded together after 2 minutes of oxygen plasma exposure and baked for 30 minutes at 75 °C. This alignment was

done by hand and appropriate design features were included to allow the device to function even if the alignment was not perfect. After baking, the two-layer PDMS was peeled off the wafer and inlets were injected for the second layer. This device was then bonded to glass using the same protocol as described above.

Using the soft lithography protocol, it was possible to produce 2 sets of single layered devices or 1 set of double layer devices per day. Depending on the size of designs, this resulted in between 4 and 20 devices.

2.5 Device surface modification - Aquapel

In order to assist the production of femtolitre sized droplets, the flow focusing nozzle of the device was coated to make it hydrophobic. This was achieved by injecting Aquapel (Pittsburgh Glass Works LLC), a car windscreen hydrophobic treatment, the main component of which is 1H,1H,2H,2H-Perfluorodecyltriethoxysilane. This was injected through an oil inlet until it reached the nozzle, ensuring it did not progress into the water channels. After application, the device was placed in a 75 °C oven for 30 minutes to dry.

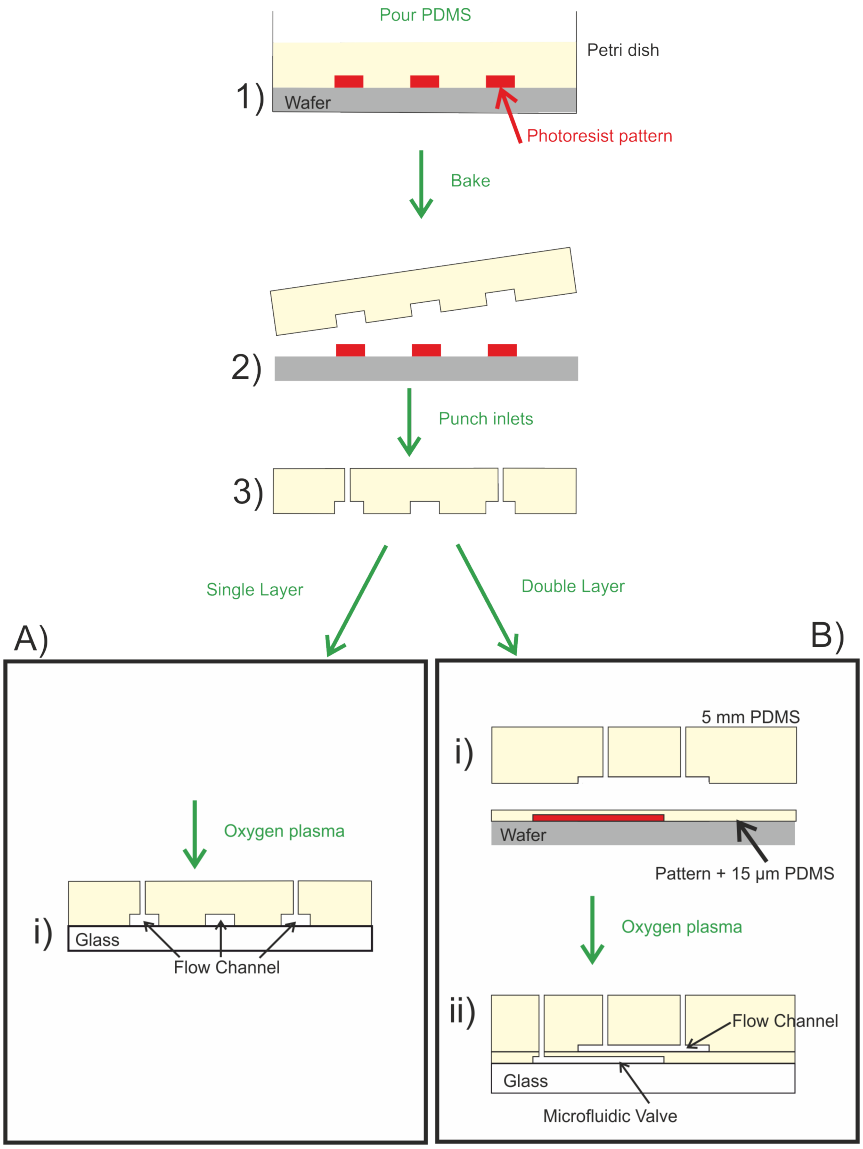

Figure 2.4: Schematic of soft lithography of PDMS devices. 1) Liquid PDMS was poured onto the master wafer mould and degassed. After a 30 minute bake at 75°C the PDMS was cut and peeled from the wafer 2). Inlet and outlet ports were punched with biopsy punches 3). For a single layer device A) the PDMS exposed to oxygen plasma to functionalise for covalent bonding to glass Ai) If the device was multilayered and incorporated valves B), a thin layer of PDMS 15 μm higher than the valve channel height was spin coated onto the wafer Bi). This was baked before oxygen plasma treatment and alignment with the flow channels previously fabricated. Both sets of channels were removed from the wafer, inlets punched for the valves and bonded to glass Bii).

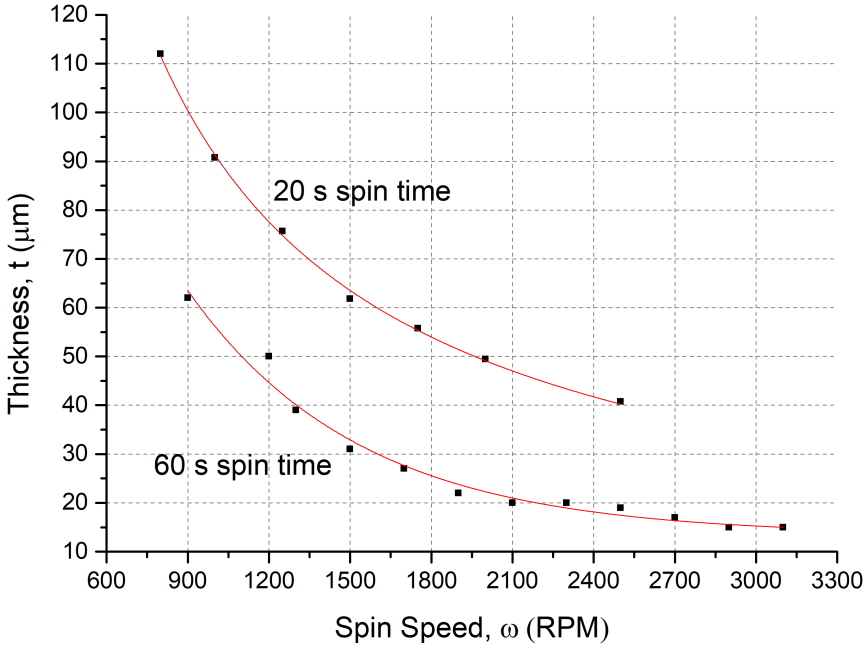

Figure 2.5: PDMS spin curve for a 10:1 ratio of PDMS base to crosslinker for a spin time of 20 and 60 s. PDMS was spread with a spin of 800 RPM for 5 seconds before spinning up to final speed

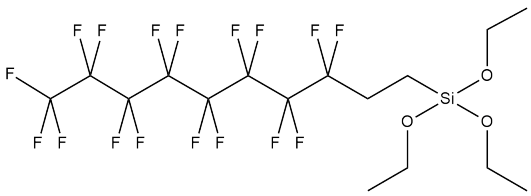

Figure 2.6: Aquapel - 1H,1H,2H,2H-Perfluorodecyltriethoxysilane. The injection of Aquapel into a flow focussing nozzle increases hydrophobicity.

2.6 Bead-Antibody Conjugation Protocol

Amino functionalised beads that are 1 μm in diameter were coupled to anti-PSA antibodies using a commercially available kit (Polysciences). PBS was prepared by dissolving one 5 g tablet of PBS powder in 500 ml of MilliQ water (pH 7.45, 140 mM NaCl, 10 mM PO 4 , 2.68 mM KCl). PBS was filtered through a 200 nm cellulose membrane syringe filter (Minisart RC4, Sartorius Stedim, UK) prior to use. Firstly, 0.129 ml of 2.5% bead solution (77pM) was mixed with 0.071 ml of PBS buffer containing 0.5% Tween-20 (Sigma). This resulted in a 50 pM bead solution. The beads then underwent a washing step involving centrifuging the bead solution for 6 minutes in a microcentrifuge at 13 kRPM then careful removal of the supernatant. The remaining pellet was then resuspended in 300 μl of PBS containing 0.5% Tween-20 via sonication for 3 minutes. After these centrifugation and sonication steps were carried out 3 times, the pellet was resuspended in 200 μl of PBS with Tween-20. 400 μl of 8% gluteraldehyde was added, which bonds to the primary amine groups on the beads. This solution was sonicated for 1 hour and shaken for 4 hours to ensure a complete reaction. The beads were then washed 3 times using the method described previously. 125μl of PBS and 75μl of capture antibody (monoclonal anti-PSA, R&D Systems) were added to resuspend the pellet. The resulting solution is composed of 50 pM bead and 200 μg/ml of capture antibody. Overnight incubation on a shaker ensures all of the gluteraldehyde molecules bond to

the primary amine groups on the antibodies. There are 4 possible binding sites of the gluteraldehyde due to the antibody being comprised of 4 monomers which bind via the N-terminus. After overnight mixing, the solution was again centrifuged and the supernatent collected. This supernatent was then analysed by UV-vis to determine the amount of protein in the solution. This value indicates how much of the protein remains and, therefore, how much has bound to the beads. The pellet was then resuspended in 500 μl of 0.2M ethanolmine and mixed for 1 hour. This step blocked any unreacted gluteraldehyde sites on the bead. The solution was centrifuged and resuspended in 500μl of 0.1 % Bovine Serum Albumin (BSA). BSA was used to block any nonspecific protein binding sites on the bead that would affect the binding of PSA to antibody in later steps. A final centrifugation for 6 minutes at 13 kRPM followed by the addition of 200μl of a storage buffer (PBS + 1 % BSA + 0.1 % sodium azide) completes the bead-antibody conjugation.

2.7 Immunocomplex Formation Protocol

Formation of the immunocomplex is shown in scematic figure 2.7. The next component of the immunocomplex was the target biomarker. The biomarker bonds to the antibody through weak chemical interactions on one of two active sites. To add this to the complex, 40 μl of the antibody conjugated beads was

added to 160 μl of PBS with 0.5 % Tween-20 resulting in a 10 pM solution. The beads were washed 3 times using the same method as previously described. The resulting pellet was suspended in 100 μl of PBS with 0.5 % Tween-20 and 100 μl of target biomarker added in a number of given concentrations as well as a control with no biomarker (PSA biomarker, 30 kDa, R&D Systems). The solution was incubated for 2 hours then washed twice. After biomarker binding a biotinylated detection antibody (polyclonal anti-PSA, R&D Systems) was conjugated. The solution from the previous step was centrifuged and supernatent removed. The pellet was resuspended in 100 μl of PBS with 0.5 % Tween-20 and 100 μl of 17 nM detection antibody. This was incubated for 1 hour and washed 6 times. The resulting pellet was resuspended in 200 μl of PBS with 0.5 % Tween-20 giving a solution of 10 pM bead and 8.5 nM detection antibody. The final component of the immunocomplex is streptavidin conjugated β-galactosidase (Invitrogen). After again being centrifuged, the pellet was suspended in 100 μl of PBS with 0.5 % Tween-20 and 100 μl of 50 nM streptavidin conjugated β-galactosidase. The solution was incubated for 1 hour before being washed 6 times. The sample was sonicated for 30 minutes and then injected into the microfluidic device for experimentation.

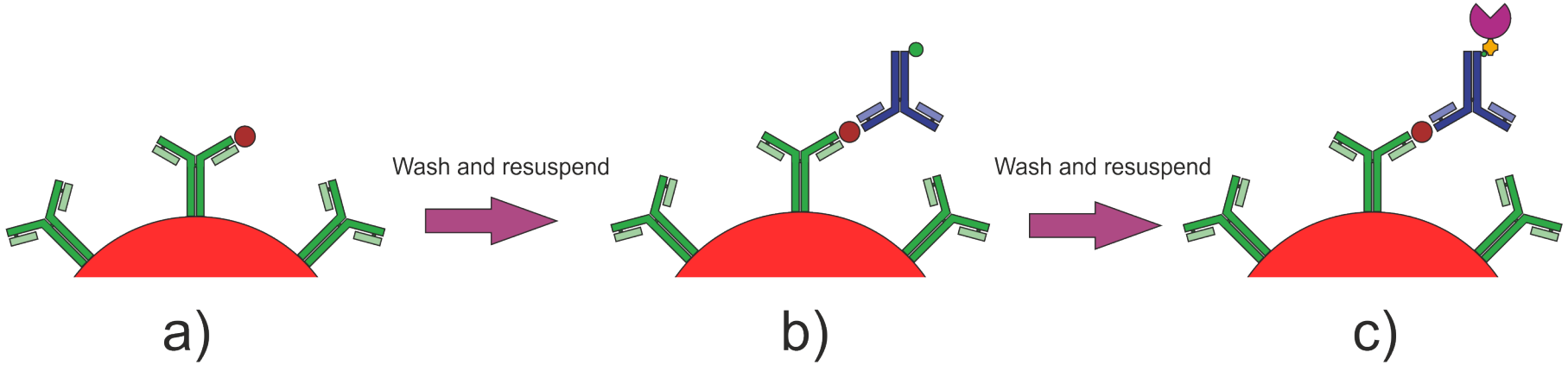

Figure 2.7: a) PSA target biomarkers (dark red) were conjugated to antibody conjugated beads formed in section 2.6 through 2 hours of incubation. The beads were washed twice before a 1 hour incubation with a secondary antibody solution (dark blue, green shows conjugated biotin). After 6 washes, the beads were suspended in a solution of streptavidin (yellow) - conjugated β-galactosidase enzyme (purple) and incubated for 1 hour. After 6 washes the beads were resuspended before injection into the microfluidic device.

2.8 Fluid Delivery - Pumps, Tubing, Interfacing with devices

In this thesis, microfluidic devices required liquid delivery and pressurised gas to operate all of the components. Liquid delivery was performed with syringe drivers, (Harvard PhD ULTRA) in either single or dual gang mode. The size and material of the syringes will be given in their corresponding experimental descriptions.

Polythene tubing 0.36 mm inner diameter and 1.09 mm outer diameter (Smiths Medical) was interfaced with devices by direct insertion into the punched inlets/outlets. Gas inlets were interfaced with Tygon® polymer tubing with a 23 american wire gauge metal insert. In devices where the connections experience high pressures, the tubing was sealed to the device with Norland optical adhesive (NOA-81, Norland Products). This adhesive was applied to the connection and cured under a 365 nm, 120 W UV lamp for 10 minutes. This provides a good seal against leakage without the adhesive being brittle. The adhesive also exhibits low auto fluorescence which will not interfere with fluorescence microscopy imaging[196].

2.9 Pressure Control System

A 95 PSI air supply was directed into 4 pressure regulators, 2 x 0-30 PSI and 2 x 0-120 PSI (March Bellofram Precision Regulator, type 10) before being connected to valve banks to actuate the supply. These valve banks connected to the Tygon® tubing described above.

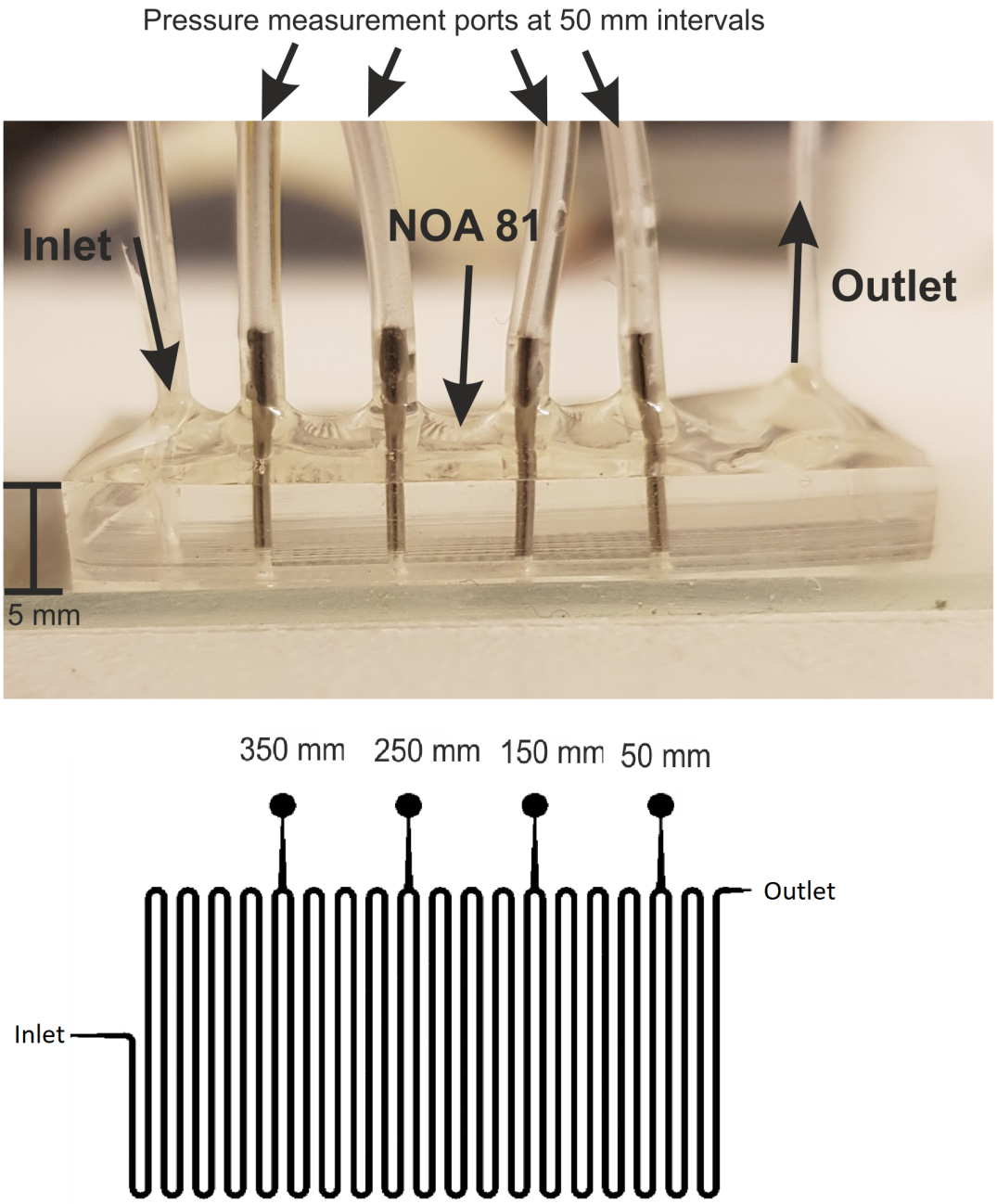

Figure 2.8: The device used in this study comprised of 250 μm wide by 21 μm deep channels. At 50 mm intervals, pressure measurement points are connected to a regulated air supply. A schematic of the device setup showing the fluid inlet and 4 pressure measurement ports.

2.10 Camera & Software

Fluorescence images were acquired using a Andor iXon EMCCD camera through Micro-Manager 3 software. During pressure experiments, bright field images were acquired with a FlyCap Grasshopper 3 camera mounted on a Motic stereo microscope.

2.11 Optical Techniques

2.11.1 Epi-fluorescence Microscopy

In epi-fluorescent microscopy, a sample is illuminated with a narrow spectral band leading to emission at a shifted spectral band. These microscopes use mercury bulbs to produce a wide spectral light source. An excitation filter is placed in the path of the light source to select the excitation wavelengths of the sample required. The beam is then directed to the sample through reflection off a dichoric mirror where the excited state of the sample relaxes to produce a fluorescence which is observed as a shift in wavelength in emitted light. This fluorescence then travels through the dichoric mirror and onto a detector.

During fluorescence measurements, a Bioimager BIM800FLW inverted epi-fluorescence microscope was used. A mercury lamp was used as the light source

and the microscope was fitted with an FITC filter set (excitation 475 ± 35 nm, Dichoric mirror 508 nm and emission 530 ± 43 nm) and a Texas Red filter (excitation = 559 nm, emission = 630 nm).

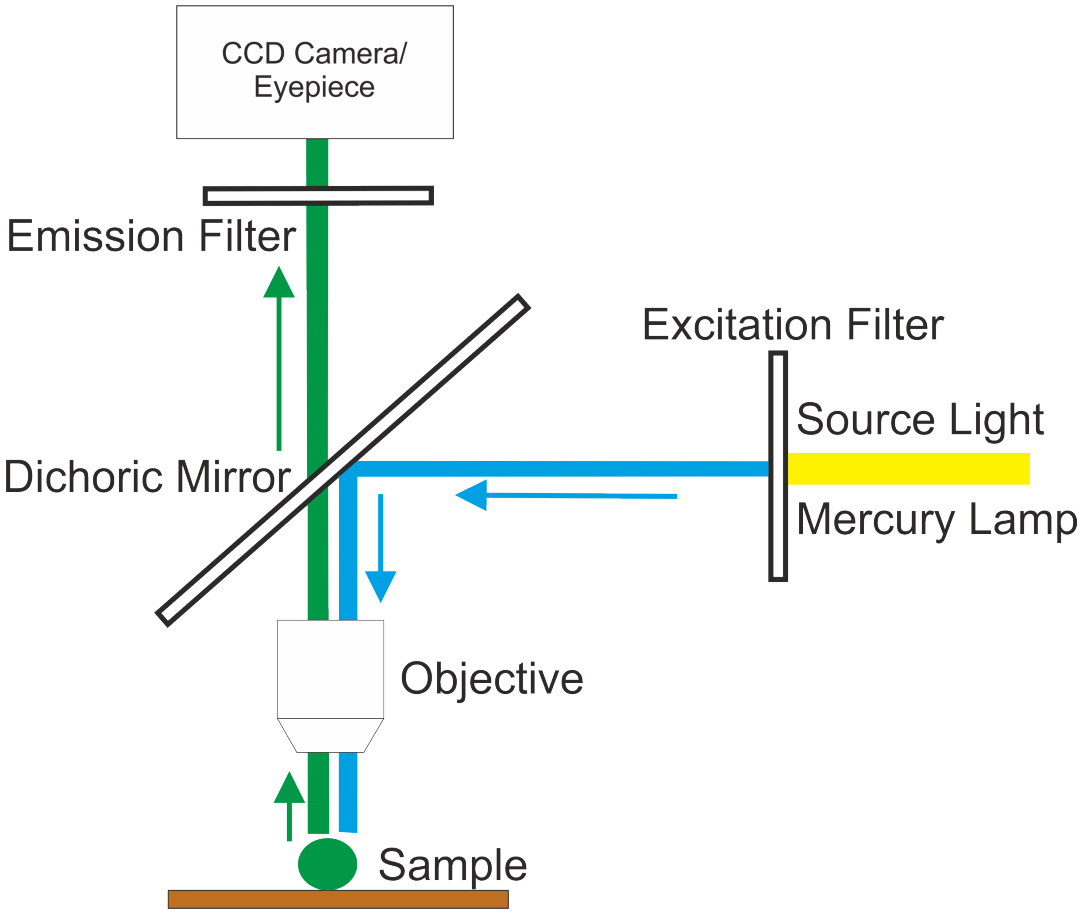

Figure 2.9: Schematic of an upright fluorescence microscope. An excitation filter is used to select the wavelength to illuminate the specimen. A dichoric mirror directs the beam to the sample and allows the emitted wavelength through to a detector after an emission filter.

2.11.2 Fluorescence Spectroscopy

During enzyme kinetics studies fluorescence spectroscopy was performed with a Perkin-Elmer LS 55 fluorescence spectrophotometer. This method uses a xenon

lamp to produce excitation light at wavelengths from 250-790 nm. Monochromators within the spectrometer select the excitation and emission wavelengths during data acquisition which is detected through photomultiplier tubes. The sample was loaded in a 1.5 ml quartz cuvette with path length 1 cm.

2.11.3 UV/Vis Spectroscopy

Ultraviolet-visible spectroscopy (UV/Vis) measures the absorption of a sample after excitation from an ultraviolet/visible wavelength source. The ratio of incident light intensity to the intensity received by a detector provides the absorption. The light source travels through monochromators to select the excitation wavelength incident on the sample. The absorbance of the sample follows Beer-Lambert's law shown in equation 2.1 where A is the measured absorbance, I_0 is the incident light intensity, I is the transmitted intensity, ϵ is the extinction coefficient, c is the concentration of the sample and L is the path length through the sample. The extinction coefficient ϵ is a property of the molecule being measured and has units of $M^{-1}cm^{-1}$. Samples were loaded into cuvettes with path length 1cm.

$$A = log_{10}\left(\frac{I_0}{I}\right) = \epsilon cL \tag{2.1}$$

Uv/Vis spectroscopy can be used to determine the concentration of protein

in a sample through absorption at 280 nm due to the presence of the amino acid Tryptophan. Tryptophan contains aromatic rings causing delocalisation of electrons in the Π–orbital. This causes a large absorption at 280 nm, the intensity of which is indicative of the protein concentration[197]. This method was used to determine protein concentration before and after antibody conjugation onto amine functionalised beads described in the bead-antibody conjugation protocol. The extinction coefficient for a typical IgG antibody with molecular weight 150 kDa is 210,000 $M^{-1}cm^{-1}$ due to the presence of 11 Tryptophan amino acids in the heavy and light chain[197]. Uv/Vis spectroscopy was performed on a Agilent Cary 5000 Uv-Vis-NIR spectrophotometer.

2.11.4 Raman Spectroscopy

Raman spectroscopy uses the principle of Raman scattering to collect molecular information about a sample. When light is incident upon a sample most of the photons will scatter with unchanged energy (Rayleigh scattering), however, approximately 1 in 10^6 photons will interact with the molecular vibrational states of the sample and experience an energy shift. This differs from fluorescence as there is no emission of a photon from an excited state relaxing to a ground state. There can be a loss in energy, known as Stokes Raman scattering, or an increase in energy, anti-Stokes Raman scattering. This energy change is dependent on the vibrational frequency of the molecules' bonds and their po-

larisability and as such, the measured energy shift provides information on molecular structure. When measuring Raman signal, the sample is illuminated with a monochromatic light source such as a laser. The Rayleigh scattered photons are filtered out before the detection of Raman scattered photons. The intensity of detected photons is plotted against wavenumber to produce a Raman spectra. The wavenumber is the shift in energy through the interactions with the molecule and its calculation is shown in equation 2.2 where Δw is the wavenumber, λ_0 is the excitation wavelength and λ_R is the Raman scattered wavelength. Displaying the energy shift as opposed to raw photon wavelengths allows comparisons of data even if taken at different excitation wavelengths. These peaks in the Raman spectra are distinctive to molecules and a spectra can be considered a molecular fingerprint. Figure 2.10 shows the changes in energy for each of the scattering regimes[198].

$$\Delta w = (\frac{1}{\lambda_0} - \frac{1}{\lambda_R}) \tag{2.2}$$

For measurement of mineral oil diffusion into PDMS, devices were prepared on 60 x 24 mm glass coverslips of # 1 thickness (130 - 160 μm). The Raman system used was an inVia Raman confocal inverted microscope (Renishaw) with a Leica DMi8/SP8 laser scanning confocal microscopy system with 532 nm, 22 mW laser. The system was calibrated with the 532 nm laser using a silicon calibration sample with expected peak at 520.5 cm^{-1}. Raman spectra

were taken of pure mineral oil, pure PDMS and an empty channel to identify characteristic peaks. A scan line of length 1 mm was positioned so that it began in the empty channel and ended within the bulk PDMS. Along this line, spectra were taken every 20 μm with an acquisition time of 1 s. After this scan the injection of mineral oil was started and spectra taken along the scan line every 5 minutes for 90 minutes.

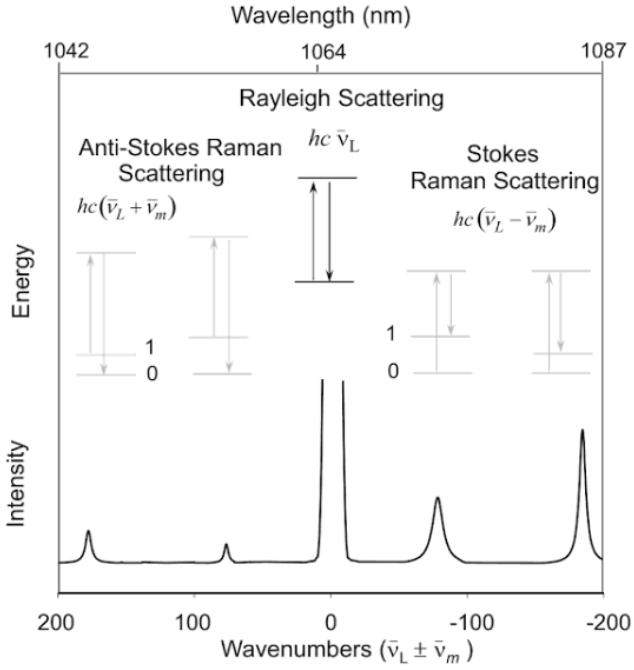

Figure 2.10: Schematic illustration of Rayleigh scattering as well as Stokes and anti-Stokes Raman scattering. ν_L represents the energy of the excitation laser which is much greater than the molecular vibrational energy. ν_m represents the vibrational energy of the molecule which is added to (anti-Stokes scattering) or subtracted (Stokes scattering) from the energy of the incident laser photon. When no interaction with the molecular vibrational modes occurs, Rayleigh scattering takes place.

2.11.5 Confocal Laser Scanning Microscopy

Confocal laser scanning microscopy is a technique for imaging samples with a shallow depth of field. The microscope is advantageous over conventional optical microscopy in that out of focus light is removed from the image with a pinhole resulting in sharp focus at the focal plane. Using a micron resolution z-stage, multiple images can be taken through a sample and reconstructed into a three dimensional image. A Leica TCS SP8 on a DMi8 microscope was used to take confocal fluorescence images of PDMS microchannels containing a 1 μM solution of fluorescein. The microscope was equipped with 488 nm, 532 nm and 638 nm lasers of which the 488 nm and 532 nm lasers were used to image fluorescein and Nile Red respectively. Channels were mounted on 60 x 22 mm, #1 thickness glass coverslips and imaged through a 40X objective. The laser rastered across the channel at a rate of 400 lines per second at a resolution of 3520 x 100 pixels. Z -stacks were taken with a z-step size of 0.53 μm from the middle of the glass coverslip until the full channel profile was imaged.

2.12 AFM Modulus Measurements

Modulus measurements were performed on a FastScan AFM (Bruker). During nanoindentation, an AFM probe is pressed into the surface of a material as the applied force and tip displacement are measured. The force displacement curve

provides a highly sensitive measurement of the probe/sample contact stiffness from which the modulus can be calculated.

The interaction of the tip and sample depend on the tip geometry and the main models are the Hertz (spherical indenter) and Sneddon (conical indenter) models. To find the modulus, the force and displacement are fed into the models[199–202].

The Hertz model:

$$F = \frac{4}{3}\frac{E}{(1-\nu^2)}\sqrt{R}\delta^{\frac{3}{2}} \tag{2.3}$$

where F = force (N), E = Young's modulus (Pa), ν = Poission Ratio (0.5 for PDMS[203]), R = tip radius (m) and γ = indentation.

For the Sneddon model:

$$F = \frac{2}{\pi}\frac{E}{(1-\nu^2)}tan(\alpha)\delta^2 \tag{2.4}$$

where α is the half angle of the indentor.

Measurements were taken using a Bruker Sharp Nitride Lever (SNL) tip with spring constant 0.07 N/m and tip radius of 2 nm and was calibrated using a silicon sample of known modulus. PDMS was prepared using the standard pro-

tocol described in section 2.4 at a 10:1 ratio of base monomer and crosslinker. During experiments, two samples were measured, the first being PDMS prepared as standard and the second having been soaked in mineral oil for 4 hours before measurement. Young's modulus values were calculated by fitting the Sneddon model to force-displacement curves using Bruker NanoScope software.

Chapter 3

Single Molecule Detection of the Enzyme β-galactosidase and Prostate Specific Antigen

This chapter will introduce and describe the experiments to detect single molecules of the cancer biomarker, PSA using a microfluidic device. The chapter will begin with experiments to measure activity of the detection enzyme β-galactosidase in bulk conditions through an enzyme kinetics study. The experiments to detect single molecules of β-galactosidase in micron width droplets will be presented along with characterisation of the droplet production process. The characterisation of immunocomplex formation for the detection of PSA will be shown followed by droplet based ELISA experiments. Finally, the results will be concluded.

3.1 Enzyme Kinetics Study

3.1.1 Objectives

The objective of this experiment is to determine the activity of the detection enzyme β-galactosidase. This will be shown through a kinetics study deducing the number of molecules digested per second (turnover number). The turnover number estimates the concentration of fluorescent product present in a droplet during single molecule detection experiments Fluorescence spectroscopy data will be shown detailing the reaction between the enzyme β-galactosidase and substrate FDG (Fluorescein di(β-D-galactopyranoside)), figure 3.1a. Analysis and deduction of key values will be presented.

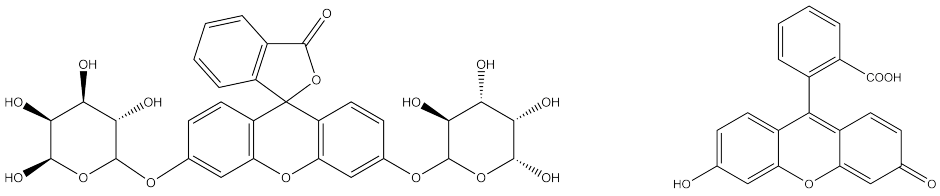

(a) FDG - Substrate **(b)** Fluorescein - Observable Product

Figure 3.1: The FDG substrate (a) is digested by β-galactosidase, which forms Fluorescein (b) and galactose.

The activity of β-galactosidase can be measured by observing the rate of reaction between the enzyme and substrate. This reaction can be characterised using Michaelis-Menten kinetics, which is a model of enzyme/substrate reactions.

The reaction between an enzyme can be modelled using equation 3.1 [86].

$$\mathrm{E} + \mathrm{S} \rightleftharpoons \mathrm{ES} \rightarrow \mathrm{E} + \mathrm{P} \tag{3.1}$$

Where E=Enzyme, S=Substrate, ES=Enzyme/substrate complex and

P=Product.

The reaction rate is the rate of product formation over time (equation 3.2)

$$v = \frac{d[P]}{dt} \tag{3.2}$$

The Michaelis-Menten equation relates the reaction rate, v, to substrate concentration, [S]. This can also be expressed in terms of the reactions maximum rate, V_{max}, substrate concentration, [S], and the Michaelis Constant, K_M (equation 3.3). The Michaelis constant represents the substrate concentration that corresponds to half the maximum reaction rate[204].

$$v = \frac{V_{max}[S]}{K_M + [S]} = k_{cat}[E]_0 \frac{[S]}{K_M + [S]} \tag{3.3}$$

k_{cat} is the turnover rate, which is the number of substrate molecules converted to product per enzyme active site per time.

3.1.2 Fluorescein Excitation and Emission Spectra

The excitation and emission of the fluorescein product were measured using a fluorescence spectrophotometer.

50pM β-galactosidase was mixed with 50nM FDG in a 1:1 ratio in a quartz cuvette. The solution was incubated at room temperature overnight to ensure full conversion from FDG to fluorescein.

The spectra in figure 3.2 show peak excitation and emission wavelengths of 484 nm & 514 nm respectively. These wavelengths were used as excitation and emission during the remaining experiments.

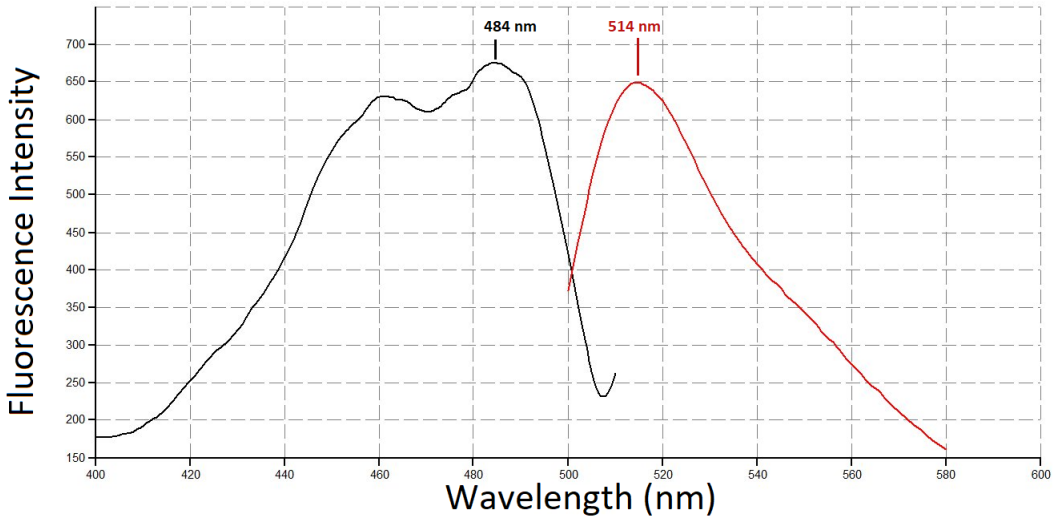

Figure 3.2: Excitation and emission spectra for a solution of 50pM β-galactosidase and 50nM FDG incubated overnight for full FDG to fluorescein digestion. Peak excitation is at 484 nm and peak emission at 514 nm.

3.1.3 Spectrophotometer Saturation

To determine the concentration boundaries of the β-galactosidase/FDG reaction, fluorescein solutions were prepared to be measured using the spectrophotometer. A stock solution was prepared by dissolving 3.32 mg of fluorescein powder in 25 μl of DMSO (Dimethyl sulfoxide). Once dissolved, the solution was made up to 10 ml with MilliQ (18 MΩcm H_2O). The resulting concentration of fluorescein was 1 mM. This stock was then diluted into 1 ml samples of fluorescein concentration 1-60 nM for measurement on the spectrophotometer. The solutions were placed in 1.5 ml quartz cuvettes and emission spectra taken with excitation at 484 nm with emission scan range 500-580 nm. The concentration limits of the instrument were found to be between 1nM & 60nM of fluorescein (Figure 3.3).

The intensity of fluorescence at peak emission (514 nm) was plotted against fluorescein concentration (figure 3.4) yields a gradient of 18.9 $\pm$ 0.3 A.U/nM. This can be used to directly convert fluorescence intensity signal into fluorescein

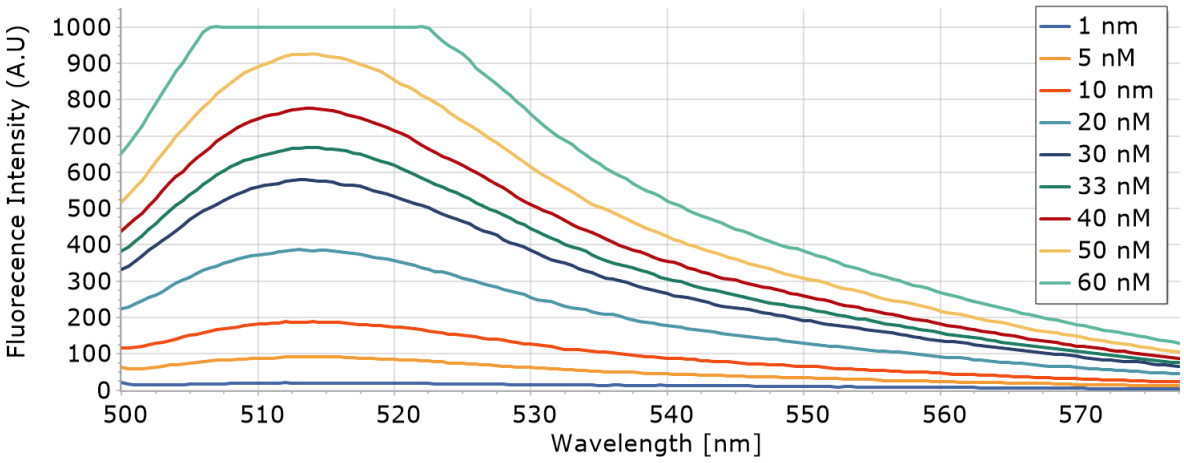

Figure 3.3: Emission spectra for increasing concentrations of fluorescein solution. Excitation wavelength = 484 nm, emission scan range = 500-580 nm. A 60 nM solution causes the instrument to saturate.

concentrations.

3.1.4 β-galactosidase/FDG Reaction Kinetics

Observing the fluorescence intensity at 514 nm over time shows the increase in fluorescein product during the β-galactosidase/FDG reaction. To monitor the reaction, 400 μl of 50 nM FDG was added to a quartz cuvette in the spectrophotometer. 400 μl of 250pM β-galactosidase was added to the cuvette and mixed thoroughly through pipetting. The instrument was set to measure the emission spectrum (between 500-580 nm) of the sample with an excitation of 484 nm, every minute. As the reaction continues, the reaction rate slows as the available substrate decreases, shown by a decrease in gradient in figure 3.5.

This reaction was repeated with substrate concentrations from 0.5 μM to 500 μM FDG. A profile of fluorescence vs time was measured and the reaction rate was calculated for each substrate concentration. The reaction rate of each was then plotted against the substrate concentration, a Michaelis-Menten curve (figure 3.6). The curve was fitted with a Hill function to output the maximum

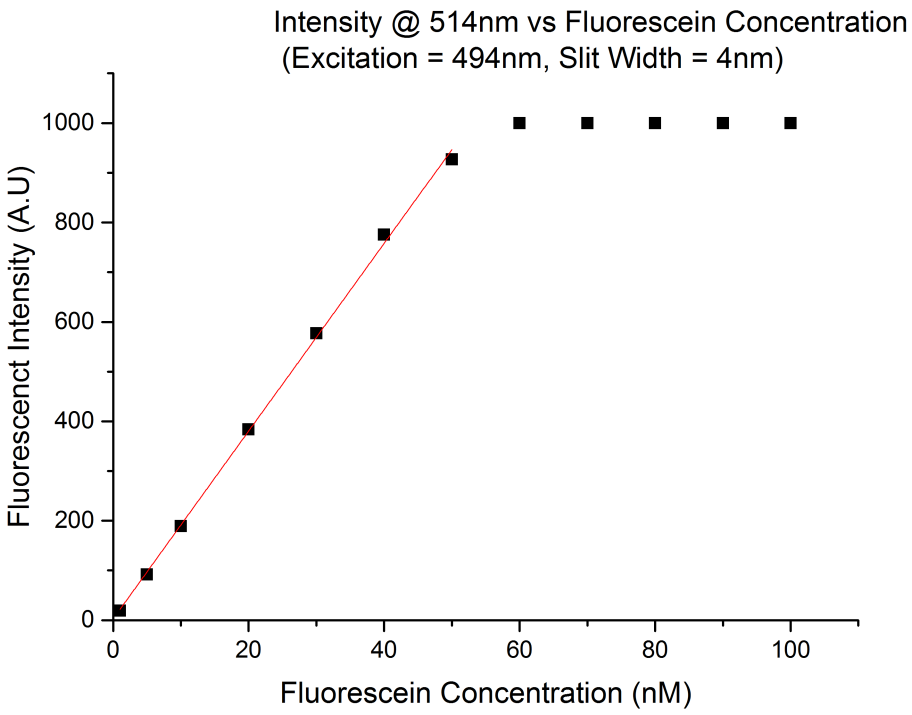

Figure 3.4: The fluorescence intensity at 514 nm increases linearly with fluorescein concentration. The spectrophotometer saturates above 50nM. This plot also gives a direct conversion factor between fluorescent intensity and concentration (18.9 $\pm$ 0.3 A.U/nM). Error bars too small to be plotted, n = 3.

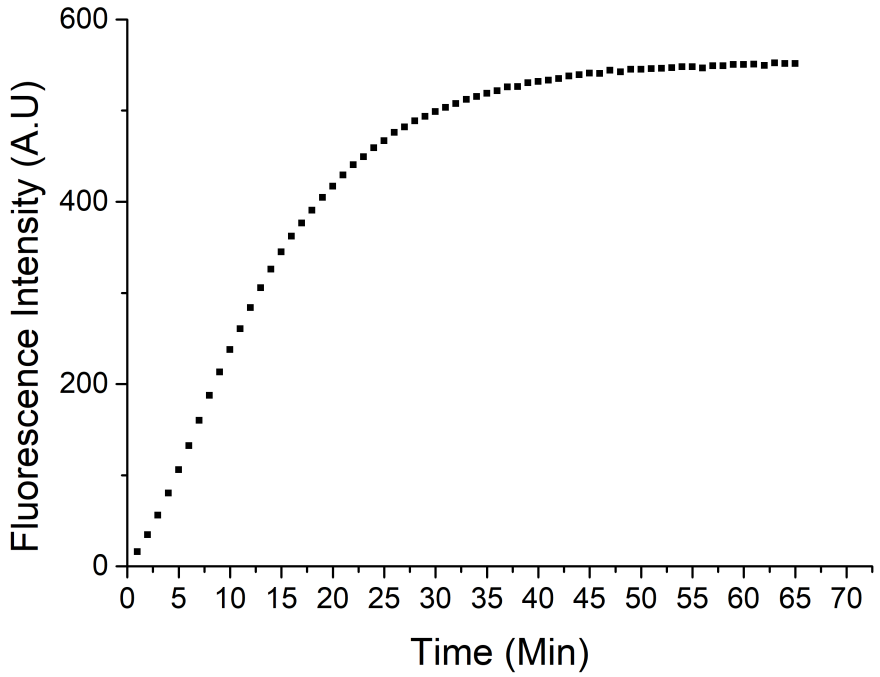

Figure 3.5: Fluorescence intensity of the β-galactosidase/FDG reaction measured at 514 nm in intervals of 1 minute for 70 minutes displays the full reaction. The initial slope of the reaction is the reaction rate (v). Single reaction plotted.

velocity, V_{max}, and Michaelis constant, K_M.

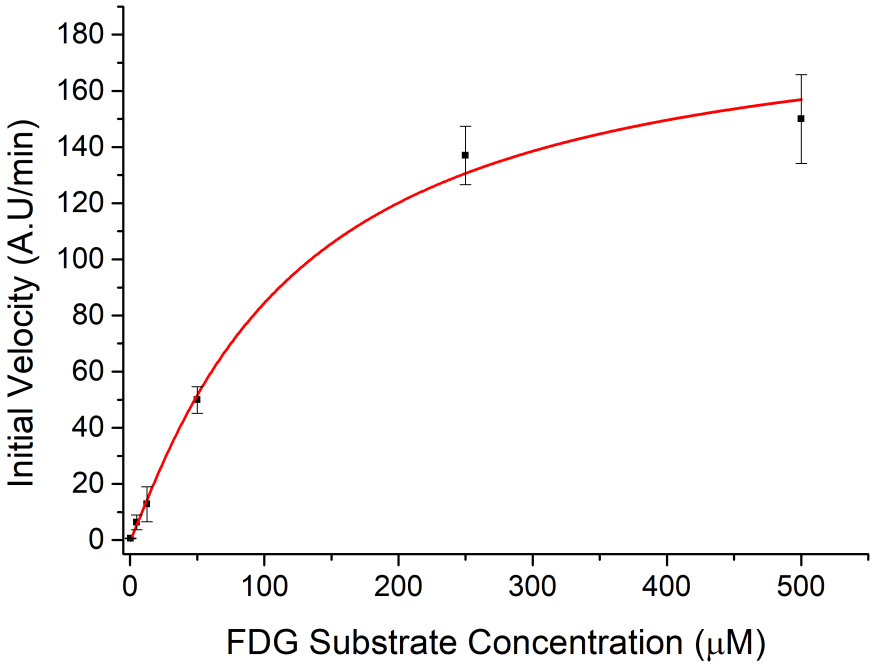

Figure 3.6: The Michaelis-Menten curve of the β-galactosidase/FDG reaction shows the rate of reaction saturating as the substrate concentration increases. For each point, the reaction rate was extracted from an enzyme reaction profile as shown in figure 3.5. n = 3

To extract the K_M and V_{max} values, a Lineweaver-Burke plot was produced (figure 3.7). The Lineweaver-Burke equation (equation 3.4) takes the inverse of the Michaelis-Menten equation (equation 3.3). The values of inverse velocity were plotted against inverse substrate concentration (figure 3.7) and produced a straight line of gradient = $\frac{K_M}{V_{max}}$ and y-intercept = $\frac{1}{V_{max}}$.

$$\frac{1}{v} = \frac{K_M + [S]}{V_{max}[S]} = \frac{K_m}{V_{max}}\frac{1}{[S]} + \frac{1}{V_{max}} \tag{3.4}$$

From the Lineweaver-Burke fit (figure 3.7), $V_{max} = 173 \pm 40$ A.U/min and $K_M = 137 \pm 30\mu M$

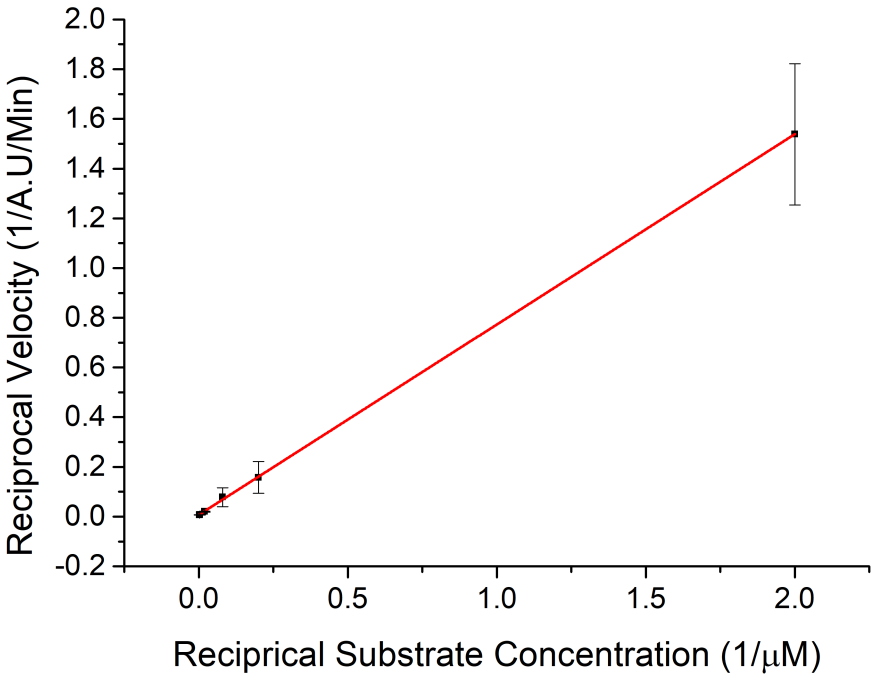

Figure 3.7: Linewaver-Burke Plot of the β-galactosidase/FDG reaction. Y-intercept=$\frac{1}{V_{max}}$ and gradient=$\frac{K_M}{V_{max}}$. $V_{max} = 173 \pm 40$ A.U/min and $K_M = 137 \pm 30 \mu M$. n = 3

To obtain the turnover number, the maximum velocity, V_{max}, is divided by the β-galactosidase concentration. $k_{cat} = 13700 \pm 700s^{-1}$. This corresponds to 13700 molecules of FDG converted to molecules of fluorescein product per second. In a droplet based single molecule detection experiment, inside droplets of diameter 4 μm, the fluorescein concentration will be $24 \pm 1\mu M$ after 10 minutes of incubation.

3.1.5 Summary

The kinetics of the reaction between enzyme β-galactosidase and substrate FDG have been shown. The literature reports K_M values of the β-galactosidase/FDG reaction to be anywhere from 18 - 638 μM[205,206]. The experiment which determined a value of 638 μM[206] was performed under the same conditions as Huang et al. (18 μM[205]) and commented that such a low result was unusual and determined under "erroneous assumptions" although these assumptions were not stated. A study by Rissin et al. whereby single enzyme molecules were trapped in a fibre optic array calculated the K_M value of the bulk β-galactosidase/FDG reaction to be 117 $\pm$ 23 μM which overlaps with the values obtained in this study of 137 $\pm$ 30[207].

3.2 Droplet Production

3.2.1 Objectives

This section will show experiments performed to investigate droplet production in a flow-focusing microfluidic nozzle. The geometry of the nozzle was modified and droplet generation observed. A description of the manufacturing process

to produce the nozzles will be given, after which measurements of droplet diameters as a function of oil flow rate will be shown. Analysis and conclusions will follow. The experiments of droplet production were performed using the immunoassay device described in section 2.1.

Monodisperse droplet production is a key feature in the biomarker detection experiments. The monodispersity of the droplets provides identical reaction vessels for the formation of detectable product through the enzyme-substrate reaction. Inconsistencies in droplet size lead to changing effective product concentrations, which can make droplets appear less fluorescent and therefore can be interpreted as not containing biomarker.

The aim of this section is to determine the flow parameters required to produce 4 μm diameter droplets in the flow focusing nozzle.

The diameter of droplets generated through a flow-focusing nozzle, D, is given in equation 3.5 from Yobas et al.[208], where Ca = capillary number, σ = interfacial surface tension, r = radius of curvature at the droplet production interface, μ = dynamic viscosity of continuous phase, Q_O = oil flow rate.

$$D = \frac{2^{\frac{2}{3}}\, Ca\, \sigma\pi r^3}{\mu Q_O} \tag{3.5}$$

3.2.2 Device Manufacture

In order to investigate droplet generation in flow-focusing nozzles, the chip to perform the single molecule immunoassay experiments was used. The geometry of the nozzle was changed by manipulating the diameter of the droplet production orifice (shown by the red arrow in figure 3.8) and new devices created using the DWL lithography system.

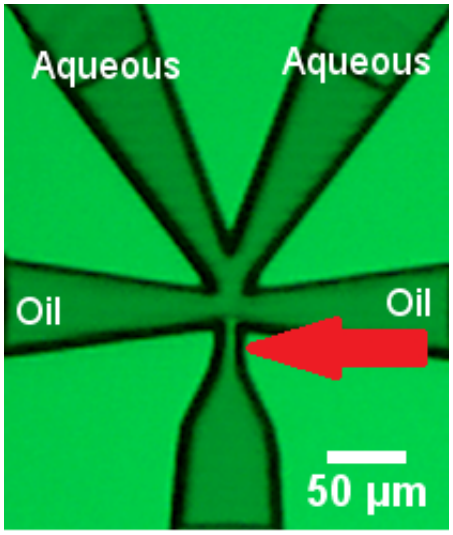

Figure 3.8: The flow focusing nozzle that is being investigated. Two continuous oil inlets shear the aqueous phase. The red arrow indicates the droplet production constriction that is being modified.

SU-8 2005 photoresist (Microchem) was spin coated onto a 3" Silicon wafer at a thickness of 5 μm and baked. After baking, the wafer was placed in the DWL where a 365 nm laser rastered across the surface and selectively exposed the photoresist. After another baking step, the resist was developed and the nozzle pattern remained.

The lithography process was repeated again for the larger channels of depth 25 μm this time using SU-8 2025 photoresist. Verification of the resist thickness was measured using a Dektax XT surface profiler. This is a stylus-based step measurement instrument, which can scan profiles of length 10 mm. Maximum step size is 1000 μm and the vertical resolution of the stylus is $\sim$ 0.3 Å. The average SU-8 2005 height measured was 4.2 $\pm$ 0.2 μm & the SU-8 2025 had average height of 22.17$\pm$0.1μm.

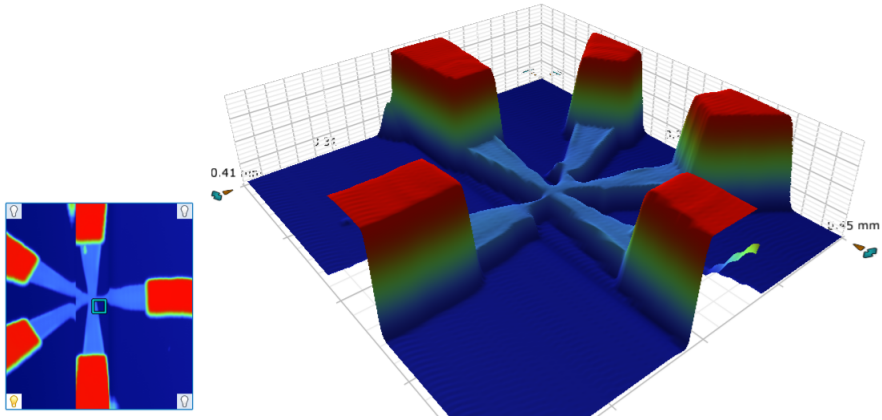

Figure 3.9: 3D mapping of SU-8 height with the Dektak XT shows the geometric constriction during droplet generation.

3.2.3 Experimental Methods

The droplet generation experiment was performed using PBS buffer (pH 7.4) as the aqueous phase and fluorinated oil (HFE 7500, Novec, 3M) as the oil phase. Droplets were stabilised with a block-co-polymer surfactant dissolved in the oil phase (5% w/w). A schematic of the droplet generation is shown in figure 3.11

Each solution (oil and buffer) was injected into the microfluidic device using Hamilton 2500 μl (Oil) and 250 μl (buffer) syringes driven by a syringe driver (Harvard Apparatus PHD 2000). Polyethylene tubing (Smith Medical) of inner diameter 0.36 mm and outer diameter 1.09 mm was used to interface with the microfluidc device.

During the experiment, the PBS buffer was kept constant at a flow rate of 40 μl/h. The oil flow rate was increased and the droplets were imaged at the outlet of the device. Diameters of the droplets were measured using ImageJ software.

Figure 3.10 shows the diameter change of droplets produced with varying oil flow rates. Droplet size is inversely proportional to the oil flow rate Q_O. The

geometric constriction allowed for large shear forces to be produced within the device. This generates high frequency small droplets down to 4 μm. The use of a block co-polymer surfactant reduced the interfacial tension of the two phases and the use of a low viscosity oil (around 1.2 cP) enabled the chip to overcome high hydrodynamic resistances that are experienced with more viscous oils [21]. Silicon oil at around 19 cP and mineral oil at 123 cP would not allow stable femtolitre sized droplets to be produced [3].

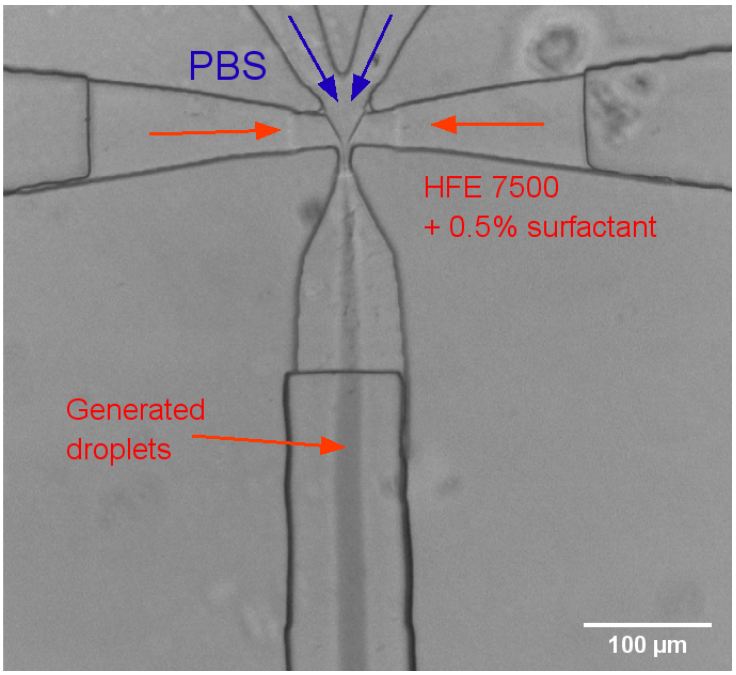

Figure 3.10: Generation of droplets was performed using a 5 μm high by 6 or 10 μm wide flow focussing nozzle. HFE 7500 oil with 0.5% block copolymer surfactant was the continuous phase with PBS buffer as the discontinuous phase.

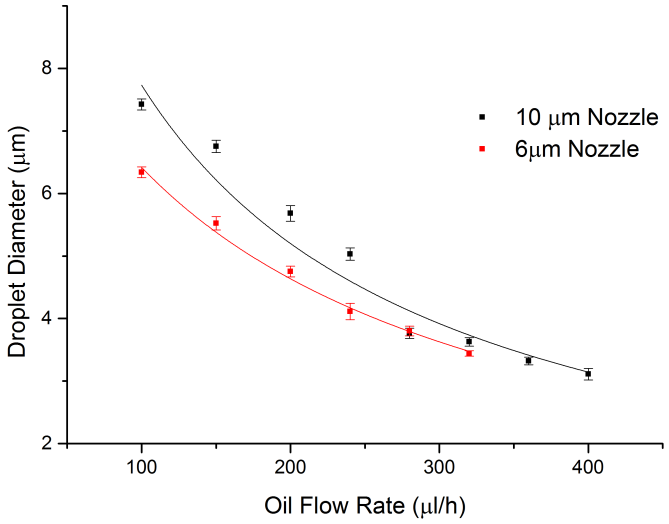

Figure 3.11: Droplet diameters decrease at a rate inversely proportional to the oil flow rate. In the 6 μm nozzle, the droplet production became unstable above Q_O = 320 μl/h. n = approx. 350 droplets per point.

3.2.4 Summary

From this data, it can be concluded is that it is possible to produce 4 μm droplets in a flow focusing nozzle where the constriction geometry is 10 x 5 μm and 6 x 5 μm

3.3 Single Enzyme Detection

The β-galactosidase/fluorescein di-β-galactopyranoside (FDG) reaction (see section 3.1) is the reporting element of the single molecule immunoassay. The β-galactosidase enzyme is the final component of the bead-based immunocomplex and its reaction with FDG shows the presence of target biomarker. Showing the viability of this reaction within droplets is key to single molecule detection.

3.3.1 Pure Fluorescein Detection

Droplets of fluorescein were produced in the microfluidic device to ensure detection was possible. The concentration of fluorescein solution prepared was between 5 and 20 μM. Each concentration of fluorescein was injected into the microfluidic device in the aqueous phase inlets. Droplets were formed in the flow focusing device as described in section 3.2.3. The droplets were then trapped and their fluorescence intensity measured through fluorescence microscopy. The fluorescein was excited with an FITC filter set (excitation 475 $\pm$ 35 nm, Dichoric mirror 508 nm and emission 530 $\pm$ 43 nm). Figure 3.12 shows the fluorescein solution when injected into the aqueous inlets and imaged through the FITC filter set.

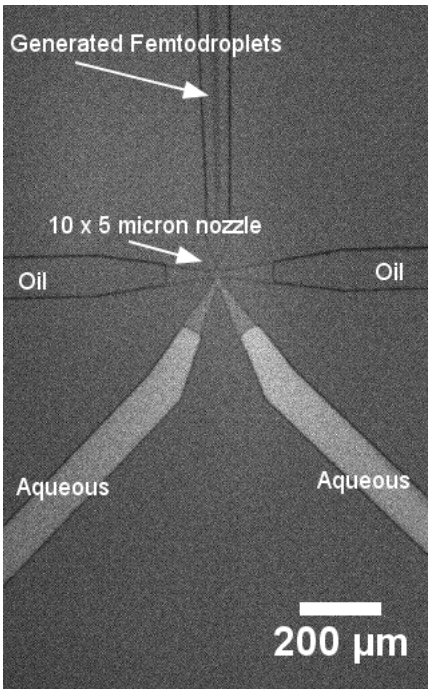

Figure 3.12: Pure fluorescein solution being injected into the aqueous inlets of the device, fluorescence is observed before droplet generation has occurred. The fluorescence is observed through an FITC filter.

Example images of droplets of fluorescein trapped in the microfluidic device are shown in figure 3.13. These droplets (5 μm in diameter) were imaged

and their intensities measured. The measured fluorescence intensity against prepared fluorescein concentration is shown in figure 3.14. This shows a good linearity with coefficient of determination, $R^2 = 0.99$. This data provides a tool for converting measured pixel intensities into fluorescein concentrations and also shows the maximum observable concentration. The Andor iXon camera used to take the images stores pixel intensities in 14 bit integers, leading to a maximum pixel value of 2^{14} (16384 units). From the linear fit of figure 3.14, this corresponds to a fluorescein concentration of ~ 38 μM. When measuring fluorescence of droplets, a droplet is considered to have a fluorescent signal when its intensity is over 3 times the standard deviation of the background intensity. This was used in all experiments in this chapter where fluorescence is observed.

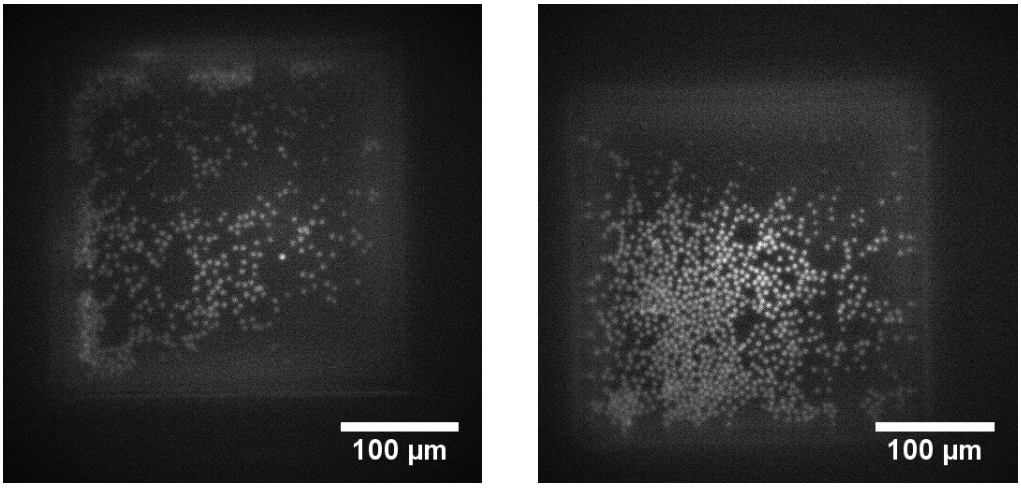

(a) **(b)**

Figure 3.13: Droplets of fluorescein generated through a 10 μm flow focusing nozzle were trapped in a pressure actuated trap (shown in figure 2.1) and their fluorescence intensities measured. A standard curve of intensity was then plotted. a) 5μM fluorescein, b) 10μM fluorescein.

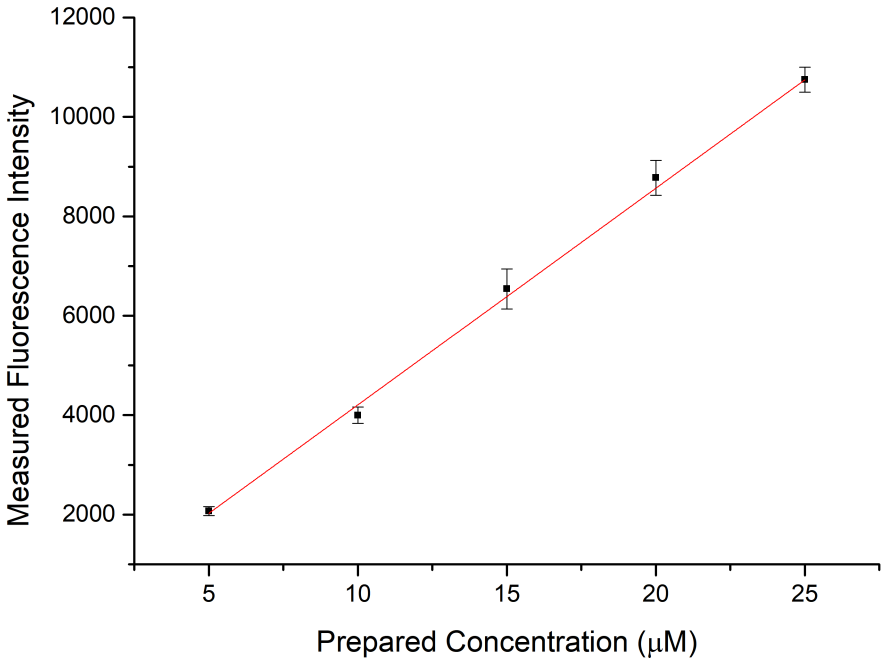

Figure 3.14: Average intensity of droplets produced from pure fluorescein solution. Linearity is good and shows the limit of measurement of 38 μM. Fluorescence acquired with EM gain = 200 and exposure time 0.1s.

3.3.2 Droplet Polydisperisty

During single enzyme molecule detection experiments it is essential that all droplets are monodisperse and of a reasonable diameter (5 μm or less). This is because polydisperse droplet populations can contain smaller droplets that will evolve higher effective concentrations of fluorescent product over a shorter time. After the 10 minute incubation period of the β-galactosidase/FDG reaction, when imaged, the droplets vary in fluorescence intensity. An increase in a single droplet intensity compared to the average droplet intensity is a sign of multiple enzyme occupancy within a droplet. This multiple occupancy is first controlled when the enzyme concentration to be measured is chosen, as the capture of enzymes is Poissonian. This means that the encapsulation is a random event and infers some statistical variation. The concentration is chosen so that the average occupancy of a droplet is much less than 1. Therefore in one measurement, the majority of droplets will contain no enzyme while few will contain 1 (see table 1.3 in section 1.3). Even at some average occupancies less than 1, there is still a finite probability of multiple enzyme occupancy. The elimination of this multiple occupancy is essential for single molecule detection. Elimination of polydispersity can be achieved through quality lithography,

If the droplets produced are too large, the effective concentration of fluorescent product will be reduced in the droplets. Droplet volume, and therefore concentration, scale with r^3, so a droplet of diameter 8 μm (that would normally evolve a fluorescent product concentration of $\sim$ 24 μM) would have a fluorescein concentration closer to 3 μM. Even if these droplets were incubated at a longer time to reach the higher concentration, this would be in excess of 1 hour, reducing the throughput of measurements significantly. The fluorescein may also leak from the droplets on that time scale[148]. Figure 3.15 shows a single enzyme molecule detection experiment where the droplets produced were

of diameter 8 μm. The resulting fluorescence image shows a signal that is not greater than 3 S.D above background.

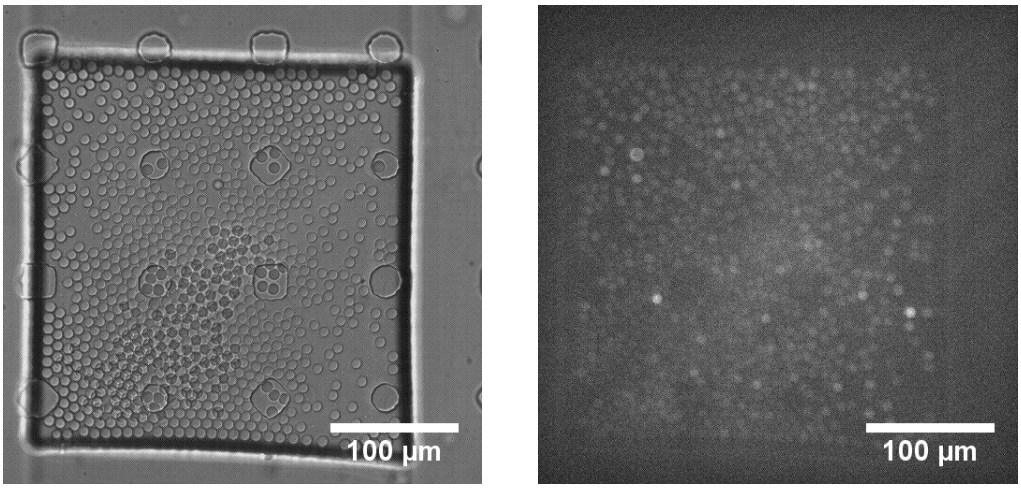

(a) **(b)**

Figure 3.15: a) 8 μm Droplets produced through a 10 μm flow focusing nozzle. b) Fluorescent signal developed within the droplets was close to the lower limit of detectable concentration. The droplet intensities are almost comparable to the background. Excitation = 465-495nm, Emission = 515-555nm. Exposure time = 0.25s.

3.3.3 Single Enzyme Detection

To carry out a single molecule enzyme experiment, the microfluidic chip was set up as follows. Samples were prepared from aliquots. β-galactosidase was prepared from stock by diluting with PBS (pH 7.4) + 0.1% Tween-20 to concentrations of 9.4 pM, 940 fM and 94 fM. These concentrations correspond to a droplet occupancy of 0.1, 0.01 and 0.001 respectively. 50 μl of 2 mM Fluorescein di-β-galactopyranoside (FDG) was diluted to 200 μl (500 μM) with PBS + 0.1 % Tween-20 (pH 7.4). Fluorinated oil with a block-copolymer surfactant (5 % w/w) to stabilise the droplets was loaded into 2500 μl syringes (Hamilton 1002) and placed in a syringe driver. β-galactosidase and FDG were loaded into 250 μl syringes (Hamilton 1725) and placed in a second syringe pump. Polyethylene

tubing was attached to the syringe needles and interfaced with the PDMS microfluidic device. Manufacture and preparation of the microfluidic device can be found in methods chapter 2. The samples were injected into the device and flow rates were adjusted until stable droplet generation was achieved.

When the droplet generation was stable, the flow was diverted into the trapping region through actuation of the control valve. The valve was activated through introduction of air through Tygon tubing. A pressure of 30-40 PSI was typically used (variations from device to device cause variations in required sealing pressure). When sufficient droplets were flowing through the trapping region, the trapping valve was activated. This valve trapped droplets in a 300 x 300 μm chamber capable of holding 5 x 10^4 droplets. The droplets were held for a period of 10 minutes before being imaged through an FITC filter. The filter excitation = 465-495 nm and emission = 515-555 nm. Images were analysed using a MATLAB script which first analysed the bright field image and found droplets and marked them with circles. Then, it used this as a mask to measure the intensity within each of the detected circles. Droplets which displayed a signal more than 3 times the standard deviation of background were considered a positive signal.

Figure 3.16 shows a bright field and fluorescence image of a single enzyme counting experiment. The prepared concentration of β-galactosidase was 9.4pM corresponding to an average droplet occupancy of 0.1. Counting of droplets in this case yielded an average occupancy (Number of fluorescent, therefore enzyme containing, droplets/Total number of droplets) of 0.093. This corresponds to a measured concentration of 8.78pM. Note in the fluorescence image that some droplets appear to be of a higher fluorescence intensity than others. This is due to the Poisson statistics driving the enzyme capture. Equation 3.6 shows the probability of observing k events $P(k)$ of a capture event with average success λ. At an average of 0.1 enzyme molecules per droplet there is a

0.4% chance of dual molecule occupancy. This is $\sim$ 20 droplets in a full trap of 5 x 10^4 droplets.

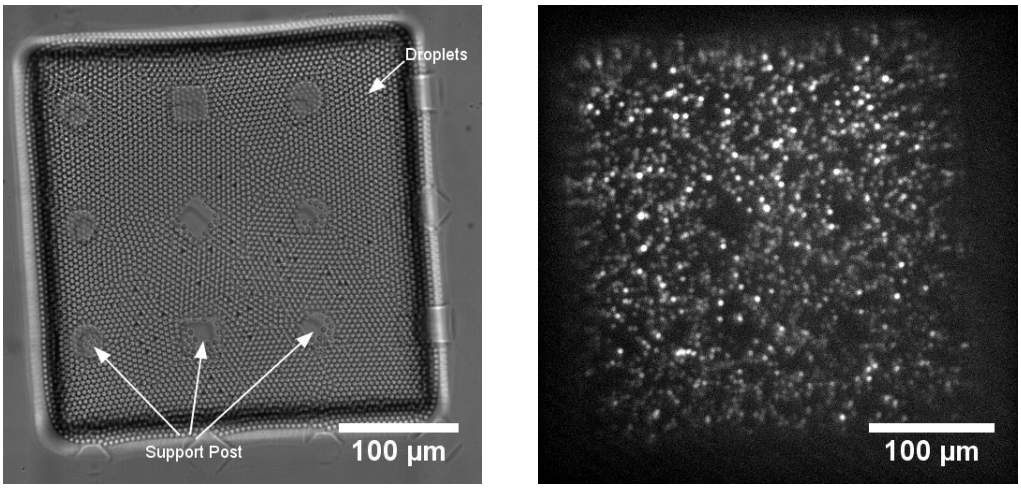

(a) **(b)**

Figure 3.16: a) Droplets containing β-galactosidase enzyme, trapped within the microfluidic device. The concentration prepared = 9.4 pM b) After 10 minutes of incubation, a fluorescence image is taken. Excitation = 465-495nm, Emission = 515-555nm. Exposure time = 0.25s.

$$P(k) = e^{-\lambda}\frac{\lambda^k}{k!} \tag{3.6}$$

Figure 3.17 shows the bright field and fluorescence images of an experiment where the prepared concentration was 940 fM (occupancy = 0.01). As expected, lowering the enzyme concentration reduces the number of fluorescent droplets. Plotted in figures 3.18 and 3.19 is the relationship between prepared concentration of β-galactosidase and measured concentration through single enzyme detection experiments.

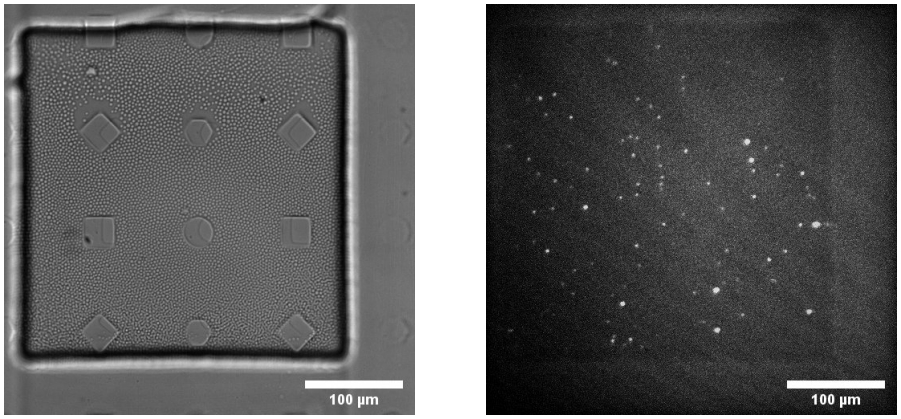

(a) **(b)**

Figure 3.17: a) 4.4μm diameter droplets trapped within the microfluidic device. The concentration prepared = 940 fM = 1 in 100 droplets contain an enzyme. b) After 10 minutes of incubation, a fluorescence image is taken. Excitation = 465-495nm, Emission = 515-555nm. 0.25s exposure time.

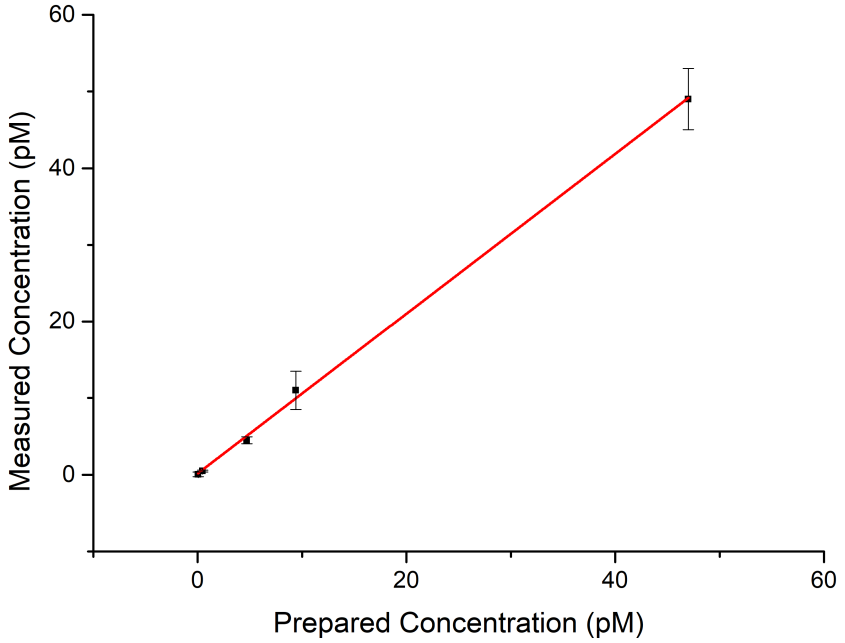

Figure 3.18: Prepared concentration vs measured concentration of β-galactosidase encapsulated in 4 μm droplets. Inset: Zoomed view of lower measured concentrations from 47 fM to 9.4 pM. The lowest detected concentration was 47 fM which was equivalent to 3 fluorescence droplets within a trap. n = 3.

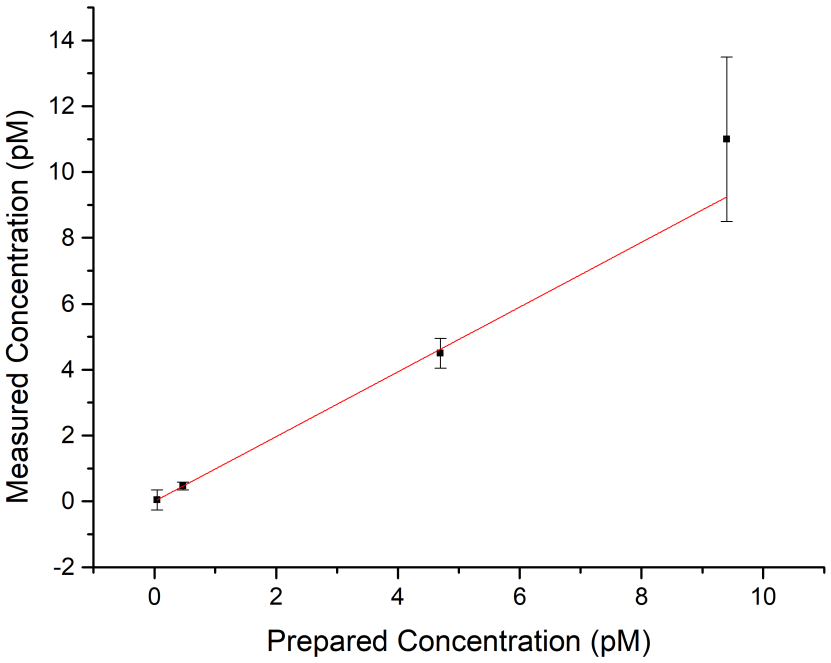

Figure 3.19: Prepared concentration vs measured concentration of β-galactosidase encapsulated in 4 μm droplets shown without 47 pM data point for clarity of lower concentrations. The lowest detected concentration was 47 fM.

3.3.4 Summary

From this data, it can be concluded that it is possible to detect single molecules of β-galactosidase within 4 μm droplets through observation of β-galactosidase reacting with FDG.

3.4 PSA Detection

3.4.1 Objectives

This section will show experiments performed to detect PSA using droplet based ELISA. Immunocomplexes were formed on 1 μm polystyrene beads as described in section 2.7.

3.4.2 Immunocomplex Preparation

Primary anti-PSA antibodies (monoclonal mouse IgG, R&D Systems) were covalently bonded to 1 μm amine-functionalised polystyrene beads using a gluteraldehyde crosslinking kit (Polysciences). Reported in Shim et. al.[3], the conjugation of primary antibodies to polystyrene beads causes fluorescence when excited at a wavelength of 560 nm and observed at 630 nm (Texas Red). Figure 3.20 shows the fluorescence present when 5 μl of fully conjugated immunocomplexes on beads were deposited on a glass slide. The image was taken through a Texas Red filter (excitation = 559 nm, emission = 630 nm). Figure 3.21 shows the fluorescence when many beads collect in a region of the PDMS device (again imaged through a Texas Red filter). However, when trapped within femtodroplets, the fluorescence could not be observed. It may be that the fluorescence emitted by the bead conjugates is too weak to detect or that the

fluorescence is from the beads themselves. Intrinsic protein fluorescence occurs at wavelengths much shorter than that of the emission filter of Texas Red (Tryptophan is excited at 280 nm and emits at 350 nm)[197].

Uv-Vis spectroscopy has shown that the absorbance at 280 nm of stock anti-PSA antibody verifies the stock concentration (3.3 μM). After conjugation, the absorbance dropped indicating an antibody concentration of 36 nM indicating protein conjugation had occurred.

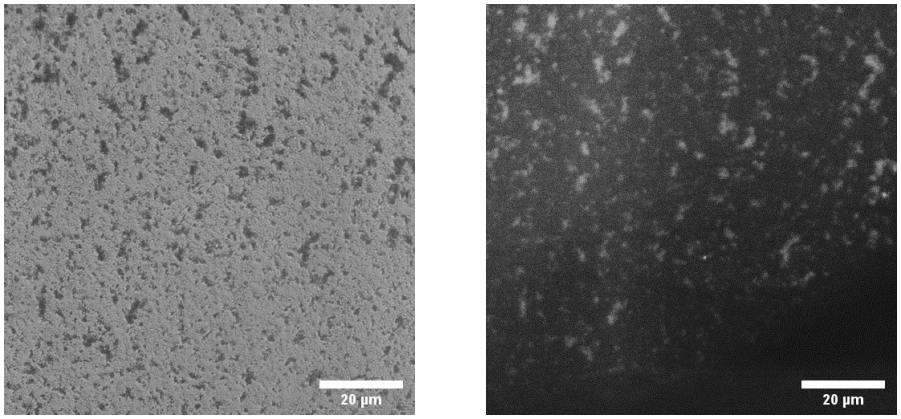

(a) **(b)**

Figure 3.20: a) 5 μl of solution containing 1 μm beads with PSA immunocomplexes conjugated were deposited onto a glass slide b) Fluorescent signal was observed when illuminated with a Texas Red filter (Excitation = 559 nm, emission = 620 nm).

After primary antibody conjugation, 100 μl of the biomarker sample was incubated in 100 μl of 24 pM bead solution for 1 hour at room temperature with gentle shaking. The beads were washed through centrifugation and resuspended in 100 μl of fresh PBS buffer + 0.5% Tween-20 (pH 7.4) 2 times. 100 μl of 17 nM anti-PSA, biotinylated detection antibody, was added and incubated for 1 hour as before. The beads were washed 6 times through centrifugation and resuspended in 100 μl of PBS + 0.5% Tween-20. 100 μl of 5 nM streptavidin-conjugated β-galactosidase solution was added and incubated for 1 hour as before. The solution was washed 6 times, resuspended in 200 μl of PBS + 0.5%

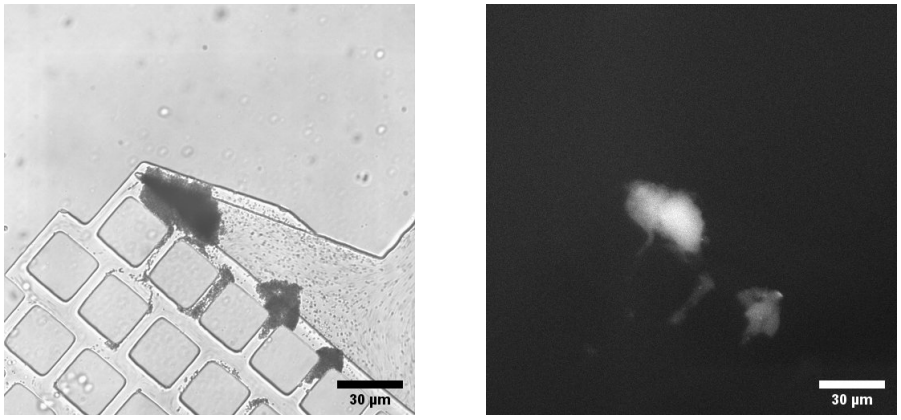

(a) **(b)**

Figure 3.21: a) A bright field image of the aqueous inlet of the immunoassay device showing a high concentration of 1 μm diameter beads with a PSA immunocomplex conjugated. The beads accumulated within the PDMS device inlet filter. b) A fluorescence microscopy image showed fluorescence of the beads within the PDMS device through a Texas Red filter (Excitation = 559 nm, emission = 620 nm).

Tween-20 and sonicated for 30 minutes before injection in to the microfluidic device.

3.4.3 Detection of PSA Biomarker in Droplet Based ELISA.

To perform a droplet based ELISA experiment, immunocomplexes were prepared on 1 μm amine-functionalised beads as described in section 2.7. This sample solution was injected into the microfluidic device as described in the single enzyme detection experiments (section 3.3.3). In this experiment the 2 aqueous phases were the bead bound immunocomplex solution and the FDG substrate (500 μM). The oil phase was the same used in single enzyme detection experiments (HFE 7500 and 5% w/w block copolymer surfactant).

After generation of femtodroplets, the aim is for a single bead to be present within each droplet (see figure 3.22). This is so a single enzyme is digesting

the substrate and the number of fluorescent droplets can be counted as before. As each immunocomplex should contain only one enzyme, the number of fluorescent droplets equals the number of PSA molecules. The concentration of immunocomplex conjugated beads is known at the start of the experiment (typically 12 pM) so the concentration of PSA can be calculated from the ratio of fluorescent droplets and total bead containing droplets, multiplied by the known bead concentration.

Figure 3.23 shows a PSA detection experiment with a PSA sample concentration of 30 pM. The generation of droplets was not ideal in this experiment as some larger droplets containing many beads were present.

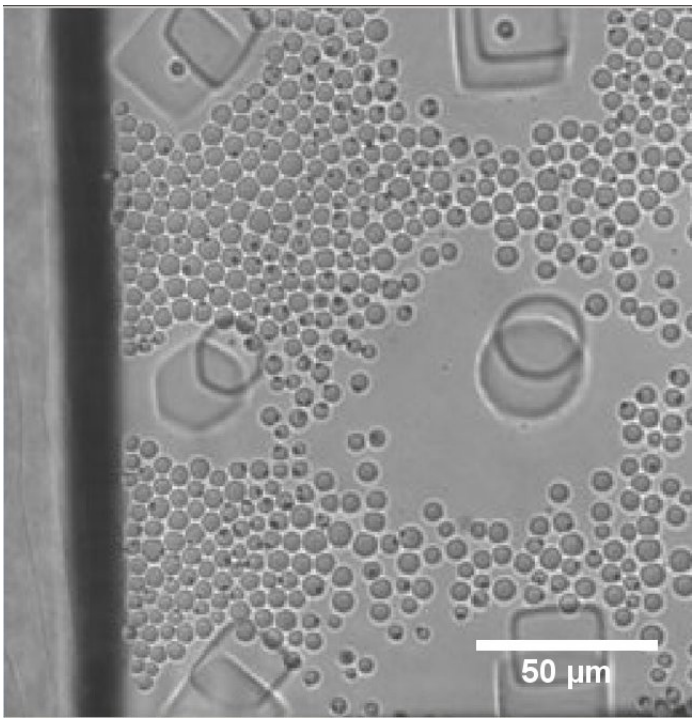

Figure 3.22: This bright field image shows the 1 μm beads contained within droplets. Without the individual bead fluorescence it is still possible to determine the presence of beads within droplets with some scrutiny.

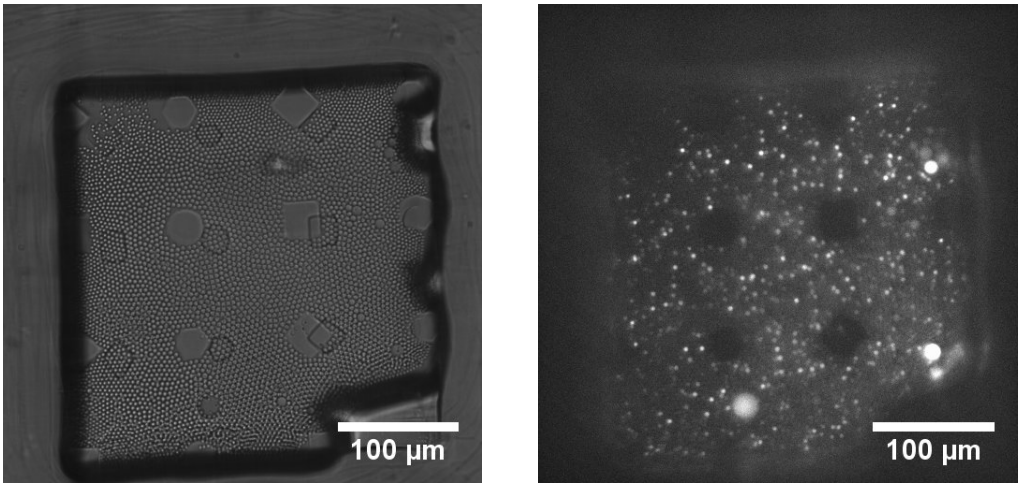

(a) **(b)**

Figure 3.23: a) A bright field image droplets trapped within the PDMS device containing a 30 pM PSA sample. b) A fluorescence microscopy image showed fluorescence of the droplets through an FITC filter (Excitation = 465-495 nm, Emission = 515-555 nm. Exposure time = 0.25 s.)

3.5 Chapter Summary

The aims of this chapter were to expand the detection limits of a microfluidic single molecule detection system to detect cancer biomarkers. During initial experimentation to determine single enzyme concentration, the droplets that were produced were not able to be detected using fluorescence microscopy. To troubleshoot this experiment, the kinetics of the β-glactosidase enzyme was investigated and this chapter lays out the further troubleshooting steps of the individual components of the immunoassay experiment. The enzyme was found to be active and processing the substrate at a rate that is within previously reported values. The optics of the experiment were investigated and found to be inadequate to detect the level of fluorescence product being formed within the droplets. Polydisperse droplet formation was addressed through the analysis of photolithography techniques and nozzle size. When the droplets were of an acceptable monodispersity, attention was focussed on the biological components. The acquisition of new optics allowed for the detection of fluorescent prod-

ucts from β-galactosidase and measurement of concentrations down to 47 fM. The conjugation of antibodies onto polystyrene beads was confirmed through UV-Vis spectroscopy although they did not exhibit the fluorescent properties previously reported, only when many beads collected together. This could be indicative of a weak signal that is unable to be detected on a single bead level. This made PSA detection difficult as the method of inferring concentration depends on knowing the number of droplets containing beads. As the beads are 1 μm they can be elusive optically. Manual counting of beads was possible although some observations were dubious as to whether beads were being observed or some other foreign particle. The observation of fluorescence would be a strong indicator of bead presence and the use of fluorescent dyed beads would be a useful addition to the experimental setup. The characterisation of each element led to preliminary observations of a PSA immunoassay, however, the full measurement capabilities of the microfluidic device were not observed.

To further this project, experiments would include detection of a range of PSA concentrations possibly through the use of fluorescently tagged beads where the fluorescenct properties are well characterised. Multiplexing of the system can be fairly easily achieved with coded beads to detect multiple biomarkers. One of the main losses in the device is the number of droplets produced that are wasted due to incubation times of trapped droplets. The integration of an in-line detection system may improve the number of samples that are able to be measured at any given time.

Chapter 4

Pressure Induced Deformation of Channels after Mineral Oil Absorption

This chapter will describe the experiments undertaken to measure the pressure inside a PDMS microfluidic device. The measurement of pressure within a channel containing water under different flow rates using a unique measurement method will be presented. This will be followed by the presentation of experiments using different fluids flowing through the channel and their effect on the pressure measurements. Finally, an analysis of the behaviour of channels after exposure to PDMS soluble oil will be shown. Characterisation of the PDMS before and after oil exposure will be shown with bulk swelling of PDMS, AFM surface characterisation and Raman Spectroscopy data presented.

The device used in this section was a simple serpentine channel with pressure measurement channels extending from the main channel every 50 mm. The layout of the device is shown in figure 4.1. The dimensions of the channel are 250 μm wide, 21 μm high and 470 mm in length with 4 pressure measurement ports. These ports were simply channels that forked off from the main channel and led to a punched outlet. These outlets were interfaced with pressure regulators through tubing and sealed with optical adhesive (NOA 81, see section 2.8).

4.1 Measuring the Pressure of A Microfluidic Channel

The first steps in this project focused on measuring the internal pressure of a PDMS microchannel. The usual approach to take these measurements is through the use of pressure transducers that are connected to the channels. In this project, a new method of measurement was proposed using a pressurised air supply and gas regulators to counteract the internal pressure of the flowing liquid until an equilibrium is reached. To validate the method for measuring pressure, the first experiments used a flow of water within a 21 μm x 250 μm channel at flow rates of 600 - 1800 μl/hr. The device layout in figure 4.1 shows a 470 mm long channel with four pressure measurement ports extending out from the main channel.

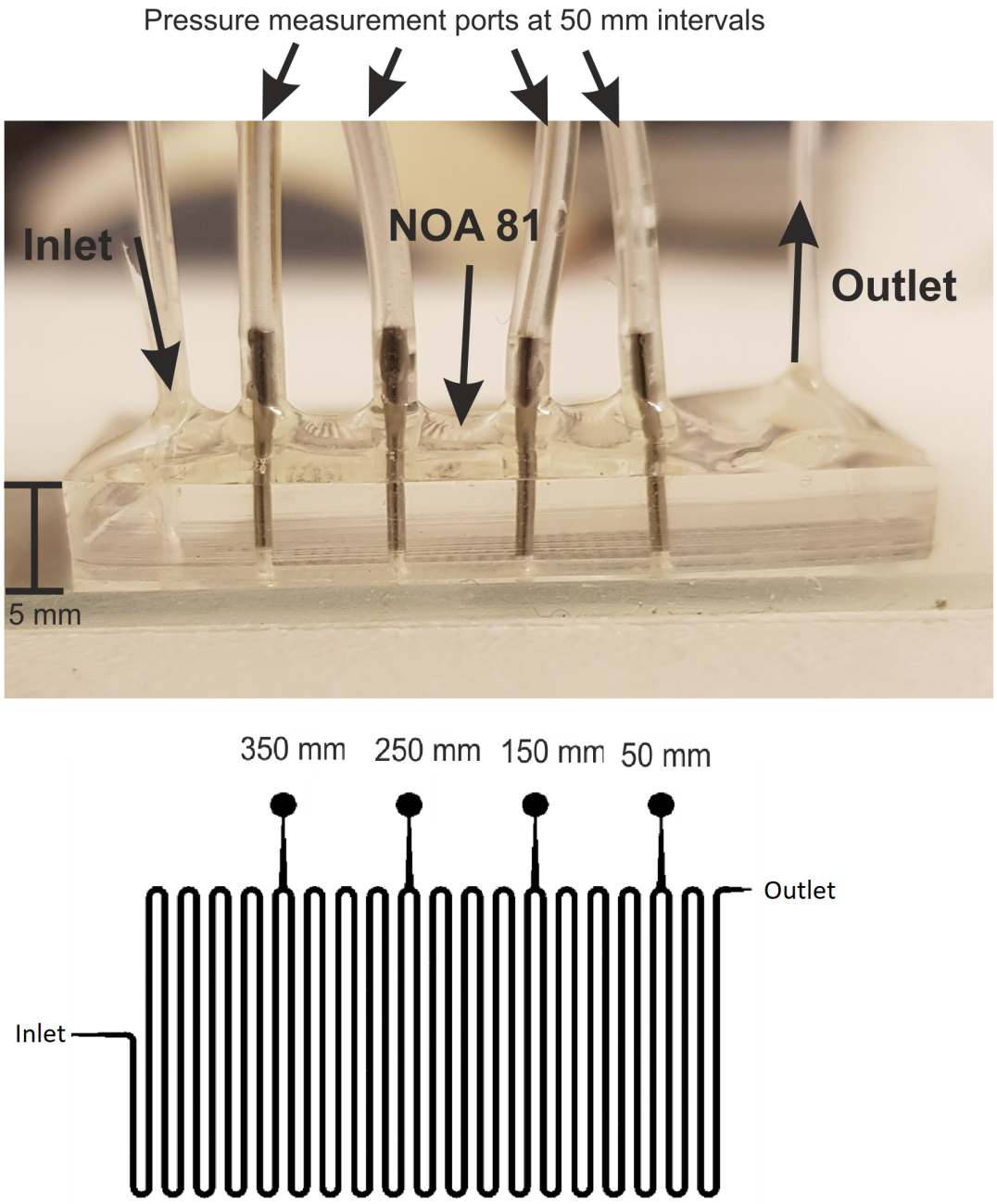

Figure 4.1: The device used in this study comprised of 250 μm wide by 21 μm deep channels. At 50 mm intervals, pressure measurement points are connected to a regulated air supply. A schematic of the device setup showing the 4 pressure measurement ports.

4.1.1 Internal Pressure of a Rigid Channel

The pressure inside a microfluidic channel depends on the material properties of the walls. In the devices used in these experiments, 3 of the walls are made of PDMS (the fourth being glass) which (as described in section 1.4) deforms under flow due to the elastic nature of the polymer. This means that under the same flow rates, a rigid channel will experience a higher internal pressure as the walls are not allowed to deform and increase the channel cross sectional area. To calculate the pressure values for a rigid walled channel, the microfluidics package of COMSOL® Multiphysics was used. The geometry of the device was imported and the Navier-Stokes equations for Stokes flow were solved. This simulation resulted in the pressure values shown in figure 4.2.

4.1.2 Internal Pressure of PDMS Microchannels due to Elastic Deformation

The measurement of pressure within a microfluidic channel was performed with water at 21 °C and a viscosity of 8.9 x 10^{-4} Pas. The fluid was introduced into the channel at a flow rate of 600 μl/hr through the inlet. As the fluid flowed through the channel, the pressure regulators were adjusted so that the pressure equalised at the interface of the channel and the measurement point. An example of this equilibrium can be seen in figure 4.4

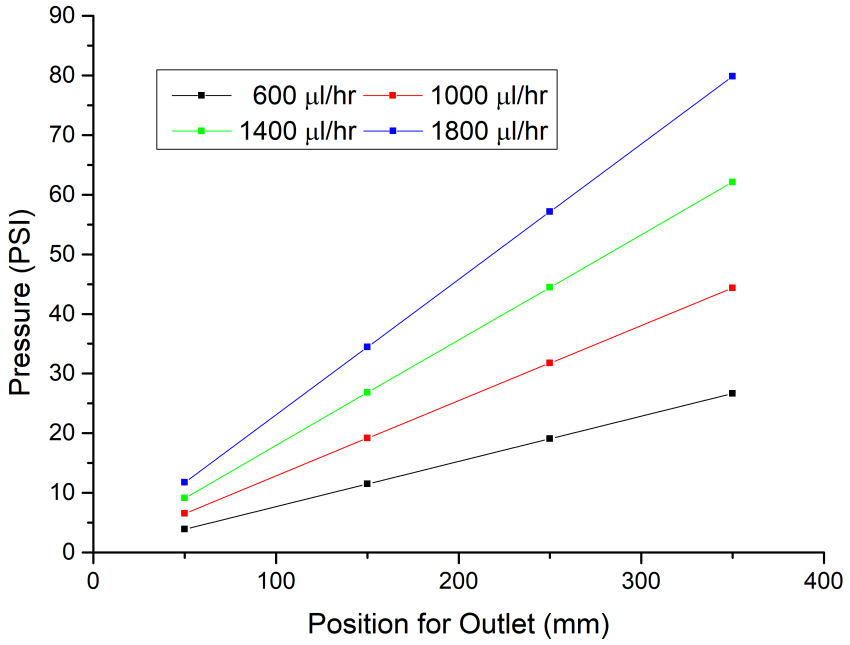

Figure 4.2: When the channel walls are simulated to be non-deformable, a linear relationship is observed between the channel position and internal pressure.

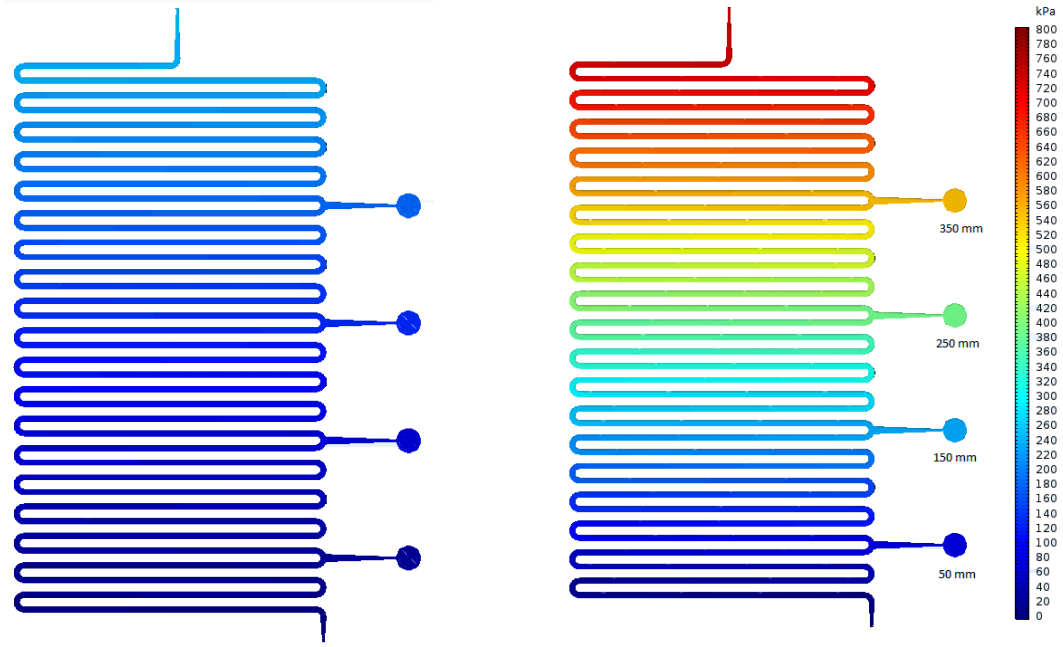

(a) **(b)**

Figure 4.3: Pressure gradient of a non compliant microchannel under a flow rate of (a) 600 μl/h and (b) 1800 μl/h. The channel geometry is 21 μm x 250 μm x 470 mm. Reynolds number, Re = 1.3 - 3.8.

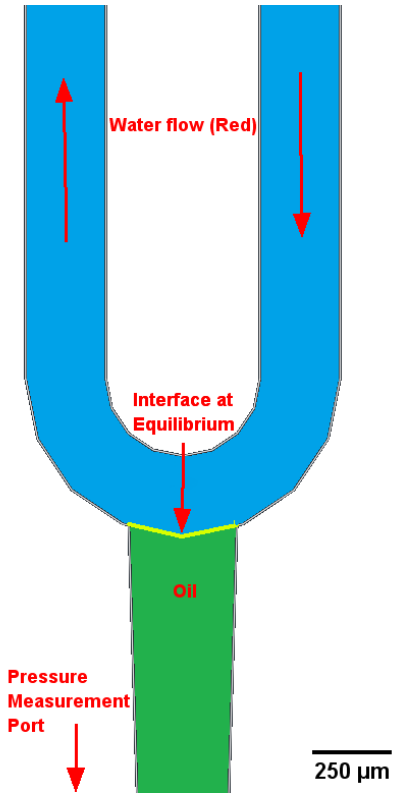

Figure 4.4: A pressure measurement point within the microfluidic device. Here the flow of fluid has been initiated in the main channel (water) and the air pressure off chip has been gradually increased to match the internal pressure of the liquid. When equilibrated, an interface is formed between the flowing fluid and external gas supply.

When all four regulators were in equilibrium with the fluid flow, the pressures were read. For flow rates of 600 μl/hr to 1800 μ/hr the resulting measured pressures are shown in figure 4.5. The pressure is no longer linearly dependant on channel position as the PDMS channel in able to deform under the pressure driven flow due to its elastic properties. The higher the pressure, the higher the deformation which increases the channels cross sectional area and reduces the pressure compared to a rigid channel. This measured reduction confirms that deformation is taking place.

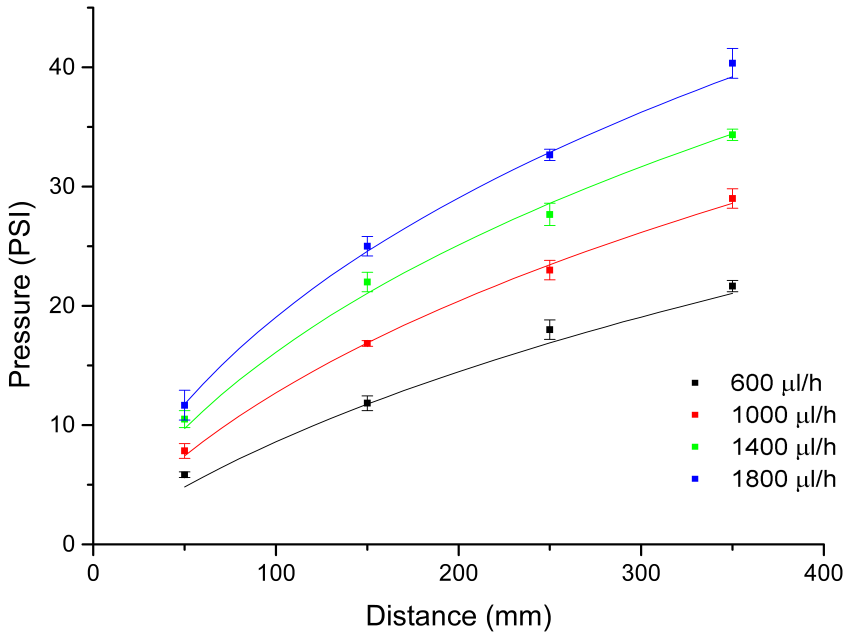

Figure 4.5: The pressure profiles of a microfluidic channel at varying flow rates shows a non-linear relation as expected in a deformable channel. Symbol = experimental data, solid line = theoretical calculation.

The pressure measurements have been plotted along with theoretical pressure values from the model proposed by Gervais et. al.[170] where the deforma-

tion of the PDMS channel is modelled as flow between tapering plates resulting in equation 4.1 (derivation of this equation is shown in section 1.4), where Q = fluid flow rate, h_0 = channel initial height, E = Young's modulus, α = fitting parameter, μ = fluid viscosity, L = channel length, z = channel position, p(z) = channel internal pressure and W = channel width. This equation was solved for p(z) in MATLAB (MathWorks, USA) at each flow rate using the Young's Modulus measured with nanoindentaion (section 4.5) where E= (2.80 ± 0.03) MPa. Fitting the data with these theoretical calculations showed that for this system the proportionality constant $\alpha = 0.7$ which is in line with Gervais' predictions that α should be of order 1.

$$Q = \frac{h_0^4 E}{48\alpha\mu(L-z)}\left[\left(1+\alpha\frac{p(z)W}{Eh_0}\right)^4+1\right] \tag{4.1}$$

From this plot it can be seen that this method for measuring pressure on chip with the equilibrium of pressurised air and fluid flow is valid and agrees with the model. The fact that gas is able to permeate through PDMS does not appear to affect the measurements taken. It was theorised that there may be sufficient surface area of the channel to allow air to escape at the pressure measurement points, however, this does not appear to be the case even at pressures exceeding 40 PSI.

4.2 Initial Pressure Measurements with Mineral Oil

The next step was to increase the viscosity of the working fluid within the channel to measure the difference in measured internal pressure. The motivation was to be able to measure the internal pressure and infer the viscosity of a fluid on-chip. The candidate fluid was mineral oil (Sigma) as it had a viscosity 30 x that of water and found to have high solubility in PDMS[209]. The viscosity of the mineral oil was measured using a parallel plate rheometer and found to have a viscosity of (35.6 ± 0.1) mPas.

The viscosity of the mineral oil was measured on a TA Instruments dynamic stress rheometer (SR 500). The fluid was stressed between two parallel plates and the shear rate measured:

$$\dot{\gamma} = \frac{v}{h} \tag{4.2}$$

Where $\dot{\gamma}$ = Shear Rate(s^{-1}), v = plate velocity($\frac{m}{s}$) and h = distance between plates (m).

$$\tau = \eta\dot{\gamma} \tag{4.3}$$

Therefore, from a plot of stress vs rate, the gradient gives viscosity:

$$\eta = \frac{\tau}{\dot{\gamma}} \tag{4.4}$$

where η = Viscosity (Pas) and τ = Shear Stress (Pa).

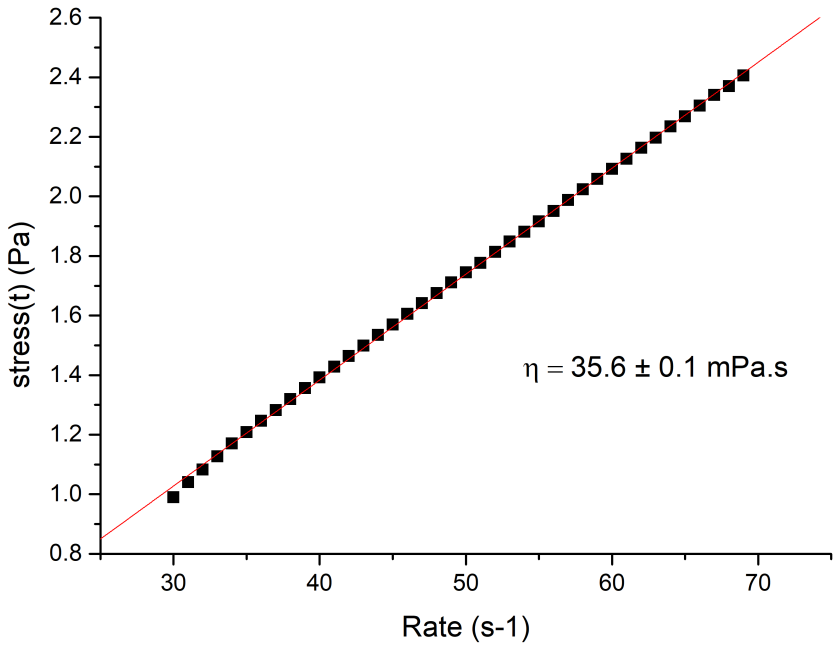

Figure 4.6: Measurement of mineral oil viscosity with a rheometer yields 35.6 ± 0.1 mPas

The oil was then used as the fluid in the chip and the pressure measured. When the viscosity was extracted from the pressure measurements it was found to be between 9 mPas and 11 mPas, 31 % lower than the rheometer measured value. Figure 4.7 shows the pressure drop of the channel as a function of flow rate. The red line is a theoretical calculation of channel pressure from equation

4.1 with flow rates between 40 and 120 μl/h, viscosity 35.6 mPas and Young's modulus 2.8 MPa. The black points show the measured pressure drop and it can be seen that under current assumptions the system is not in a similar state to the previous water pressure measurements. The interaction of mineral oil with PDMS was then investigated as the pressure measurements did not fit with the predicted results.

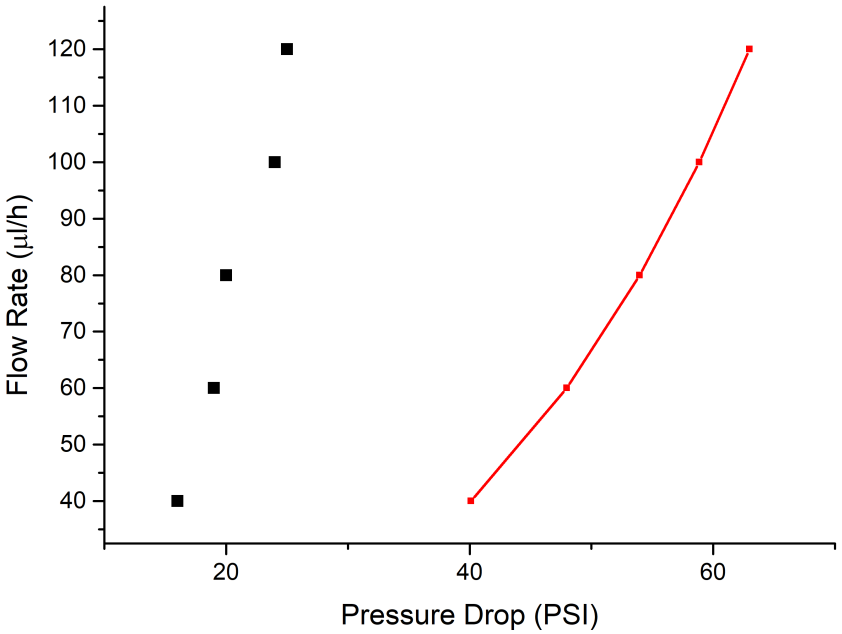

Figure 4.7: Here the red line is the theoretical pressure drop as a function of flow rate for mineral oil of viscosity 35.6 mPas. The black points are the measured values and correspond to a fluid viscosity of 9 mPas.

4.3 Bulk Swelling of PDMS

PDMS is a porous polymer which leads to absorption of certain solvents when exposed. This exposure and subsequent absorption of solvent causes the geometry of PDMS to expand when a swelling solvent diffuses into the polymer matrix. In order to investigate the swelling effects of a solvent, the swelling coefficient, S_∞ is found. S_∞ is the ratio of the polymers swollen geometry at saturation over its initial length. The extent of swelling has been investigated by Whitesides et. al.[210] for various solvents and found swelling coefficients of 1.01 to 2.13 for 38 different solvents.

4.3.1 Bulk Swelling with Mineral Oil

To investigate the extent of the absorption, pieces of PDMS 10 mm x 10 mm x 5 mm were placed in a container of oil and imaged as the oil diffused into the polymer. The surface area of the block was measured and the change over time can be seen in figure 4.8. A final measurement was taken after swelling had concluded, S_∞. The change in surface area over time in figure 4.8 shows a saturation at 3.7 % increase of surface area.

The diffusive process of swelling is characterised by the diffusion coefficient D. The model of solvent diffusion into PDMS presented by Dangla et. al[209] is shown in equation 4.5 where L(t) is the swollen length at time t, L(0) is

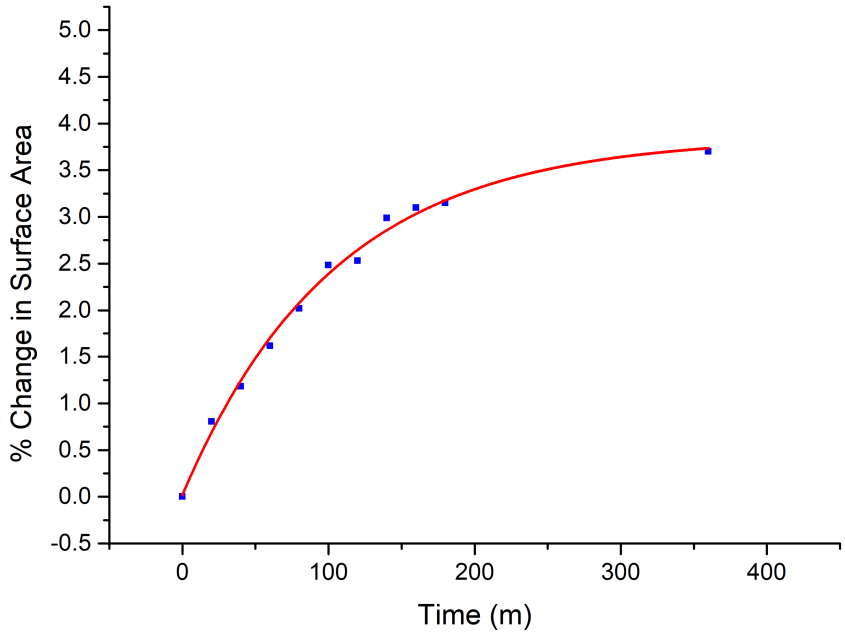

Figure 4.8: Swelling of a PDMS slab over time in mineral oil. The percentage change in surface area shows a maximum swell of 3.7 %, fit with associative exponential.

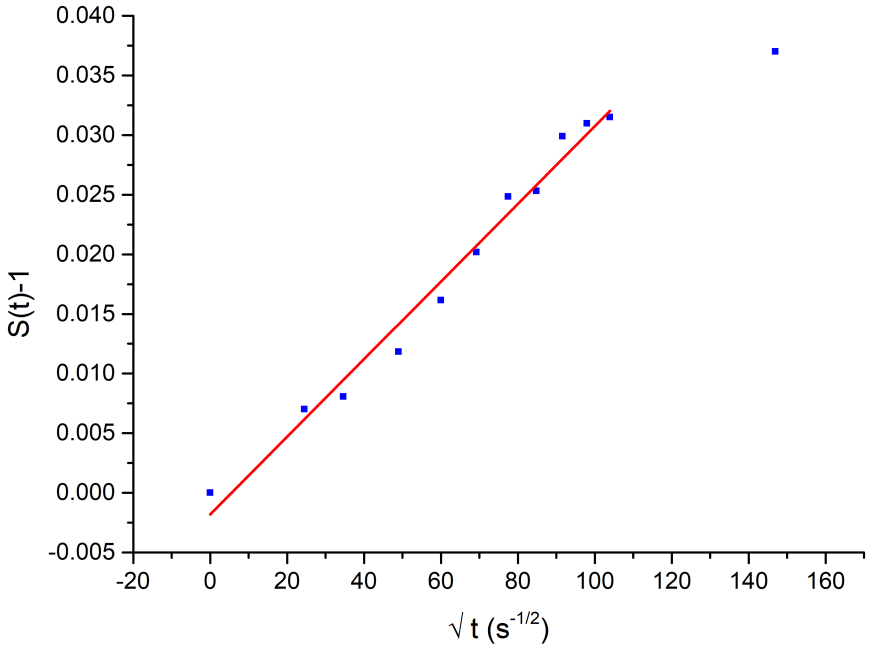

Figure 4.9: The swelling ratio of PDMS against $\sqrt{t}$ gives a linear relationship. This plot is fitted with ewuation 4.5 to extract the diffusion coefficient of mineral oil into PDMS.

the initial length, S_∞ is the infinite swelling coefficient, d is the thickness of the PDMS slab and t is time. This equation is valid before saturation occurs and can be used to estimate the diffusion coefficient, D. Figure 4.9 shows the swelling ratio S(t)-1 plotted as a function of $\sqrt{t}$. A linear fit was applied before saturation and shows good fitting ($R^2 = 0.98$). The slope, β can be used in equation 4.6 to estimate the diffusion coefficient.

$$\frac{L(t)}{L_0} - 1 = (S_\infty - 1)\frac{2}{d}\sqrt{\frac{Dt}{\pi}} \tag{4.5}$$

$$D = \pi \frac{\beta d}{2(S_\infty - 1)}^2 \tag{4.6}$$

For mineral oil in PDMS, the calculated diffusion coefficient, D = (1.29 $\pm$ 0.05) x 10^{-13} $m^2 s^{-1}$. The time of diffusion can be estimated by $t = \frac{x^2}{2D}$ where t is time in seconds and x is the distance of diffusion. The time taken for the oil to diffuse the height of the channel away from the channel (21 μm above the channel ceiling) is equal to 28.2 minutes. We can therefore assume that after a time of 3 hours the PDMS has absorbed sufficient mineral oil to be at a swollen steady state.

4.4 Channel Profile Imaging with Confocal Microscopy

4.4.1 Nile Red and Mineral Oil Solution

The cross section of the microchannel increases under pressure driven flow due to the deformation of the PDMS channel walls. The extent of this change of cross section was investigated with water that is negligibly absorbed by PDMS, and mineral oil that is readily absorbed. To observe the deformation, confocal microscopy was used. Channels were prepared using the same method as used in the pressure measurement investigations however the pressure measurement ports were not punched out and left sealed. Due to the short working distance of the 40 x objective being used ($\sim 200\ \mu$m), the devices were bonded to coverslips of thickness 130 - 170 μm. The first imaging method tried was to dissolve Nile Red dye in mineral oil to make a 1 μM solution and flow this through the channel. The aim was to use this solution to image the oil as it flowed through the channel under various flow rates and observe the pressure driven deformation of the channel. Subsequent investigation showed that Nile red has been shown to diffuse into PDMS[177] and therefore would not be suitable to image oil as it flowed. Figure 4.10 shows the profile of a channel after a Nile red mineral oil solution had been flowed through for 1 hour and then flushed with water to remove fluorophore from the channel. The channel was imaged

using a 532 nm laser as an excitation source. The resulting channel profile is 250 μm x 21 μm (pixel aspect ratio = 4.588).

Figure 4.10: Microchannel profile after flow with a Nile red mineral oil solution. Nile red is absorbed by the PDMS and gives contrast to an empty channel. Channel imaged under no flow after flushing with water. Dimension = 250 μm x 21 μm.

4.4.2 Imaging of the PDMS Water interface

To investigate the deformation of channels under pressure, it was not possible to use the Nile red solution alone. To observe the channel previously, Nile red was removed prior to imaging with water. Here, a fluorescein solution was injected after the mineral oil Nile red solution to image the interface of the channel flow and PDMS. The device design was altered slightly so a thin membrane of PDMS (100 μm) was applied as a channel base so that all walls were PDMS and could be observed. When purging the oil from the channel and subsequently injecting water, it is possible that the water will not fully wet the channel due to a thin film of oil remaining. To ensure the walls of the channel were fully wetted, the Nile red mineral oil solution was flushed with fresh mineral oil to remove and Nile red solution in the channel and then flushed again with fluorescein solution to remove oil. The water flush was continued until the solution had wet the channel walls in the x-y plane and then confocal z-stacks were taken of

the channel. The Nile red was excited with a 532 nm laser and the fluorescein with a 488 nm laser. Figure 4.11 shows the channel profile within the Nile red stained PDMS. Observations of the interface showed no spacial cavities between the two fluorophores indicating the channel was fully wetted.

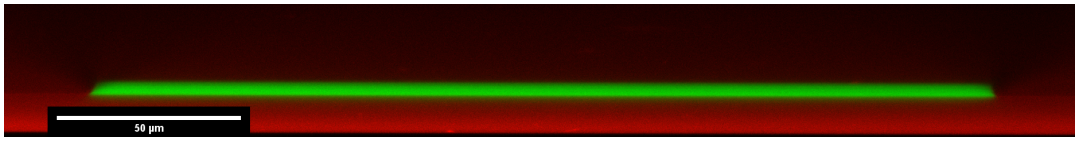

Figure 4.11: An overlay of Nile red and fluorescein fluorescence channels. Imaging the channel with both Nile red and fluorescein allowed the visualisation of the PDMS fluid interface. This shows that the water phase fully wets the channel walls.

4.4.3 Confocal Microscopy of Microchannels Under Pressure

The channels were imaged under the same flow conditions described in section 4.1.2. Under each flow rate, the channel height profile was measured by taking z-stacks at 6 locations along the channel with a z-step of 0.53 μm. For water deformation measurements, the devices were injected with 1 μM fluorescein solution. In the case of mineral oil absorption, oil was flowed through the device at a rate of 40 μl/h for 3 hours before being flushed with fluorescein solution. Each flow rate was allowed to equilibrate for 5 minutes before imaging was performed. z-stacks were analysed in ImageJ by translating the stacks into a z projection before an edge detection algorithm was applied. The maximum

height was extracted and plotted against position and flow rate.

Figure 4.12 show the heights measured when the PDMS was fresh and only fluorescein solution was flowed. The deformation increases as a function of distance along the channel as expected. At the highest flow rate measured, 1800 μl/h, the deformation of the channel was 97.6 % higher than the original channel dimension. The deformations were plotted with theoretical deformations (solid lines) which were calculated from equation 1.17 where proportionality constant, α, was 0.7 as previously calculated, E = 1.35 MPa found from AFM nanoindentation (the results of which are shown in section 4.5) and p(z) were the previously calculated theoretical pressures from section 4.1.2.

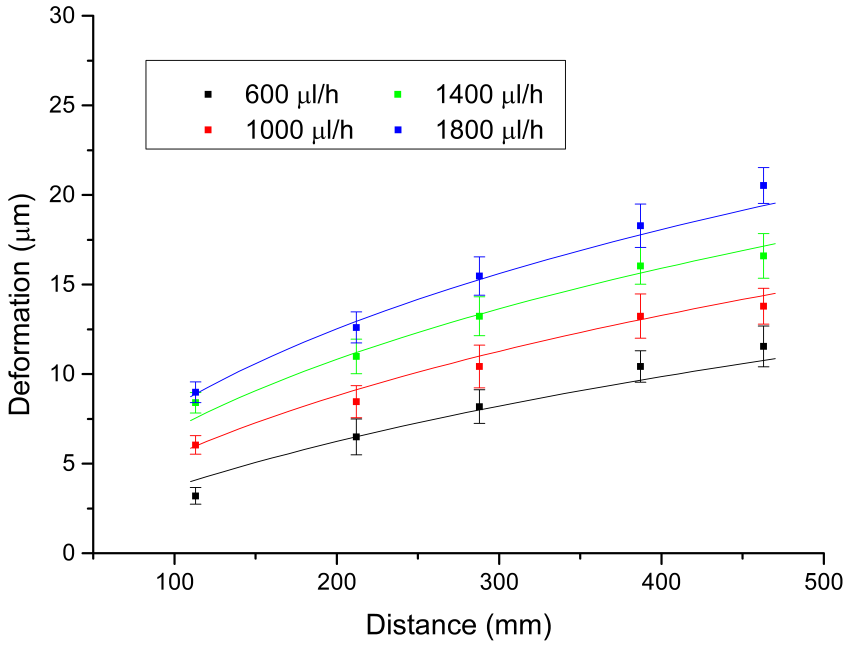

Figure 4.12: Measured deformation (symbols) of fresh PDMS flexible microchannels compared to theoretical deformations (solid lines)

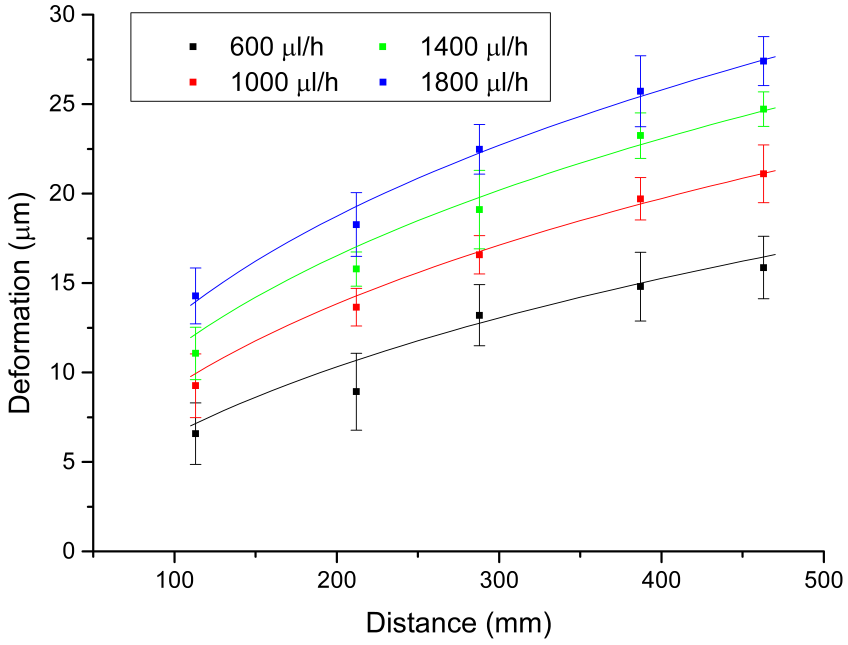

Figure 4.13: Measured deformation (symbols) of flexible microchannels after infiltration of mineral oil compared to theoretical calculations (solid lines). The change in Young's modulus allows the channel to deform further than fresh PDMS.

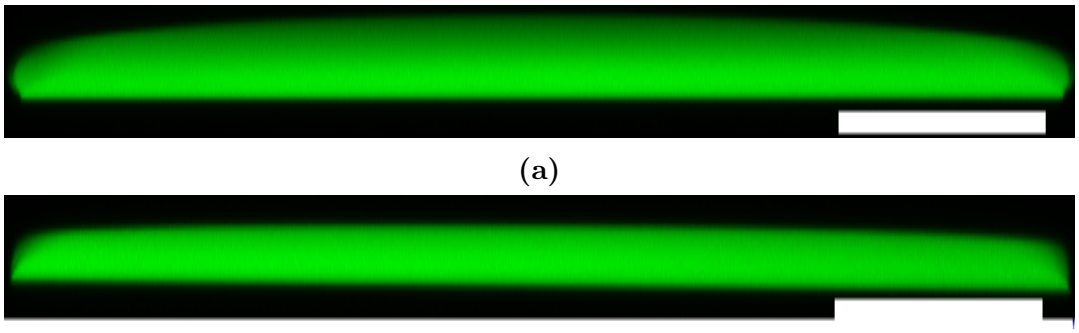

(a)

(b)

Figure 4.14: Confocal microscopy z-stacks of a channel containing fluorescein solution under a flow rate of 1800 μl/h showing ceiling deformation at a position 460 mm from the outlet (4.14a) and 110 mm for the outlet (4.14b) The deformation of the side of the channel is measured as 2.6 μm at 460 mm from the outlet whereas the height change is 11 μm. Scale bar = 50 μm

4.5 Nanoindentation of PDMS with an Atomic Force Microscope to measure Young's Modulus

In previous studies, the Young's modulus of PDMS was estimated using numerical simulation in order to calculate theoretical values of internal channel pressure and channel deformation[170,172]. In this work the Young's modulus was measured directy using nanoindentation. To determine the Young's modulus of PDMS, samples of fresh PDMS and oil soaked PDMS were measured using an Atomic Force Microscope (AFM, Bruker FastScan). The tip used was an SNL-10-D which was first tuned to obtain a spring constant and gave a value of 0.0705 N/m. The sensitivity of the tip was calibrated with a hard silicon sample to 316 nm/V. The sample thickness was 100 μm to avoid coupling between the sample and the glass it was bonded to as the indentation depth was 1 μm. Recommendation is that the indentation depth is no more than 10 % of the film thickness[201]. Indentation was performed in 20 independent locations, at least 100 μm from the previous indentation over the surface of the polymer. The oil soaked PDMS was fully saturated with oil over a period of 6 hours before measurement.

Figure 4.15 shows force displacement curves for the two different samples. In order to extract the Young's modulus of the PDMS, fitting was done using

Bruker NanoScope analysis software. The Sneddon model (described in section 2.12) was fit for a conical indenter and the Young's modulus found. For the pure PDMS sample, the modulus was found to be (2.80 ± 0.03) MPa and for the oil soaked (1.32 ± 0.04) MPa, a reduction of 53 %. This shows the infiltration of mineral oil into the polymer matrix of PDMS effects the local material properties dramatically.

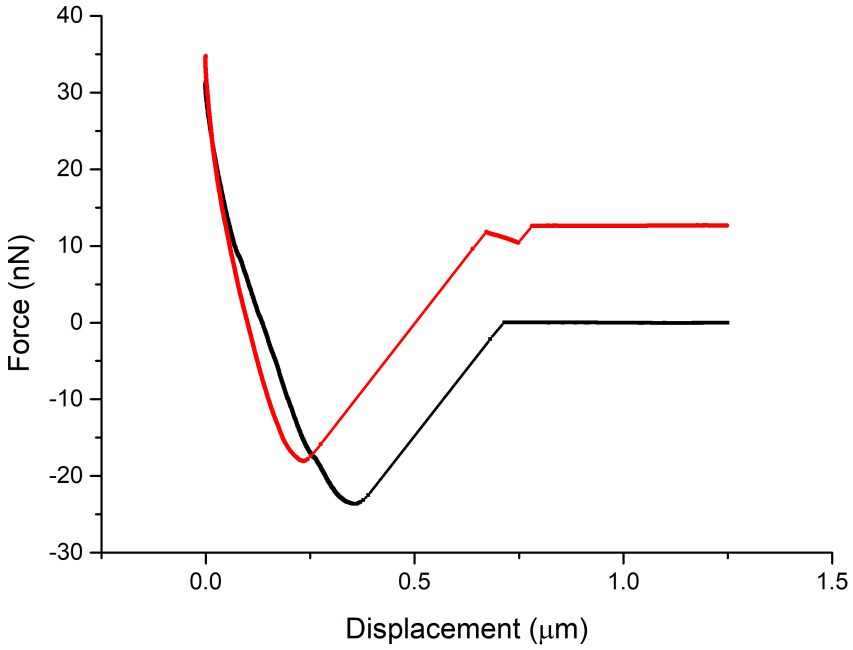

Figure 4.15: Force displacement curves for fresh PDMS (red) and oil soaked PDMS(black) from AFM nanoindentation. Each indentation generated a force displacement curve from which Young's modulus can be calculated. (curves offset for clarity)

Using this data, the theoretical calculations of the internal channel pressure and channel deformation could be calculated using equation 4.1 leading to plots 4.5, 4.12, 4.20 and 4.20

4.6 Raman Spectroscopy of Mineral Oil Absorption of PDMS

The observations with Nile red and mineral oil showed the diffusion of Nile red into the PDMS walls of the channel. This gave a good visual indication of absorption but could not be used to infer the diffusion of mineral oil. It cannot be assumed that the carrier oil diffuses at the same rate as the dye therefore another method to measure the oil permeation is required. Raman spectroscopy was used to measure the ingress of mineral oil into the PDMS channel walls without the presence of fluorophores. Fresh devices were prepared along with a sample of pure mineral oil. Raman specta were taken of pure PDMS and the mineral oil to establish characteristic peaks that will be used to track mineral oil. Measurements were taken with a 532 nm laser for all experiments. Figure 4.16 shows the spectra obtained for pure PDMS (blue) and pure mineral oil (red), from these spectra it can be seen that the mineral oil has a prominent peaks at 1443 cm^{-1} due to CH2 and CH3 groups and 2848 cm^{-1}, from C-CH3 and CH2 groups, which was used as the reference peak throughout these experiments. In order to normalise against the PDMS that the oil is diffusing in to, the peak at 709 cm^{-1} was used.

To investigate the oil infiltration, a scan line was set up which started within the channel and took spectra at intervals of 20 μm along a line perpendicular

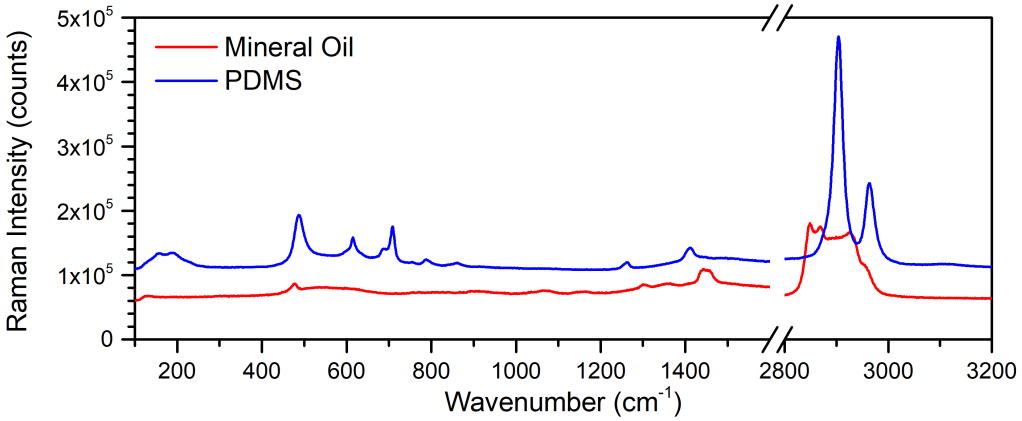

Figure 4.16: Raman Spectra of PDMS and Mineral oil identified characteristic peaks.

to the channel into PDMS (see figure 4.17, right hand side). At each point a spectra was taken with the laser at 100 % intensity (22 mW) for 1 second in high confocality mode (22 μm slit opening) through a 40 x objective. Spectra were acquired between 100 - 3200 cm^{-1} with 6 spectra within the channel and 48 outside the channel to a distance of 960 μm away from the channel wall. The laser was focussed on the glass coverslip below the channel then moved 10 microns in z to be positioned in the middle of the channel. A scan was taken with no oil present and then the mineral oil flow was started. At a flow rate of 40 μl/h, spectra were acquired along the line every 5 minutes. Figure 4.17 shows the contribution of mineral oil as a function of distance from the channel wall after a time of 75 minutes. The mineral oil peak intensity decreases further away from the channel wall but is still present within the PDMS. Figure 4.18 shows the spectra at time points 0, 40 and 75 minutes from when the oil flow started. The prominent peak in the centre of each plot is due to PDMS and

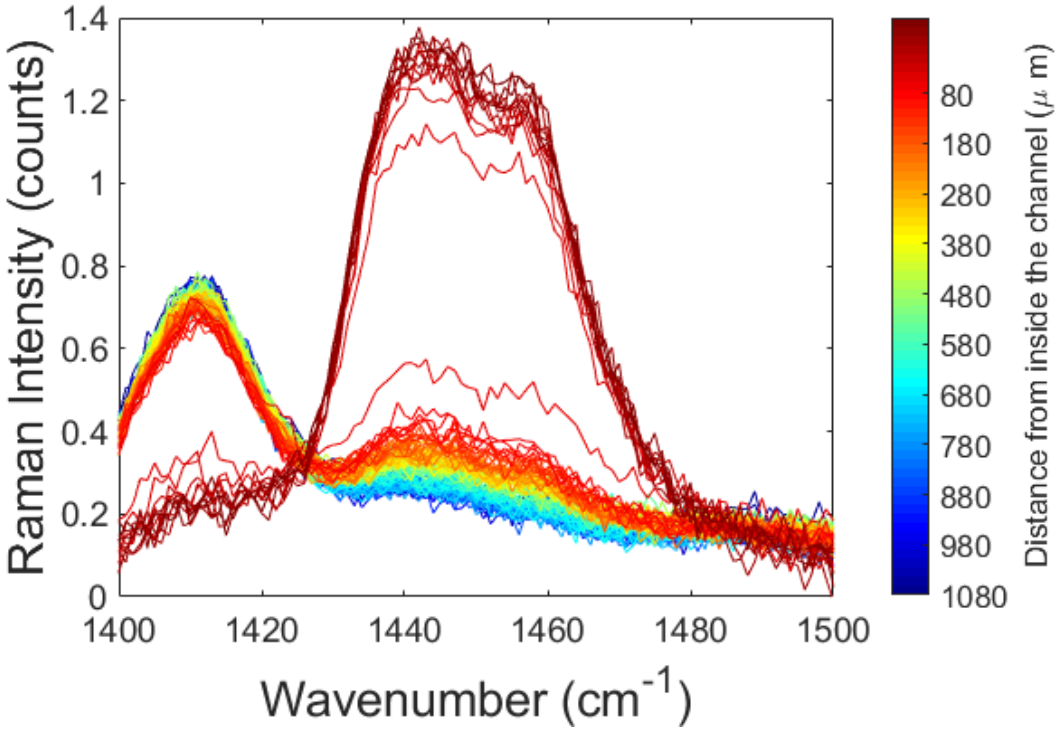

Figure 4.17: Raw Raman spectra shows the contribution of mineral oil as a function of distance from the channel wall. The Raman intensity can be seen to drop off as the scan progresses into the bulk PDMS. Time = 75 minutes therefore the bulk PDMS is saturated with oil.

the peak to the left is due to mineral oil contributions.

The normalised intensity of the PDMS was plotted against time and position in figure 4.19 and show the evolution of the increasing intensity further away from the channel edge over time. The plot indicates the the mineral oil is diffusing into the PDMS to a great enough degree that on the scale of the deformations that are being observed, the PDMS Young's modulus can be considered to be that which was measured by AFM nanoindentation. Independent of Nile red infiltration, this result shows the diffusion of mineral oil into PDMS over a time scale of tens of minutes is enough to dramatically change the Young's

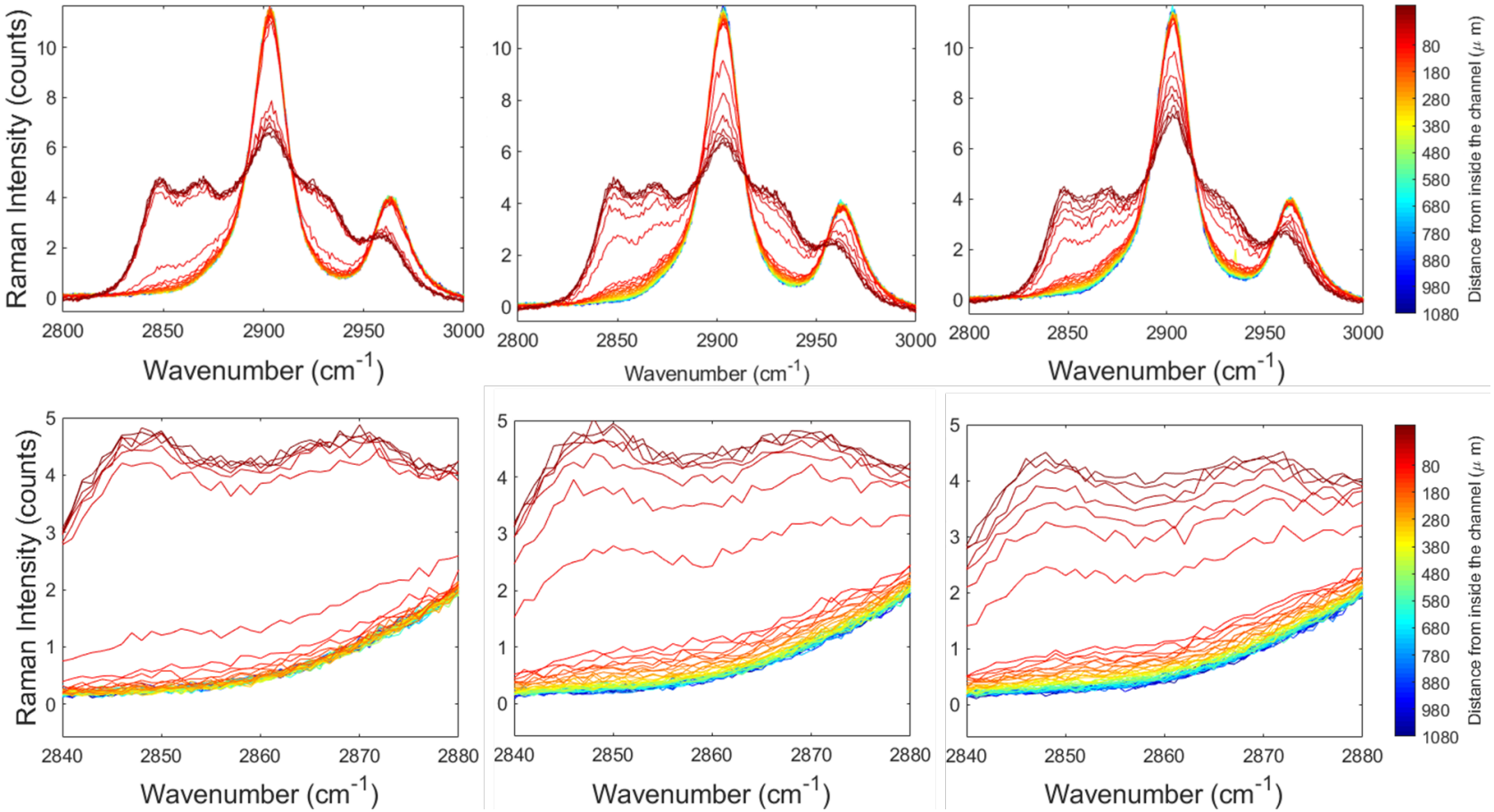

Figure 4.18: As a function of time, the intensity of the 2848 cm^{-1} can be seen to increase indicating mineral oil infiltration into the PDMS.Left column = 0 minutes after the oil flow was started, centre = 40 minutes after flow was started and right = 75 minutes.

modulus. Figure 4.19 shows that even after 20 minutes, the mineral oil has infiltrated the polymer matrix further than 50 μm allowing for the observed channel deformations.

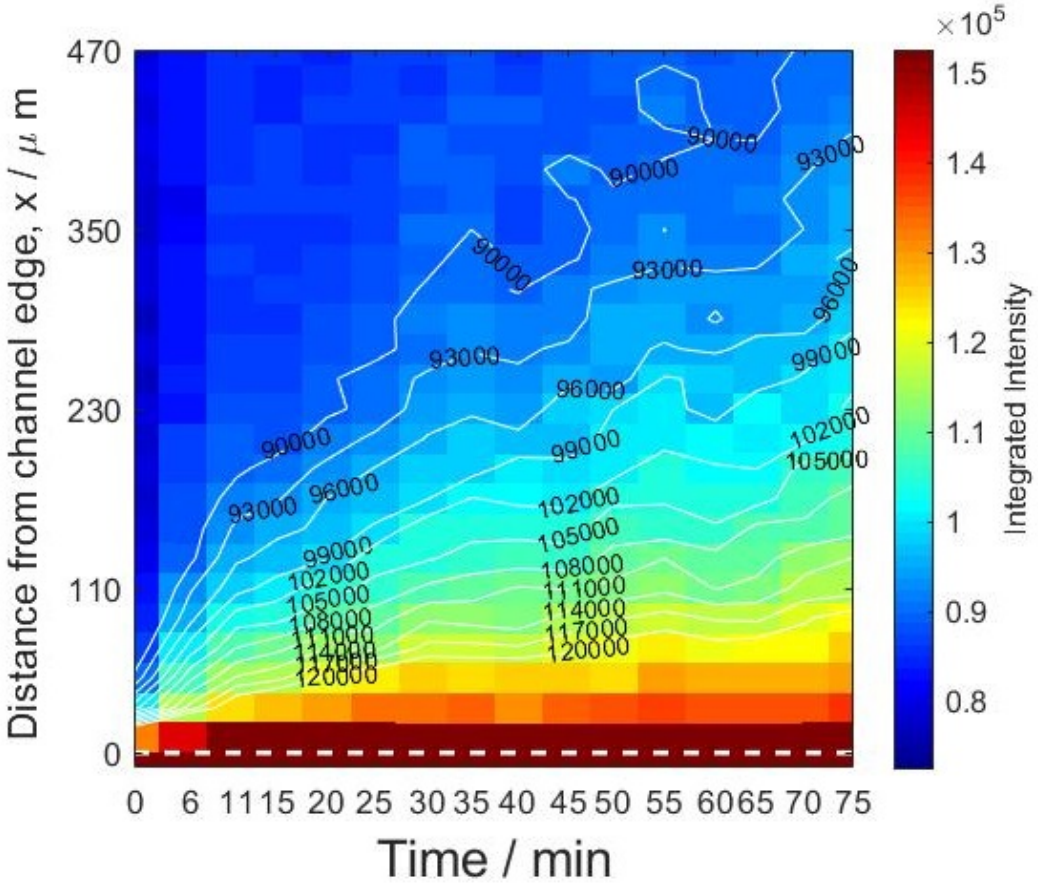

Figure 4.19: Normalised intensities of the 2848 cm^{-1} mineral oil peak against distance and time show the diffusion of oil into the PDMS polymer matrix. Contour lines show lines of equal normalised intensities.

4.7 Pressure Measurements with Mineral Oil

After investigating the interaction of PDMS with mineral oil, the pressure measurements were repeated. During the first measurement of pressure with min-

eral oil as the flowing fluid (described in section 4.2) there was constant diffusion of oil into the PDMS while the experiment was taking place. This infiltration was constantly changing the Young's modulus of the PDMS leading to inaccurate results. Here, the mineral oil was flowed through the channel at a flow rate of 40 μl/h for 3 hours before being flushed with water and then internal channel pressure measured. The change in Young's modulus measured with nanoindentation was applied to the theoretical model and a new set of theoretical values calculated. When plotted with measured results as shown in figure 4.20 it can be seen that the change in Young's modulus provides a good match to explain the change in deformation measured.

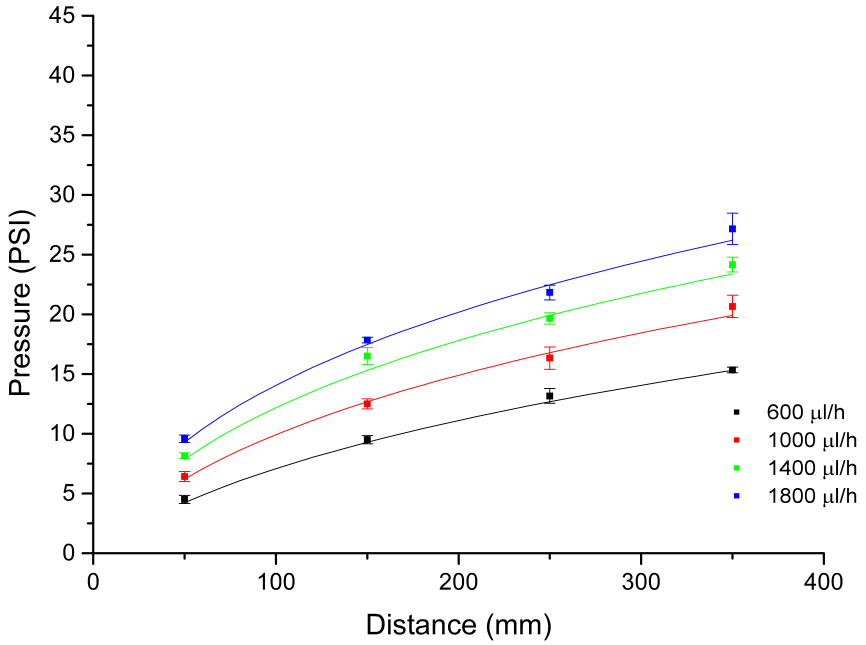

Figure 4.20: The pressure of microchannels after mineral oil flow show lower pressures than in the fresh PDMS case. The reduced Young's modulus allowed for greater deformation, therefore larger channel surface area and lower pressures.

4.8 Conclusions

In this chapter the internal pressure of microfluidic channels was investigated. A novel way to measure on chip microchannel pressure was devised using a pressurised air supply along with pressure regulators to equilibrate the channel pressure and read off a full channel pressure profile. Measured pressure for regular PDMS channels agreed with previously published theory [170,172] for deformable channels. This showed that the theories provided were valid for channels that were longer than previously reported, even using a sepentine design. The introduction of a solvent that diffuses into PDMS introduced a challenge as the internal pressures and deformations no longer agreed with theory. Bulk swelling experiments allowed the determination of the diffusion coefficient of mineral oil into PDMS and subsequent Raman spectroscopy measurements visualised the infiltration of oil into the polymer matrix. Changes in material properties were measured through AFM nanoindentation and revealed a 53 % reduction on Young's modulus after mineral oil infiltration. This new Young's modulus was used to calculate new theoretical internal pressures and deformations which matched experimental results. The deformation of channels was seen with confocal microscopy for both pure PDMS and PDMS after oil infiltration. PDMS remains a popular choice for microfluidic devices, especially in cell culture experiments as its gas permeability is key in maintaining a suitable atmosphere for cellular culture. However, the diffusion of molecules into

PDMS can cause issues as signalling molecules or even drugs can appear to vanish from studies[43]. The deformation of PDMS microchannels is important in blood vessel simulations in which the geometry of the vessel can change due to increased blood pressure. The ability to design devices which mimic these flow deformation conditions may be beneficial for furthering understanding of complex flow environments.

Chapter 5

Chip Development for Expansion Microscopy Imaging of Cardiomyocytes

The aim of this chapter is to present the motivations and iterations of a microfluidic device to perform expansion microscopy. The target biological sample was mouse cardiomyocytes that had been induced with heart failure. The aim of the expansion is to image ryanodine receptors responsible for muscle contractions as a result of this heart failure[187]. The four iterations of the device will be presented as well as images from attempts to polymerise acrylamide gel within channels containing cardiomyocytes. The general operating principle of an experiment is that cardiomyocytes are suspended in the acrylamide

monomer solution, which is then mixed with the initiator and accelerator before injection into the channel[179–181]. Different concentrations of initiator and accelerator were used and will be explained at relevant points. In this chapter, all preparation of biological samples (cardiomyocyte cells), gel components and gel compositions were performed by Tom Sheard of Biological Sciences.

The composition of the monomer solution is shown in table 5.1

Component	Stock Conc.	Amount (ml)	Final Conc.*
Sodium acrylate	38	2.25	8.6
Acrylamide	50	0.5	2.5
N,N-Methylenebisacrylamide	2	0.75	0.15
Sodium chloride	29.2	4	11.7
PBS	10X	1	1X
Water		0.9	
Total		9.4**	

Table 5.1: Monomer Composition - *all concentrations in g/100 ml except PBS - **9.4/10 ml, the remaining 0.6 ml is made up by the initiator and accelerator.

Gelling solution was made in 200 μl batches comprised of the following.

Component	Volume (μl)
Monomer Solution	188
Inhibitor Solution (4-hydroxy-TEMPO)	4
Accelerator Solution (TEMED)	4
Initiator Solution (APS)	4

Table 5.2: Standard recipe for the preparation of 200 μl of gelling solution.

Component	Amount
Tris buffer pH 8.0	50 mM
EDTA	1 mM
Triton X-100	0.5 %
Guanidine HCL	0.8 M
Proteinase K	8 units/ml

Table 5.3: Standard recipe for the preparation of digestion buffer

5.1 Initial Device Design, A Sliding Gel Block

The first proposed device design is shown in figure 5.2. The device comprises of a flow layer, shown as green and blue and the yellow control layer. Green layer is 40 μm high and the blue layer is an additional 40 μm on top of the green, 80 μm total. The yellow control valves are 25 μm in height and are on top of the flow layer. Usually in multilayer device fabrication, the valve layers are on the bottom of the device in contact with the glass. However, when these devices are to be used in a high resolution confocal microscope, the available required objectives have working distances of 200 μm. If the devices layers were arranged in the conventional orientation, the thickness of coverslip (130-170 μm) plus the valve height and membrane (25 and 15 μm) would limit the imaging ability. The reversal of the layers allows for 30 - 70 μm of imageable channel in the device. The gelation would occur between valves A and B then a force applied from flow at inlet 2 would cause the solid gel to slide into the expansion area at the left of the device.

Cardiomyocytes are cylindrical in shape with length 100 μm and diameter 10 - 25 μm[187]. A cardiomyocyte that has had staining applied to its actinin microfilament proteins is shown in figure 5.1. The image was taken on a slide after ProLong Gold Antifade Mountant (ThermoFisher) had been applied. ProLong Gold is a liquid mountant applied directly to fluorescently labelled cells or tissues on microscope slides. It protects dyes from fading during fluores-

cence imaging. This image represents the optimal image to obtain within the microfluidic device.

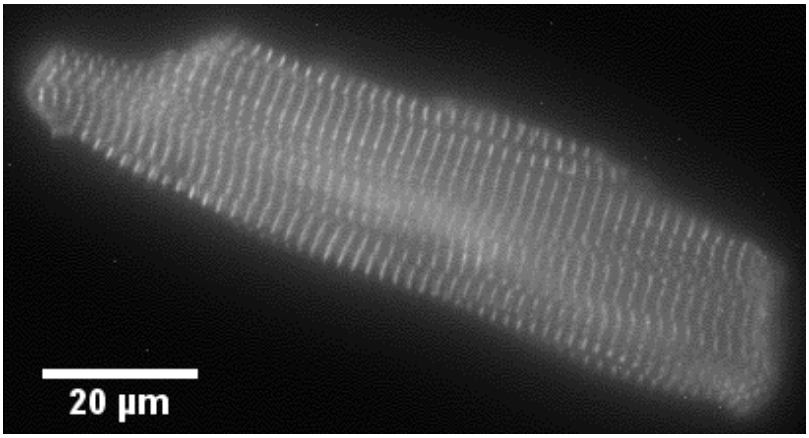

Figure 5.1: A cardiomyocyte imaged on a slide after actinin staining. A layer of ProLong Gold antifade solution has been applied to protect fluorophores from bleaching. Image provided by Tom Sheard.

The principle of operation is that the device is first filled with PBS buffer to remove all air bubbles present. The valves are activated with water in the tubing to push out the air inside the fingers until they are full of water. The gel solution is prepared off chip and immediately injected into the device through inlet 2. During the injection, valve A is activated and inlet 1 is blocked. The gel solution flows between inlet 2 and outlet 3 until sufficient cells have entered the area between the two valves. The thin channels of 1 and 3 are 30 μm to prevent the cells escaping the intended area. At this point the injection is stopped and valve B is activated. Buffer is flowed through inlet 1 to flush the right hand side of the device of gel solution before the device is left to allow polymerisation to occur. After polymerisation there should be a gel slab present within the channel. Valves A and B would be released and the slab pushed through to

the expansion area by injecting a PBS buffer flow in inlet 2. Once the slab had moved, valve A would be activated to isolate the expansion area. Digestion buffer flows between inlets 4 and 5 overnight at room temperature to digest the cell structure. Finally, PBS buffer replaces the digestion buffer and the gel expands.

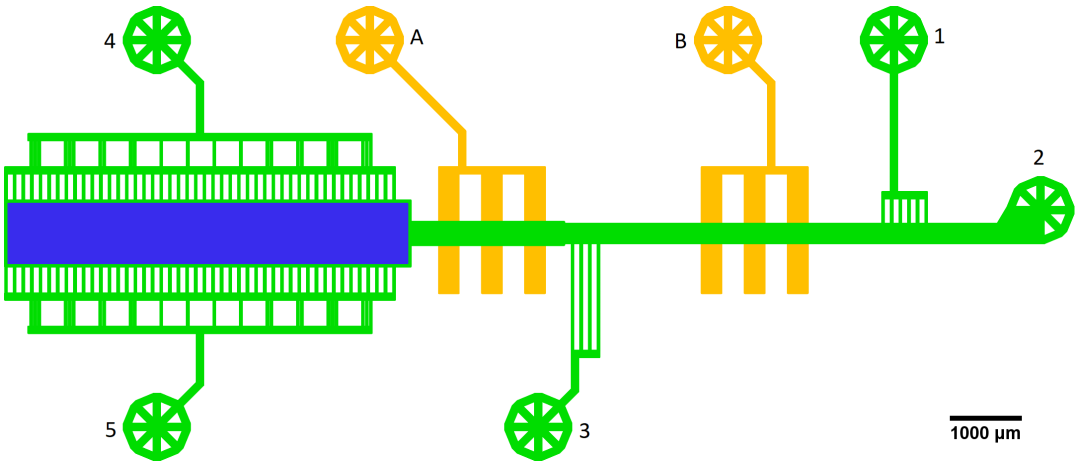

Figure 5.2: This two layered device is designed to trap cardiomyocytes in acrylamide gel solution between valves at A and B. After gelation, the gel slab is moved to the expansion chamber (blue) for digestion and expansion. The blue and green layers are 40 μm each (total 80 μm in the expansion area) and the yellow valves are 25 μm thick.

Initial experimentation involved the injection of cells to verify the devices trapping ability. The first cell injections showed that the side channels at 50 μm were too large to stop cells escaping. This is shown in figure 5.3 where the cells have begun to infiltrate the side channels. Figure 5.3a shows the cells after full injection of the solution, the gelation area has concentrated the cells. This will make the cells more difficult to resolve later in the imaging process so the concentration was lowered by ten times for injection in figure 5.3b. Note, the channels either side of the main channel were present on some designs on the

same wafer as design 1, they were removed after this iteration.

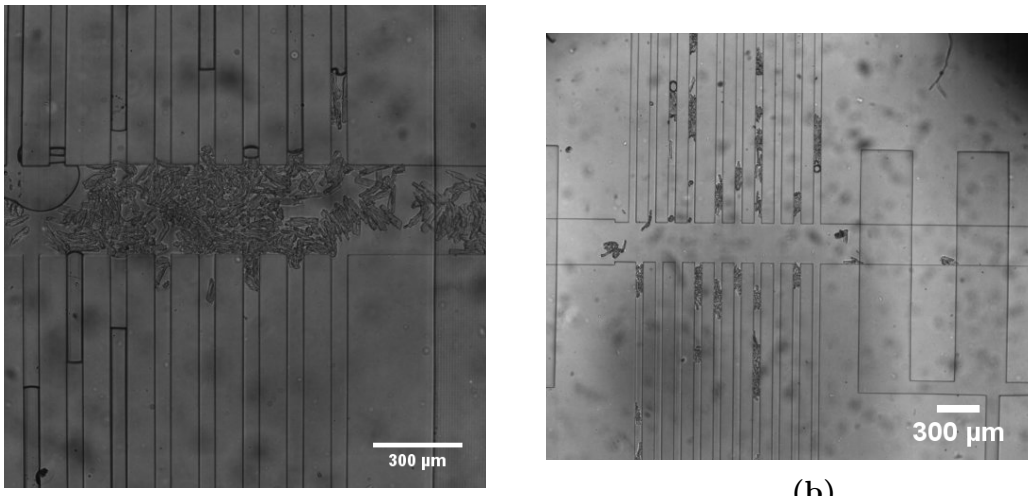

(a) **(b)**

Figure 5.3: (a) The accumulation of cells in the gelation area is too high and the cells are beginning to infiltrate the outer channels. (b) A lower concentration of cells is advantageous but again they show egress from the main channel.

Figure 5.4 shows a small cluster of cells after injection of gel solution. After leaving the gel to solidify for four hours the pressure was released. It was immediately apparent that the gelation had not been successful as the solution remains liquid when the valve was released. In the experiments described up to this point, the concentration of initiator (APS) and accelerator (TEMED) were 0.1 %. Repeating the process and leaving the gel to cure overnight had no impact and the solution remained liquid.

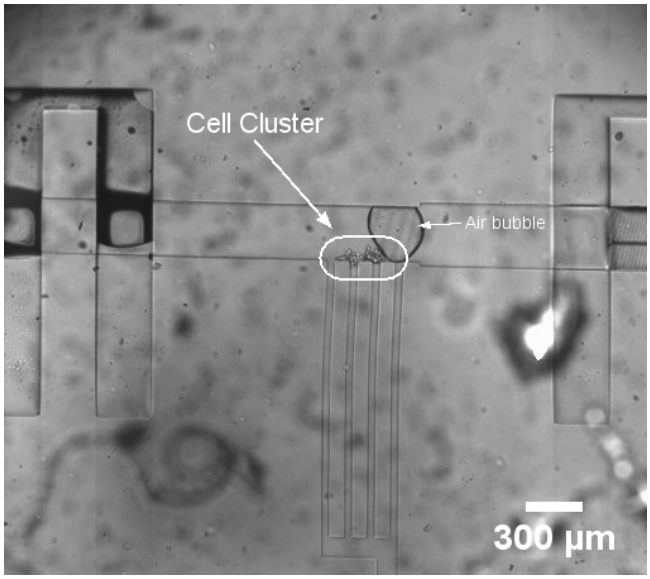

Figure 5.4: A small cluster of cells inside the gelation chamber after injection. The cells remained in this position and the gel solution remained liquid.

5.2 Device Revision 2 - A smaller gelation area

The second revision of the device is shown in figure 5.5. In this design the size of the gelation chamber was reduced to 750 μm in length to allow for the formation of a smaller gel slab. This was to make transportation of the gel into the expansion chamber easier. Another feature to aid this transition was to extend the 80 μm layer of the device to the edge of the gelation chamber where the step in height could aid the release of the slab. Inlet 1 has also been moved into the same area as valve B. This was to attempt to reduce the possibility of gel clogging up the channels when polymerising. If excess gel was present in device 1, it was possible that the slab was immovable.

Cells were injected into the device with a higher APS/TEMED concentra-

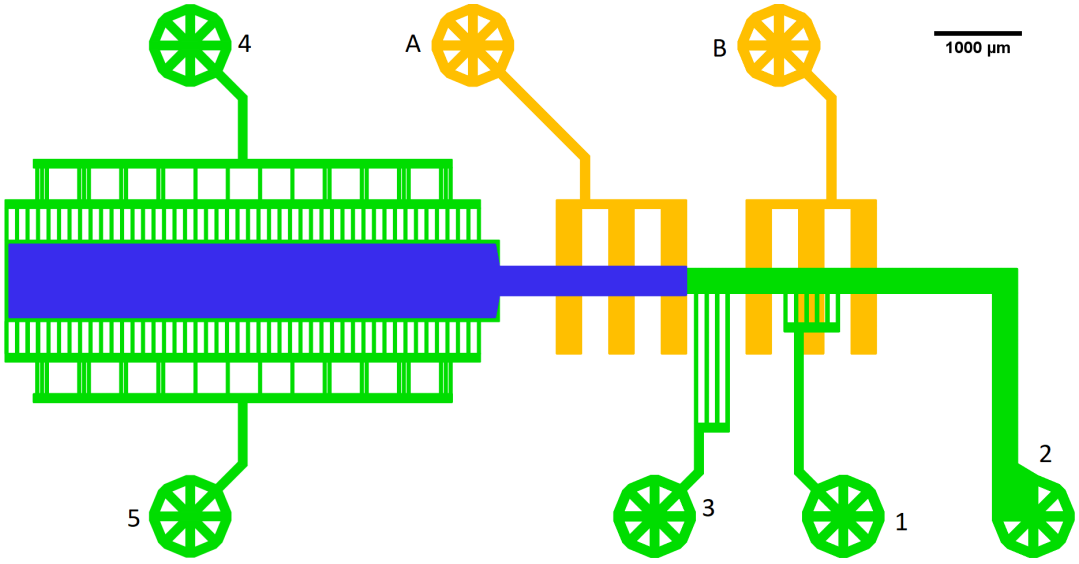

Figure 5.5: Device iteration 2 improved some of the failures of device 1. The 50 μm side channels were reduced to 30 μm and the step in height up to 80 μm was moved up to the gelation chamber edge.

tion of 0.2 % and the inhibitor 4-hydroxy-TEMPO removed. At 0.1 %, outside of the chip, the gel became solid after 12 minutes. At 0.2 % the solution became solid in approximately 30 s indicating that there is likely transport of some of the initiator and/or accelerator into the PDMS walls of the device. Figure 5.6 show cells that have been loaded into the device with a 0.2 % APS/TEMED concentration. After an overnight incubation the gel solution was still liquid and at this point no gel had been observed on chip. It could be suggested that the gel solution itself was not functioning correctly but observations of the syringe and tubing interfacing with the device disagree. Any gel remaining in the syringe became solid in the same time frame as described earlier, indicating that the PDMS was interfering with gelation.

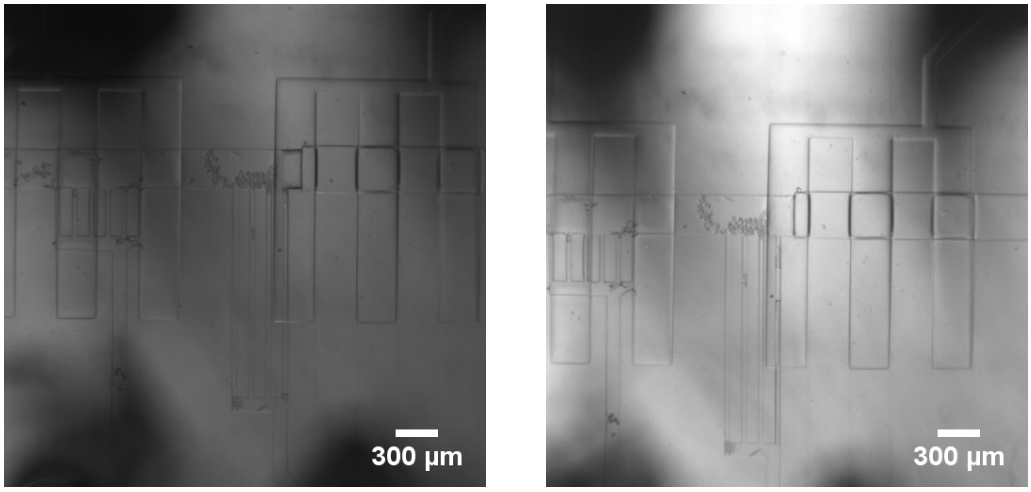

(a) **(b)**

Figure 5.6: (a) Cells were trapped in the 750 μm length gelation area. (b) After an overnight incubation to gelate, the solution was still liquid.

5.3 Device Revision 3 - Pocket based cell capture

Changes to the device were quite radical at this point. The idea of a gel slab was discarded in favour of individual pockets where gel could form. Shown in figure 5.7, the device consists of an area to diffuse cells along the width of the device when injected into inlet 1 to enable even distribution into the traps. The traps consist of walls that are 100 μm wide in a U shape. At the bottom of each trap there is a 35 μm gap to allow the laminar flow to draw cells into the traps. The yellow section shown in figure 5.7b is a large scale valve that covers the entire trap area. When casting the PDMS onto this relief pattern the resulting chamber will include the curved traps on the ceiling of the device. As can be seen in figure 5.7a, the trap moulds do not extend to the base of the device but

down to the first 40 μm layer. This feature means that gel can be polymerised in the traps while pressure is applied to the whole ceiling, pushing the traps down onto the device base. After curing, the pressure is released and should leave behind 40 μm high gel droplets. After injection of liquid gel solution and application of pressure, buffer can be flowed into inlet 3 or 4 in an attempt to flush gel away from the traps to isolate them from each other. However, due to the similarity in viscosity and miscibility, this was not possible.

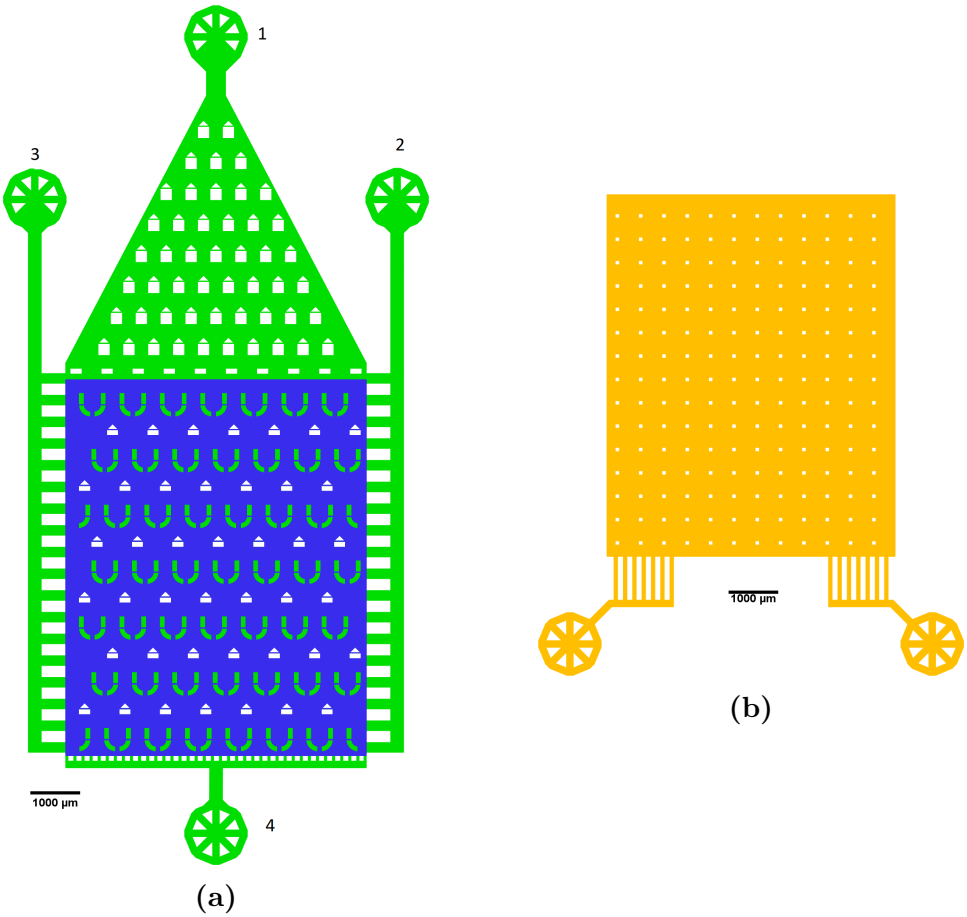

Figure 5.7: The third device design incorporated pressure actuated traps in an attempt to form discrete compartments of gel. The yellow valve layer is positioned on top of the blue 80 μm layer.

As the gel was not polymerising on chip, an APS/TEMED solution was used as the working fluid in the valve above the traps. This was done to provide a reservoir of molecules for the polymerisation process. Channels were also soaked in APS/TEMED solutions overnight to saturate the PDMS with the initiator and accelerator.

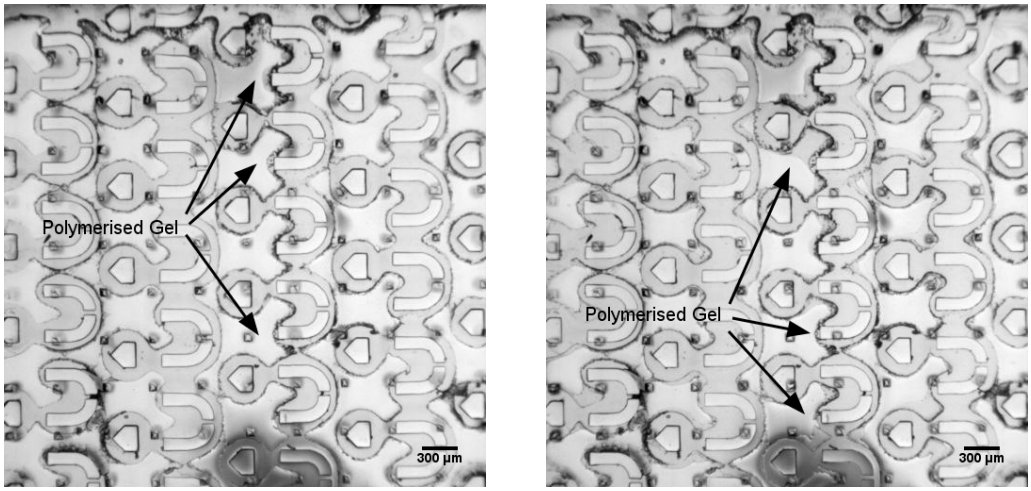

(a) **(b)**

Figure 5.8: (a) Successful crosslinking of acrylamide gel after 60 hours. The trap pressure is still applied. (b) After the release of pressure, the gel stays intact.

Cells were injected with concentration of 0.2 % and 0.3 % APS/TEMED solutions to maximise the chance of crosslinking. The 0.2 % behaved as before and no gelation occurred after 60 hours. However, the 0.3 % solution successfully crosslinked after 60 hours and can be seen in figure 5.8. The gel appears to have formed in a way in which it has no contact with the PDMS of the traps. This could be due to the gel drying up after such a long period of incubation (The edges of the gel look like they could be dry, a high magnification is shown in figure 5.9) or by some surface tension effects that arise when the gel is form-

ing. As the gel formation appears to be slow as at a time of 48 hours after injection the chamber was observed to be full of liquid.

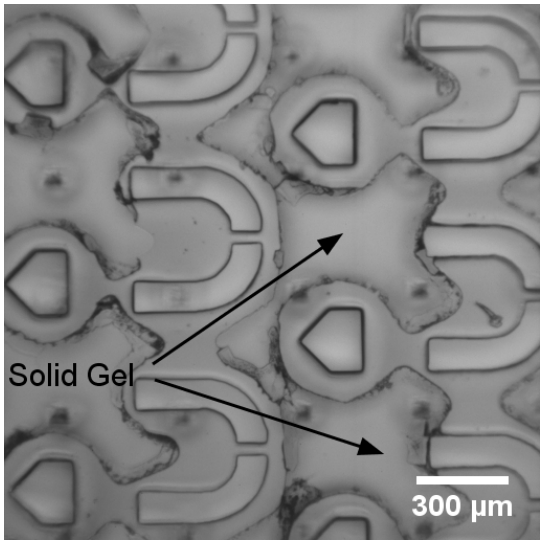

Figure 5.9: The gel has formed away from the pockets either through some drying or surface tension effects.

5.4 Device Revision 4 - Larger Trap Chambers

The next revision is shown in figure 5.10 and is similar in principle to version 3. The chambers have been made larger, 500 μm across and 800 μm long. The motivation for this design change was derived from the behaviour of the gel in the previous version. If it was possible to make the gel form away from the PDMS surface then this shape of trap would encourage the formation of individual discrete gel compartments. The cell inlet (number 1) was increased in height to 80 μm as the cells were bottlenecked at this area in the previous design. This change was to encourage a good distribution of cells across the

trapping layer. As before, the trap was actuated with APS/TEMED solution and the channels were soaked before use.

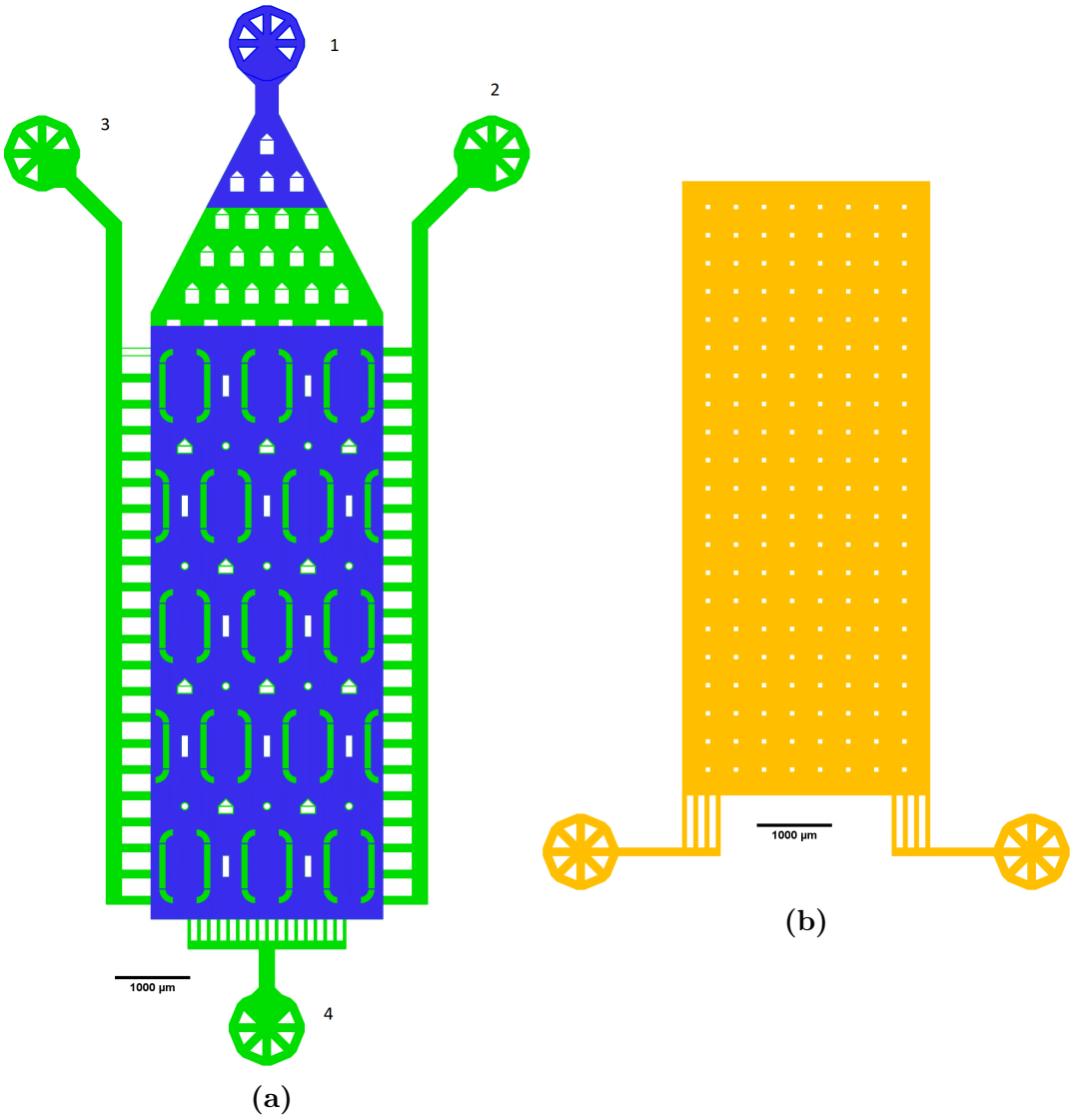

Figure 5.10: Design 4 refines the traps in order to encourage gel to form as it did in device 3. The traps are 500 μm x 800 μm x 40 μm. The valve layer is positioned on top of the traps as previously described.

Gelation occurred in this device on a handful of occasions. Interestingly the best gelation was seen at and APS/TEMED concentration of 0.2 % which failed

on previous devices. The 0.3 % APS/TEMED solutions did not gelate at all on this device. Figure 5.11 shows gelation in two of the devices. The expectation was that the gel would form into discrete compartments inside the traps but this does not appear to be the case. These gels were observed after 72 hours and appeared to still be liquid at 48 hours. There is a thin gel piece extending from the entrance/exits of the traps which could indicate that a narrowing of the opening could in fact form discrete areas of gel.

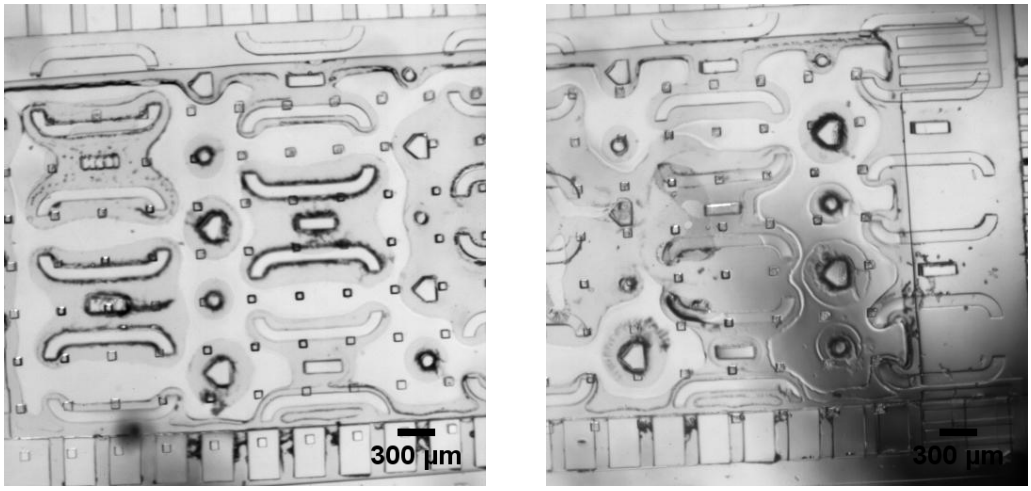

(a) **(b)**

Figure 5.11: Gelation with a 0.2% APS/TEMED solution was achieved. The gel solution did not form discrete compartments as expected.

Cells were imaged within the polymerised gel solution to ensure the fluorescence tags had not been damaged after long polymerisation times. Shown in figure 5.12, two cells demonstrated that the fluorescence had not been lost and the cells structure had remained intact. Under stress the cells can lose their rigid structure and collapse into a spherical state.

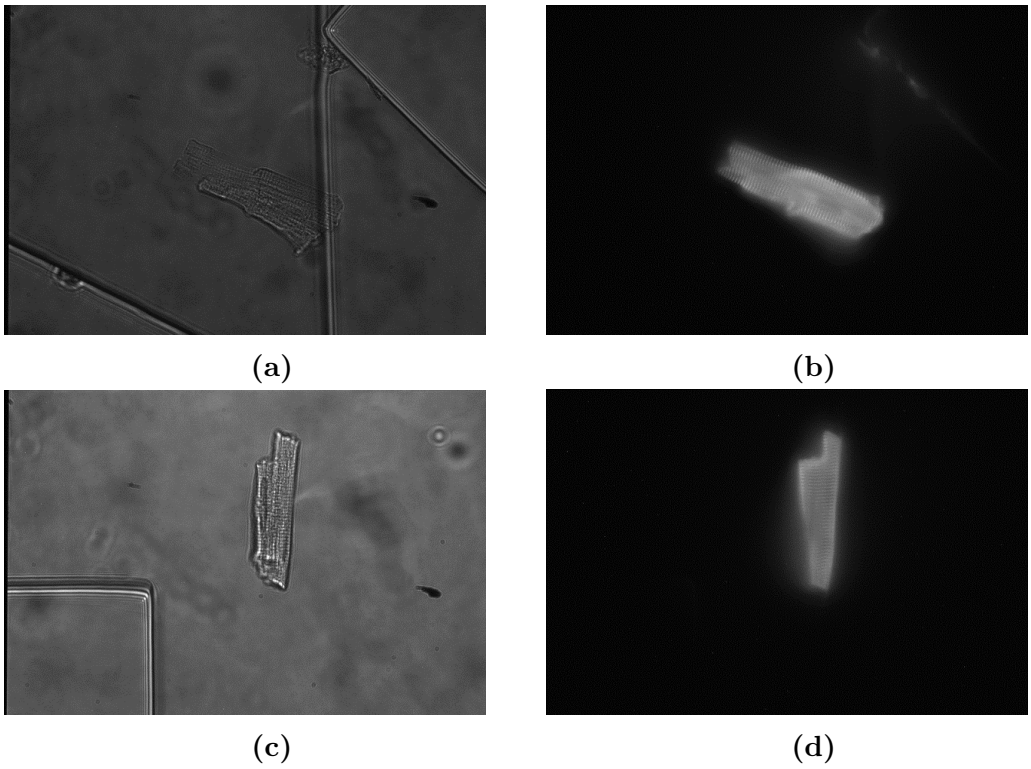

Figure 5.12: (a) and (c) show cardiomyocyte cells in place within an acrylamide gel structure. The fluorescence of the cells (b) and (d) was not lost during the acrylamide polymerisation time of 72 hours.

5.5 Conclusions

The aim of this project was to develop a microfluidic device to encapsulate cardiomyocytes within an acrylamide gel to perform expansion microscopy. Through iterations of the device design, gelation on chip has been successful. Initially gelation appeared to be inhibited by PDMS, possibly through loss of initiator and accelerator and this was resolved by the addition of an APS/TEMED reservoir in valves above the gelation. After successful gelation the device was optimised to try and force discrete compartments of gel to enable multiple expansion measurements. However, the current version does not cause this to occur. Cells were shown to be successfully embedded within the gel without degradation of fluorescence due to long cure times at room temperature. The future of this device will either take the form of refinement of the traps to encourage compartmentalisation or a droplet based approach where single cells can be encapsulated in droplets and then incubated on chip to polymerise. This may offer an advantage whereby the contents of the droplet will be contained and not diffuse out into the PDMS.

Chapter 6

Discussion

6.1 Microfluidic Immunoassay

The aim of chapter 3 was to expand the detectable concentration of prostate specific antigen (PSA) with microfluidic immunoassay. Characterisation of microfluidic droplet generation through flow focusing nozzles was performed and showed good performance of 6 - 10 μm wide nozzles for generation of droplets stably to 4 μm. The detection of single molecules of β-galactosidase was initially elusive as no detectable fluorescent product was seen during experimentation. Kinetic studies of the enzyme confirmed it was functioning as expected and subsequent investigation led to a change in optical microscopes. With new optics the fluorescence was detectable and the concentration of β-galactosidase was

measured down to a value of 47 fM. This paved the way for immunoassay and PSA detection. Characterisation of the immunocomplex conjugation confirmed the binding of primary antibodies to polystyrene beads even though previously reported fluorescence properties were unable to be replicated in single droplets but were apparent in high bead concentrations. Due to this lack of fluorescence the beads were difficult to distinguish in the droplet traps and therefore PSA detection was inaccurate. The full immunocomplex conjugation was shown to be functional as fluorescence was detected in droplets when formed with bead immunocomplexes and enzyme substrate FDG. The substitution of the beads for a bar-coded or alternatively tagged fluorescent bead could lead to improvement of PSA detection and pave the way for multiplexed detection of various biomarkers. As it stands, the multiplexed detection of biomarkers is generally reserved for research[211], developers of immunoassay believe that the technology can lead to portable, in-home devices that could monitor a range of general health biomarkers without requiring medical trained personnel[88].

Further aims of this chapter that were not realised were a redesign of the current microfluidic device in order to take advantage of wasted droplets generated within the device and utilise them for measurement. In the current configuration, the device is capable of holding 200,000 droplets at one time, a theoretical limit of detection of 4.7 fM. The current capture efficiency of beads within the device is 10 % which would need to be greatly improved to lower the

LOD even further. The investigation of rapid detection of droplet fluorescence may be useful to try and utilise wasted droplets although the practicalities of implementing such detection would greatly increase the complexity of the system.

6.2 On-chip Pressure Measurements

The experimental aim in Chapter 4 was to develop a novel method of measuring the pressure inside a PDMS microchannel. This was achieved with a pressurised air supply and regulators to counteract the pressure inside the channel and measure it. This alternative to pressure transducers was shown to match well to published theories on the internal pressure of a compliant polymer microchannel which is advantageous for more complex microfluidic chip designs as we ll as the simple straight channels presented in previous work. The introduction of mineral oil into a PDMS channel caused the measured pressures to deviate from the theory. Due to the mineral oil being absorbed by the PDMS, the local mechanical properties of the channel walls changed. To investigate, the bulk swelling of PDMS was observed and a 3.5 % increase in surface area was shown when immersed in oil. Raman spectroscopy was used to demonstrate the infiltration of mineral oil through tracking of a strong Raman peak intensity into the PDMS over time. This showed infiltration on the order of 100 μm

within 60 minutes. The mechanical properties of mineral oil soaked PDMS were investigated using AFM nanoindentation showing a 53 % decrease in Young's modulus when compared to fresh PDMS. This reduced Young's modulus was applied to the deformation theory and along with confocal imaging of channels under pressure provided a good match for measurements with oil soaked PDMS. The measurements of pressure induced deformation demonstrated before these experiments were performed estimate the value of Young's modulus based on observations made. The coupling of measured modulus and pre-existing theory reinforces

Potential further experiments could include the characterisation of other molecules diffusing into PDMS such as cellular signalling molecules or drugs as these have been found to disappear from PDMS microfluidic channels. The changing of PDMS material properties has been shown to be of use in the detection of solvent vapour when expansions cause a circuit to close activating an RFID loop[212]. The understanding of pressure within microchannels is leading to understanding of other processes such as droplet generation and the coupling of material absorption and pressure measurement could have advantages in this avenue of investigation.

6.3 Expansion Microscopy

An on chip acrylamide expansion microscopy system was developed in chapter 5 as currently no such solution exists. The devices developed from a system where gel could be formed and then moved into another part of the device to an array of traps with the possibility of confining individual compartments of gel for expansion in situ. Initial runs with standard concentrations of polymerisation initiator and accelerator yielded no solid gel inside a microfluidic device even though all gel contained within the interfacing tubing and delivery syringe was solid. The leading theory states that PDMS is absorbing one or both of these molecules and inhibiting the polymerisation. In further iterations of the device, the use of a device wide valve enabled the introduction of a reservoir of initiator and crosslinker above the gelation channel. This change enabled the formation of gel under high initial concentrations of initiator and accelerator coupled with the above channel reservoir. At this point the formation of discrete gel compartments has not been achieved but the latest device design shows great promise. For further iterations, the use of droplet microfluidics might enable easy formation of gel spheres to trap cardiomyocytes and expand them once cell digestion has occurred. This could lead to a system where many different cell types could be imaged using expansion microscopy. Currently in the field of expansion microscopy, the protocol remains relatively unchanged. The development of a microfluidic based system could greatly enhance the ac-

cessibility of expansion microscopy through the production of a generic system. Very little literature exists regarding the coupling of expansion microscopy and microfluidics and the progress in this chapter may lead to a robust and easy to use set up.

Bibliography

[1] Luoran Shang, Yao Cheng, and Yuanjin Zhao. Emerging Droplet Microfluidics. *Chemical Reviews*, 117(12):7964–8040, jun 2017. ISSN 0009-2665. doi: 10.1021/acs.chemrev.6b00848. URL `http://pubs.acs.org/doi/abs/10.1021/acs.chemrev.6b00848`.

[2] Adam Sciambi and Adam R. Abate. Accurate microfluidic sorting of droplets at 30 kHz. *Lab on a Chip*, 15(1):47–51, oct 2015. ISSN 14730189. doi: 10.1039/c4lc01194e. URL `http://xlink.rsc.org/?DOI=C4LC01194E`.

[3] Jung Uk Shim, Rohan T. Ranasinghe, Clive a. Smith, Shehu M. Ibrahim, Florian Hollfelder, Wilhelm T S Huck, David Klenerman, and Chris Abell. Ultrarapid generation of femtoliter microfluidic droplets for single-molecule-counting immunoassays. *ACS Nano*, 7(7):5955–5964, 2013. ISSN 19360851. doi: 10.1021/nn401661d. URL `http://pubs.acs.org/doi/abs/10.1021/nn401661d`.

[4] Volker Hessel. From microreactor design to microreactor process design. *Chemical Engineering and Technology*, 28(3):243, 2005. ISSN 09307516. doi: 10.1002/ceat.200590004.

[5] George M. Whitesides. The origins and the future of microfluidics. *Nature*, 442(7101):368–373, 2006. ISSN 00280836. doi: 10.1038/nature05058.

[6] Andreas Manz, N Graber, and H Michael Widmers. Miniaturized total chemical analysis systems: A novel concept for chemical sensing. *Sensors and Actuators B: Chemical*, 1(1-6):244–248, 1990. ISSN 09254005. doi: 10.1016/0925-4005(90)80209-I. URL `http://linkinghub.elsevier.com/retrieve/pii/092540059080209I`.

[7] P. Abgrall and A. M. Gué. Lab-on-chip technologies: Making a microfluidic network and coupling it into a complete microsystem - A review. *Journal of Micromechanics and Microengineering*, 17(5), 2007. ISSN 09601317. doi: 10.1088/0960-1317/17/5/R01.

[8] Nam Trung Nguyen, Majid Hejazian, Chin Hong Ooi, and Navid Kashaninejad. Recent advances and future perspectives on microfluidic liquid handling. *Micromachines*, 8(6), 2017. ISSN 2072666X. doi: 10.3390/mi8060186.

[9] Elveflow. Microfluidics and microfluidic devices : a review. pages 1–9, 2015.

[10] Ryan D. Sochol, Eric Sweet, Casey C. Glick, Sung Yueh Wu, Chen Yang, Michael Restaino, and Liwei Lin. 3D printed microfluidics and microelectronics. *Microelectronic Engineering*, 189:52–68, 2018. ISSN 01679317. doi: 10.1016/j.mee.2017.12.010.

[11] I. Burdallo, C. Jimenez-Jorquera, C. Fernández-Sánchez, and A. Baldi. Integration of microelectronic chips in microfluidic systems on printed circuit board. *Journal of Micromechanics and Microengineering*, 22(10), 2012. ISSN 09601317. doi: 10.1088/0960-1317/22/10/105022.

[12] Lei Mou and Xingyu Jiang. Materials for Microfluidic Immunoassays: A Review. *Advanced Healthcare Materials*, 6(15):1–20, 2017. ISSN 21922659. doi: 10.1002/adhm.201601403.

[13] Ellert R. Nichols and Douglas B. Craig. Single molecule assays reveal differences between in vitro and in vivo synthesized β-galactosidase. *Protein Journal*, 27(6):376–383, 2008. ISSN 15723887. doi: 10.1007/s10930-008-9147-y.

[14] Amar S. Basu. Digital Assays Part II: Digital Protein and Cell Assays. *SLAS TECHNOLOGY: Translating Life Sciences Innovation*, 22(4):387–405, aug 2017. ISSN 2472-6303. doi: 10.1177/2472630317705681. URL `http://journals.sagepub.com/doi/10.1177/2472630317705681`.

[15] Hyun Soo Kim, Timothy P. Devarenne, and Arum Han. A high-throughput microfluidic single-cell screening platform capable of selective cell extraction. *Lab Chip*, 15(11):2467–2475, 2015. ISSN 1473-0197. doi: 10.1039/C4LC01316F. URL `http://pubs.rsc.org/en/content/articlehtml/2015/lc/c4lc01316f{%}5Cnhttp://xlink.rsc.org/?DOI=C4LC01316F`.

[16] Yunpeng Bai, Emilie Weibull, Haakan N. Joensson, and Helene Andersson-Svahn. Interfacing picoliter droplet microfluidics with addressable microliter compartments using fluorescence activated cell sorting. *Sensors and Actuators, B: Chemical*, 194:249–254, 2014. ISSN 09254005. doi: 10.1016/j.snb.2013.12.089. URL `http://dx.doi.org/10.1016/j.snb.2013.12.089`.

[17] J. Nilsson, M. Evander, B. Hammarström, and T. Laurell. Review of cell and particle trapping in microfluidic systems. *Analytica Chimica Acta*, 649(2):141–157, 2009. ISSN 00032670. doi: 10.1016/j.aca.2009.07.017.

[18] Westbrook M. Weaver, Peter Tseng, Anja Kunze, Mahdokht Masaeli, Aram J. Chung, Jaideep S. Dudani, Harsha Kittur, Rajan P. Kulkarni, and Dino Di Carlo. Advances in high-throughput single-cell microtechnologies. *Current Opinion in Biotechnology*, 25:114–123, 2014. ISSN 18790429. doi: 10.1016/j.copbio.2013.09.005. URL `http://dx.doi.org/10.1016/j.copbio.2013.09.005`.

[19] M. D. Tarn, S. N. F. Sikora, G. C. E. Porter, D. O 'sullivan, M. Adams, T. F. Whale, A. D. Harrison, J. Vergaratemprado, T. W. Wilson, J. Shim, and B. J. Murray. The study of atmospheric icenucleating particles via microfluidically generated droplets. *Microfluidics and Nanofluidics*, 22: 52, 2018. ISSN 1613-4990. doi: 10.1007/s10404-018-2069-x. URL https://doi.org/10.1007/s10404-018-2069-x.

[20] Robert Michael Van Dam. *Solvent-Resistant Elastomeric Microfluidic Devices and Applications(Part4)*. PhD thesis, feb 2005. URL http://thesis.library.caltech.edu/4796/.

[21] David J Beebe, Glennys a Mensing, and Glenn M Walker. Physics and applications of microfluidics in biology. *Annual review of biomedical engineering*, 4(October):261–286, jan 2002. ISSN 1523-9829. doi: 10.1146/annurev.bioeng.4.112601.125916. URL http://www.ncbi.nlm.nih.gov/pubmed/12117759http://www.annualreviews.org/doi/abs/10.1146/annurev.bioeng.4.112601.125916.

[22] Henrik Bruus. *Theoretical microfluidics*, volume 18. Oxford university press Oxford, 2008. ISBN 0199235090. doi: 10.1111/j.1574-6968.2009.01808.x.

[23] Andrew Evan Kamholz and Paul Yager. Theoretical analysis of molecular diffusion in pressure-driven laminar flow in microfluidic channels. *Biophysical Journal*, 80(1):155–160, 2001. ISSN 00063495. doi: 10.1016/S0006-3495(01)76003-1. URL http://dx.doi.org/10.1016/S0006-3495(01)76003-1.

[24] Lu Mi, Liang Huang, Junxiang Li, Guoqiang Xu, Qiong Wu, and Wenhui Wang. Fluidic circuit based high-efficiency and large-scale single cell trap. *Lab Chip*, pages 1–5, 2016. ISSN 1473-0197. doi: 10.1039/C6LC01120A. URL http://pubs.rsc.org/en/Content/ArticleLanding/2016/LC/C6LC01120A.

[25] Bendong Liu, Mohan Li, Baohua Tian, Xu Yang, and Jiahui Yang. A positive pressure-driven PDMS pump for fluid handling in microfluidic chips. *Microfluidics and Nanofluidics*, 22(9):94, 2018. ISSN 1613-4982. doi: 10.1007/s10404-018-2112-y. URL http://link.springer.com/10.1007/s10404-018-2112-y.

[26] Wenhua Zhang, Shuichao Lin, Chunming Wang, Jia Hu, Cong Li, Zhixia Zhuang, Yongliang Zhou, Richard A. Mathies, and Chaoyong James Yang. PMMA/PDMS valves and pumps for disposable microfluidics. *Lab on a Chip*, 9(21):3088, nov 2009. ISSN 1473-0197. doi: 10.1039/b907254c. URL http://xlink.rsc.org/?DOI=b907254c.

[27] Charles N. Baroud, Francois Gallaire, and Rémi Dangla. Dynamics of microfluidic droplets. *Lab on a Chip*, 10(16):2032, 2010. ISSN 1473-0197. doi: 10.1039/c001191f. URL http://pubs.rsc.org/en/content/articlehtml/2010/lc/c001191f.

[28] Shelley L. Anna and Hans C. Mayer. Microscale tipstreaming in a microfluidic flow focusing device. *Physics of Fluids*, 18(12):121512, 2006. ISSN 10706631. doi: 10.1063/1.2397023.

[29] Younan Xia and George M. Whitesides. Soft Lithography. *Annual Review of Materials Science*, 28(1):153–184, 1998. ISSN 0084-6600. doi: 10.1146/annurev.matsci.28.1.153. URL http://www.annualreviews.org/doi/abs/10.1146/annurev.matsci.28.1.153.

[30] Zongjie Wang. Detection and Automation Technologies for the Mass Production of Droplet. 3333(Figure 1), 2018. ISSN 19411189. doi: 10.1109/RBME.2018.2826984.

[31] Mazher-Iqbal Mohammed and Marc P Y Desmulliez. Lab-on-a-chip based immunosensor principles and technologies for the detection of cardiac biomarkers: a review. *Lab on a chip*, 11(4):569–95, 2011. ISSN 1473-0189. doi: 10.1039/c0lc00204f. URL http://www.ncbi.nlm.nih.gov/pubmed/21180774.

[32] Noa Cohen, Pooja Sabhachandani, Saheli Sarkar, Lindy Kahanovitz, Norman Lautsch, Steven J. Russell, and Tania Konry. Microsphere based continuous-flow immunoassay in a microfluidic device for determination of clinically relevant insulin levels. *Microchimica Acta*, 184(3):835–841, 2017. ISSN 14365073. doi: 10.1007/s00604-017-2072-z.

[33] Mingzhu Yang, Wei Zhang, Junchuan Yang, Binfeng Hu, Fengjing Cao, Wenshu Zheng, Yiping Chen, and Xingyu Jiang. Skiving stacked sheets of paper into test paper for rapid and multiplexed assay. *Science Advances*, 3(12):eaao4862, dec 2017. ISSN 2375-2548. doi: 10.1126/sciadv.aao4862. URL http://advances.sciencemag.org/lookup/doi/10.1126/sciadv.aao4862.

[34] Xiaoxia Zhu, Shidan Xiong, Jiaqin Zhang, Xiaoyu Zhang, Xin Tong, and Shan Kong. Improving paper-based ELISA performance through covalent immobilization of antibodies. *Sensors and Actuators B: Chemical*, aug 2017. ISSN 09254005. doi: 10.1016/j.snb.2017.08.090. URL http://linkinghub.elsevier.com/retrieve/pii/S0925400517315137.

[35] Mohit S. Verma, Maria Nefeli Tsaloglou, Tyler Sisley, Dionysios Christodouleas, Austin Chen, Jonathan Milette, and George M. Whitesides. Sliding-strip microfluidic device enables ELISA on paper. *Biosensors and Bioelectronics*, 99(July 2017):77–84, 2018. ISSN 18734235. doi: 10.1016/j.bios.2017.07.034. URL http://dx.doi.org/10.1016/j.bios.2017.07.034.

[36] Paul Watts and Charlotte Wiles. Micro reactors: A new tool for the synthetic chemist. *Organic and Biomolecular Chemistry*, 5(5):727–732, 2007. ISSN 14770520. doi: 10.1039/b617327f.

[37] Kangning Ren, Jianhua Zhou, and Hongkai Wu. Materials for microfluidic chip fabrication. *Accounts of Chemical Research*, 46(11):2396–2406, 2013. ISSN 00014842. doi: 10.1021/ar300314s.

[38] J. Cooper McDonald, David C. Duffy, Janelle R. Anderson, Daniel T. Chiu, Hongkai Wu, Olivier J. A. Schueller, and George M. Whitesides. Fabrication of microfluidic systems in poly(dimethylsiloxane). *Electrophoresis*, 21(1):27–40, 2000. ISSN 0173-0835. doi: 10.1002/(SICI)1522-2683(20000101)21:1⟨27::AID-ELPS27⟩3.0.CO;2-C. URL http://doi.wiley.com/10.1002/(SICI)1522-2683(20000101)21:1{%}3C27::AID-ELPS27{%}3E3.0.CO;2-C.

[39] Chenlu Hou. Photopatterned polyacrylamide gels enable efficient microfluidic protein assays. 2011.

[40] Renato S. Lima, Paulo A.G.C. Leão, Maria H.O. Piazzetta, Alessandra M. Monteiro, Leandro Y. Shiroma, Angelo L. Gobbi, and Emanuel Carrilho. Sacrificial adhesive bonding: A powerful method for fabrication of glass microchips. *Scientific Reports*, 5:1–15, 2015. ISSN 20452322. doi: 10.1038/srep13276. URL http://dx.doi.org/10.1038/srep13276.

[41] Sally A. Peyman, Radwa H. Abou-Saleh, James R. McLaughlan, Nicola Ingram, Benjamin R.G. Johnson, Kevin Critchley, Steven Freear, J. Anthony Evans, Alexander F. Markham, P. Louise Coletta, and Stephen D. Evans. Expanding 3D geometry for enhanced on-chip microbubble production and single step formation of liposome modified microbubbles. *Lab on a Chip*, 12(21):4544–4552, 2012. ISSN 14730189. doi: 10.1039/c2lc40634a.

[42] David C. Duffy, J. Cooper McDonald, Olivier J A Schueller, and George M. Whitesides. Rapid prototyping of microfluidic systems in poly(dimethylsiloxane). *Analytical Chemistry*, 70(23):4974–4984, 1998. ISSN 00032700. doi: 10.1021/ac980656z.

[43] Samuel K. Sia and George M. Whitesides. Microfluidic devices fabricated in poly(dimethylsiloxane) for biological studies. *Electrophoresis*, 24(21): 3563–3576, 2003. ISSN 01730835. doi: 10.1002/elps.200305584.

[44] Yongha Hwang and Rob N. Candler. Non-planar PDMS microfluidic channels and actuators: a review. *Lab Chip*, 2017. ISSN 1473-0197. doi: 10.1039/C7LC00523G. URL http://xlink.rsc.org/?DOI=C7LC00523G.

[45] M. A. Unger. Monolithic Microfabricated Valves and Pumps by Multilayer Soft Lithography. *Science*, 288(5463):113–116, 2000. ISSN 00368075. doi: 10.1126/science.288.5463.113. URL http://www.sciencemag.org/cgi/doi/10.1126/science.288.5463.113.

[46] Hsiang Y. Wang, Ning Bao, and Chang Lu. A microfluidic cell array with individually addressable culture chambers. *Biosensors and Bioelectronics*, 24(4):613–617, 2008. ISSN 09565663. doi: 10.1016/j.bios.2008.06.005.

[47] T. Thorsen. Microfluidic Large-Scale Integration. *Science*, 298(5593): 580–584, 2002. ISSN 00368075. doi: 10.1126/science.1076996. URL http://www.sciencemag.org/cgi/doi/10.1126/science.1076996.

[48] Soon-Eng Ong. Fundamental principles and applications of microfluidic systems. *Frontiers in Bioscience*, 13(13):2757, 2008. ISSN 10939946. doi: 10.2741/2883. URL http://www.bioscience.org/2008/v13/af/2883/list.htm.

[49] Howard A. Stone. Introduction to Fluid Dynamics for Microfluidic Flows. In *CMOS Biotechnology*, chapter 2, pages 5–30. 2007. ISBN 0-387-36836-1. doi: 10.1007/978-0-387-68913-5_2. URL http://link.springer.com/10.1007/978-0-387-68913-5{_}2.

[50] Yechun Wang and Panagiotis Dimitrakopoulos. Low-Reynolds-number droplet motion in a square microfluidic channel. *Theoretical and Computational Fluid Dynamics*, 26(1-4):361–379, jan 2012. ISSN 0935-4964. doi: 10.1007/s00162-011-0238-6. URL http://link.springer.com/10.1007/s00162-011-0238-6.

[51] J K Nunes, S S H Tsai, J Wan, and H a Stone. Dripping and jetting in microfluidic multiphase flows applied to particle and fiber synthesis. *Journal of physics D: Applied physics*, 46(11):114002, mar 2013. ISSN 0022-3727. doi: 10.1088/0022-3727/46/11/114002. URL http://iopscience.iop.org/0022-3727/46/11/114002/article/.

[52] Sungyoung Choi, Myung Gwon Lee, and Je Kyun Parka. Microfluidic parallel circuit for measurement of hydraulic resistance. *Biomicrofluidics*, 4(3):1–9, 2010. ISSN 19321058. doi: 10.1063/1.3486609.

[53] H Amini, W Lee, and D Di Carlo. Inertial microfluidic physics. *Lab Chip*, 14(15):2739–2761, 2014. ISSN 1473-0189. doi: 10.1039/c4lc00128a. URL http://www.ncbi.nlm.nih.gov/pubmed/24914632.

[54] Chase Jonathan Hansel. *MAPPING OF PRESSURE LOSSES THROUGH MICROCHANNELS WITH SWEEPING-BENDS OF VARIOUS ANGLE AND RADII*. PhD thesis, 2006. URL http://etd.fcla.edu/CF/CFE0002091/Hansel{_}Chase{_}J{_}200805{_}MS.pdf.

[55] Peter Atkins and J De Paula. *Atkins' Physical chemistry 9th edition*. Oxford university press, 2009. ISBN 9780199543373. doi: 10.1021/ed056pA260.1. URL http://library.wur.nl/WebQuery/clc/1842621{%}5Cnhttp://scholar.google.com/scholar?hl=en{&}btnG=Search{&}q=intitle:Atkins'+physical+chemistry{#}1{%}5Cnhttp://www.oup.co.uk/pdf/hechemcat08/physicalchemistry.pdf{%}5Cnhttp://www.oup.co.uk/pdf/hechemcat08/physicalchemistr.

[56] Kwang W Oh, Kangsun Lee, Byungwook Ahn, and Edward P Furlani. Design of pressure-driven microfluidic networks using electric circuit analogy. *Lab on a chip*, 12(3):515–45, 2012. ISSN 1473-0189. doi: 10.1039/c2lc20799k. URL http://www.ncbi.nlm.nih.gov/pubmed/22179505.

[57] Helen Song, Joshua D Tice, and Rustem F Ismagilov. A Microfluidic System for Controlling Reaction Networks in Time. *Angewandte Chemie, International Edition in English*, 42(7):768–772, feb 2003. ISSN 00448249. doi: 10.1002/ange.19350483406. URL http://doi.wiley.com/10.1002/anie.200390203.

[58] Yuan-Sheng Lee, Nirveek Bhattacharjee, and Albert Folch. 3D-Printed Quake-Style Microvalves and Micropumps. *Lab on a Chip*, (c):210–212, 2018. ISSN 1473-0197. doi: 10.1039/C8LC00001H. URL http://pubs.rsc.org/en/Content/ArticleLanding/2018/LC/C8LC00001H.

[59] Pablo E. Guevara-Pantoja, Rocío J. Jiménez-Valdés, Jose L. García-Cordero, and Gabriel A. Caballero-Robledo. Pressure-actuated monolithic acrylic microfluidic valves and pumps. *Lab on a Chip*, 18(4):662–669, 2018. ISSN 14730189. doi: 10.1039/c7lc01337j. URL http://pubs.rsc.org/en/Content/ArticleLanding/2018/LC/C7LC01337J.

[60] Shia-Yen Teh, Robert Lin, Lung-Hsin Hung, and Abraham P Lee. Droplet microfluidics. *Lab on a chip*, 8(2):198–220, 2008. ISSN 1473-0197. doi: 10.1039/b715524g.

[61] Isao Kobayashi, Sukekuni Mukataka, and Mitsutoshi Nakajima. Production of monodisperse oil-in-water emulsions using a large silicon straight-through microchannel plate. *Industrial and Engineering Chemistry Research*, 44(15):5852–5856, 2005. ISSN 08885885. doi: 10.1021/ie050013r.

[62] Marie Leman, Faris Abouakil, Andrew D. Griffiths, and Patrick Tabeling. Droplet-based microfluidics at the femtolitre scale. *Lab Chip*, 15(3):753–765, 2015. ISSN 1473-0197. doi: 10.1039/C4LC01122H. URL http://pubs.rsc.org/en/content/articlehtml/2015/lc/c4lc01122h{%}5Cnhttp://xlink.rsc.org/?DOI=C4LC01122H.

[63] Joshua D. Tice, Helen Song, Adam D. Lyon, and Rustem F. Ismagilov. Formation of Droplets and Mixing in Multiphase Microfluidics at Low Values of the Reynolds and the Capillary Numbers. *Langmuir*, 19(22):9127–9133, 2003. ISSN 07437463. doi: 10.1021/la030090w.

[64] Andrew S. Utada, Alberto Fernandez-Nieves, Howard A. Stone, and David A. Weitz. Dripping to jetting transitions in coflowing liquid streams. *Physical Review Letters*, 99(9):1–4, 2007. ISSN 00319007. doi: 10.1103/PhysRevLett.99.094502.

[65] Shelley Lynn Anna. Droplets and Bubbles in Microfluidic Devices. *Annual Review of Fluid Mechanics*, 48(1):285–309, 2016. ISSN 0066-4189. doi: 10.1146/annurev-fluid-122414-034425. URL http://dx.

doi.org/10.1146/annurev-fluid-122414-034425{%}5Cnhttp://www.annualreviews.org/doi/10.1146/annurev-fluid-122414-034425.

[66] Elena Castro-Hernández, Maarten P. Kok, Michel Versluis, and David Fernandez Rivas. Study of the geometry in a 3D flow-focusing device. *Microfluidics and Nanofluidics*, 20(2):1–8, 2016. ISSN 16134990. doi: 10.1007/s10404-016-1708-3. URL http://link.springer.com/10.1007/s10404-016-1708-3.

[67] Qingyi Xu and Mitsutoshi Nakajima. The generation of highly monodisperse droplets through the breakup of hydrodynamically focused microthread in a microfluidic device. *Applied Physics Letters*, 85(17): 3726–3728, oct 2004. ISSN 0003-6951. doi: 10.1063/1.1812380. URL http://aip.scitation.org/doi/10.1063/1.1812380.

[68] A. S. Utada, E. Lorenceau, D. R. Link, P. D. Kaplan, H. A. Stone, and D. A. Weitz. Monodisperse Double Emulsions Generated from a Microcapillary Device. *Science*, 308(5721):537–541, apr 2005. ISSN 0036-8075. doi: 10.1126/science.1109164. URL http://www.sciencemag.org/cgi/doi/10.1126/science.1109164.

[69] Armend Gazmeno Håti, Tomasz Szymborski, Mathias Steinacher, and Esther Amstad. Production of monodisperse drops from viscous fluids. *Lab on a Chip*, 2018. ISSN 1473-0197. doi: 10.1039/C7LC01322A. URL http://pubs.rsc.org/en/Content/ArticleLanding/2018/LC/C7LC01322A.

[70] Mark A. Levenstein, Lukmaan A. Bawazer, Ciara S. Mc Nally, William J. Marchant, Xiuqing Gong, Fiona C. Meldrum, and Nikil Kapur. A reproducible approach to the assembly of microcapillaries for double emulsion production. *Microfluidics and Nanofluidics*, 20(10):1–11, 2016. ISSN 16134990. doi: 10.1007/s10404-016-1806-2.

[71] Eric Y. Liu, Sukwon Jung, David A. Weitz, Hyunmin Yi, and Chang-Hyung Choi. High-throughput double emulsion-based microfluidic production of hydrogel microspheres with tunable chemical functionalities toward biomolecular conjugation. *Lab on a Chip*, 18:323–334, 2018. ISSN 1473-0197. doi: 10.1039/C7LC01088E. URL http://xlink.rsc.org/?DOI=C7LC01088E.

[72] Deyong Zhu, Xiaohu Zhou, and Bo Zheng. A double emulsion-based, plastic-glass hybrid microfluidic platform for protein crystallization. *Micromachines*, 6(11):1629–1644, 2015. ISSN 2072666X. doi: 10.3390/mi6111446.

[73] Jean-Christophe Christophe Baret. Surfactants in droplet-based microfluidics. *Lab on a Chip*, 12(3):422–433, 2011. ISSN 1473-0197. doi: 10.1039/C1LC20582J. URL papers2://publication/uuid/4D5974D9-2461-4BEE-BFBC-906192A39BF6.

[74] Xiaonan Xu, Haojun Yuan, Ruyuan Song, Miao Yu, Ho Yin Chung, Youmin Hou, Yuhe Shang, Hongbo Zhou, Xiaonan Xu, Haojun Yuan, Ruyuan Song, Miao Yu, and Ho Yin Chung. High aspect ratio induced spontaneous generation of monodisperse picolitre droplets for digital PCR High aspect ratio induced spontaneous generation of monodisperse picolitre droplets for digital PCR. 014103, 2018.

[75] Li Lu, Jeffrey W. Schertzer, and Paul R. Chiarot. Continuous microfluidic fabrication of synthetic asymmetric vesicles. *Lab Chip*, 2015. ISSN 1473-0197. doi: 10.1039/C5LC00520E. URL `http://xlink.rsc.org/?DOI=C5LC00520E`.

[76] Jinyu Chen, Zhaofeng Luo, Lin Li, Jinlong He, Luoquan Li, Jian-Wei Zhu, Ping Wu, and Liqun He. Capillary-based Integrated Digital PCR in Picoliter Droplets. *Lab on a Chip*, 2017. ISSN 1473-0197. doi: 10.1039/C7LC01160A. URL `http://pubs.rsc.org/en/Content/ArticleLanding/2017/LC/C7LC01160A`.

[77] Shuo Wang, Andrew Bruning, Oju Jeon, Fei Long, Eben Alsberg, and Chang Kyoung Choi. An in-situ photocrosslinking microfluidic technique to generate non-spherical, cytocompatible, degradable, monodisperse alginate microgels for chondrocyte encapsulation. *Biomicrofluidics*, 12(1):014106, jan 2018. ISSN 1932-1058. doi: 10.1063/1.5017644. URL `http://aip.scitation.org/doi/10.1063/1.5017644`.

[78] Philip C Gach, Kosuke Iwai, Peter Kim, Nathan Hillson, and Anup K Singh. Droplet Microfluidics for Synthetic Biology. *Lab Chip*, 17:3388–3400, 2017. ISSN 1473-0197. doi: 10.1039/C7LC00576H. URL `http://pubs.rsc.org/en/Content/ArticleLanding/2017/LC/C7LC00576H`.

[79] Yu-Dong Ma, Kang Luo, Wen-Hsin Chang, and Gwo-Bin Lee. A microfluidic chip capable of generating and trapping emulsion droplets for digital loop-mediated isothermal amplification analysis. *Lab on a Chip*, 2017. ISSN 1473-0197. doi: 10.1039/C7LC01004D. URL `http://xlink.rsc.org/?DOI=C7LC01004D`.

[80] Haishui Huang and Xiaoming He. Fluid displacement during droplet formation at microfluidic flow-focusing junctions. *Lab on a chip*, 15(21):4197–205, 2015. ISSN 1473-0189. doi: 10.1039/c5lc00730e. URL `http://pubs.rsc.org/en/content/articlehtml/2015/lc/c5lc00730ehttp://xlink.rsc.org/?DOI=C4LC01155Dhttp://xlink.rsc.org/?DOI=C5LC00730E`.

[81] Brian J Adzima and Sachin S Velankar. Pressure drops for droplet flows in microfluidic channels. *Journal of Micromechanics and Microengineering*, 16(8):1504–1510, 2006. ISSN 0960-1317. doi: 10.1088/0960-1317/16/8/010.

[82] J. R. Haliburton, S. C. Kim, I. C. Clark, R. A. Sperling, D. A. Weitz, and A. R. Abate. Efficient extraction of oil from droplet microfluidic

emulsions. *Biomicrofluidics*, 11(3), 2017. ISSN 19321058. doi: 10.1063/1.4984035.

[83] C. Holtze, A. C. Rowat, J. J. Agresti, J. B. Hutchison, F. E. Angilè, C. H. J. Schmitz, S. Köster, H. Duan, K. J. Humphry, R. A. Scanga, J. S. Johnson, D. Pisignano, and D. A. Weitz. Biocompatible surfactants for water-in-fluorocarbon emulsions. *Lab on a Chip*, 8(10):1632, 2008. ISSN 1473-0197. doi: 10.1039/b806706f. URL `http://xlink.rsc.org/?DOI=b806706f`.

[84] Olaf Wagner, Julian Thiele, Marie Weinhart, Linas Mazutis, David A. Weitz, Wilhelm T S Huck, and Rainer Haag. Biocompatible fluorinated polyglycerols for droplet microfluidics as an alternative to PEG-based copolymer surfactants. *Lab on a chip*, 16(1):65–9, 2016. ISSN 1473-0189. doi: 10.1039/c5lc00823a. URL `http://pubs.rsc.org/en/Content/ArticleLanding/2015/LC/C5LC00823Ahttp://www.ncbi.nlm.nih.gov/pubmed/26626826`.

[85] Gianluca Etienne, Michael Kessler, and Esther Amstad. Influence of Fluorinated Surfactant Composition on the Stability of Emulsion Drops. *Macromolecular Chemistry and Physics*, 218(2):1600365, jan 2017. ISSN 10221352. doi: 10.1002/macp.201600365. URL `http://doi.wiley.com/10.1002/macp.201600365`.

[86] Dong Ku Kang, Xiuqing Gong, Soongwon Cho, Jin Young Kim, Joshua B. Edel, Soo Ik Chang, Jaebum Choo, and Andrew J. Demello. 3D Droplet Microfluidic Systems for High-Throughput Biological Experimentation. *Analytical Chemistry*, 87(21):10770–10778, 2015. ISSN 15206882. doi: 10.1021/acs.analchem.5b02402.

[87] Ana I. Barbosa and Nuno M. Reis. A critical insight into the development pipeline of microfluidic immunoassay devices for the sensitive quantitation of protein biomarkers at the point of care. *The Analyst*, 142(6):858–882, 2017. ISSN 0003-2654. doi: 10.1039/C6AN02445A. URL `http://xlink.rsc.org/?DOI=C6AN02445A`.

[88] Francesco Piraino, Francesca Volpetti, Craig Watson, and Sebastian J. Maerkl. A digital-Analog microfluidic platform for patient-centric multiplexed biomarker diagnostics of ultralow volume samples. *ACS Nano*, 10(1):1699–1710, 2016. ISSN 1936086X. doi: 10.1021/acsnano.5b07939. URL `http://pubs.acs.org/doi/10.1021/acsnano.5b07939`.

[89] Oliver J. Dressler, Richard M. Maceiczyk, Soo Ik Chang, and Andrew J. Demello. Droplet-based microfluidics: Enabling impact on drug discovery. *Journal of Biomolecular Screening*, 19(4):483–496, 2014. ISSN 10870571. doi: 10.1177/1087057113510401. URL `http://www.ncbi.nlm.nih.gov/pubmed/24241711`.

[90] Galder Cristobal, Laurence Arbouet, Flavie Sarrazin, David Talaga, Jean-Luc Bruneel, Mathieu Joanicot, and Laurent Servant. On-line laser

Raman spectroscopic probing of droplets engineered in microfluidic devices. *Lab on a Chip*, 6(9):1140, sep 2006. ISSN 1473-0197. doi: 10.1039/b602702d. URL http://xlink.rsc.org/?DOI=b602702d.

[91] Richard M. Maceiczyk, David Hess, Flora W.Y. Chiu, Stavros Stavrakis, and Andrew J. DeMello. Differential detection photothermal spectroscopy: Towards ultra-fast and sensitive label-free detection in picoliter & femtoliter droplets. *Lab on a Chip*, 17(21):3654–3663, 2017. ISSN 14730189. doi: 10.1039/c7lc00946a. URL http://xlink.rsc.org/?DOI=C7LC00946A.

[92] Bodong Yang, Yangcheng Lu, and Guangsheng Luo. Controllable preparation of polyacrylamide hydrogel microspheres in a coaxial microfluidic device. *Industrial and Engineering Chemistry Research*, 51(26):9016–9022, 2012. ISSN 08885885. doi: 10.1021/ie3004013.

[93] Meng Sun and Siva A. Vanapalli. Generation of chemical concentration gradients in mobile droplet arrays via fragmentation of long immiscible diluting plugs. *Analytical Chemistry*, 85(4):2044–2048, 2013. ISSN 00032700. doi: 10.1021/ac303526y.

[94] Si Hyung Jin, Heon-Ho Jeong, Byungjin Lee, Sung Sik Lee, and Chang-Soo Lee. A programmable microfluidic static droplet array for droplet generation, transportation, fusion, storage, and retrieval. *Lab Chip*, 15:3677–3686, 2015. ISSN 1473-0197. doi: 10.1039/C5LC00651A. URL http://dx.doi.org/10.1039/C5LC00651A{%}5Cnhttp://xlink.rsc.org/?DOI=C5LC00651A.

[95] Samin Akbari and Tohid Pirbodaghi. A droplet-based heterogeneous immunoassay for screening single cells secreting antigen-specific antibodies. *Lab on a chip*, 14(17):3275–80, 2014. ISSN 1473-0189. doi: 10.1039/c4lc00082j. URL http://www.ncbi.nlm.nih.gov/pubmed/24989431.

[96] Sungho Jang, Byungjin Lee, Heon-Ho Jeong, Si Hyung Jin, Sungyeon Jang, Seong Gyeong Kim, Gyoo Yeol Jung, and Chang-Soo Lee. On-chip analysis, indexing and screening for chemical producing bacteria in microfluidic static droplet array. *Lab Chip*, 16:10.1039/C6LC00118A, 2016. ISSN 1473-0197. doi: 10.1039/C6LC00118A. URL http://pubs.rsc.org/en/Content/ArticleLanding/2016/LC/C6LC00118A.

[97] Linas Mazutis, John Gilbert, W Lloyd Ung, David A Weitz, Andrew D Griffiths, and John A Heyman. Single-cell analysis and sorting using droplet-based microfluidics. *Nat. Protocols*, 8(5):870–891, 2013. ISSN 1750-2799. doi: 10.1038/nprot.2013.046\rhttp://www.nature.com/nprot/journal/v8/n5/abs/nprot.2013.046.html#supplementary-information. URL http://www.ncbi.nlm.nih.gov/pubmed/23558786{%}5Cnhttp://dx.doi.org/10.1038/nprot.2013.046.

[98] David J. Collins, Adrian Neild, Andrew DeMello, Ai Qun Liu, and Ye Ai. The Poisson distribution and beyond: Methods for microfluidic droplet production and single cell encapsulation. *Lab on a Chip*, 15(17):3439–3459, 2015. ISSN 14730189. doi: 10.1039/c5lc00614g. URL `http://pubs.rsc.org/en/content/articlehtml/2015/lc/c5lc00614g`.

[99] Samaneh Mashaghi, Alireza Abbaspourrad, David A. Weitz, and Antoine M. van Oijen. Droplet microfluidics: A tool for biology, chemistry and nanotechnology. *TrAC - Trends in Analytical Chemistry*, 82:118–125, sep 2016. ISSN 18793142. doi: 10.1016/j.trac.2016.05.019. URL `http://linkinghub.elsevier.com/retrieve/pii/S0165993616300061`.

[100] Wei Lung Chou, Pee Yew Lee, Cing Long Yang, Wen Ying Huang, and Yung Sheng Lin. Recent advances in applications of droplet microfluidics. *Micromachines*, 6(9):1249–1271, 2015. ISSN 2072666X. doi: 10.3390/mi6091249.

[101] Stefanie Utech, Radivoje Prodanovic, Angelo S. Mao, Raluca Ostafe, David J. Mooney, and David A. Weitz. Microfluidic Generation of Monodisperse, Structurally Homogeneous Alginate Microgels for Cell Encapsulation and 3D Cell Culture. *Advanced Healthcare Materials*, 4(11):1628–1633, aug 2015. ISSN 21922659. doi: 10.1002/adhm.201500021. URL `http://doi.wiley.com/10.1002/adhm.201500021`.

[102] Jason P. Beech and Jonas O. Tegenfeldt. Tuneable separation in elastomeric microfluidics devices. *Lab on a Chip*, 8(5):657–659, 2008. ISSN 14730189. doi: 10.1039/b719449h.

[103] Yan Pang, Hyoungsoo Kim, Zhaomiao Liu, and Howard A. Stone. A soft microchannel decreases polydispersity of droplet generation. *Lab on a Chip*, 14(20):4029–4034, 2014. ISSN 14730189. doi: 10.1039/c4lc00871e.

[104] Ok Chan Jeong, Sin Wook Park, Sang Sik Yang, and James Jungho Pak. Fabrication of a peristaltic PDMS micropump. *Sensors and Actuators, A: Physical*, 123-124:453–458, 2005. ISSN 09244247. doi: 10.1016/j.sna.2005.01.035.

[105] Seyed Hossein Hassanpour and Mohammadamin Dehghani. Review of cancer from perspective of molecular. *Journal of Cancer Research and Practice*, 4(4):127–129, 2017. ISSN 23113006. doi: 10.1016/j.jcrpr.2017.07.001. URL `http://linkinghub.elsevier.com/retrieve/pii/S2311300617300125`.

[106] Samir M. Hanash, Christina S. Baik, and Olli Kallioniemi. Emerging molecular biomarkers-blood-based strategies to detect and monitor cancer. *Nature Reviews Clinical Oncology*, 8(3):142–150, 2011. ISSN 17594774. doi: 10.1038/nrclinonc.2010.220. URL `http://dx.doi.org/10.1038/nrclinonc.2010.220`.

[107] Jennifer M. Croswell. Cumulative Incidence of False-Positive Test Results in Lung Cancer Screening. *Annals of Internal Medicine*, 152(8):505, apr 2010. ISSN 0003-4819. doi: 10.7326/0003-4819-152-8-201004200-00007. URL http://annals.org/article.aspx?doi=10.7326/0003-4819-152-8-201004200-00007.

[108] Olga Golubnitschaja and Josef Flammer. What Are the Biomarkers for Glaucoma? *Survey of Ophthalmology*, 52(6 SUPPL.):155–161, 2007. ISSN 00396257. doi: 10.1016/j.survophthal.2007.08.011.

[109] Charles L. Sawyers. The cancer biomarker problem. *Nature*, 452(7187): 548–552, 2008. ISSN 14764687. doi: 10.1038/nature06913.

[110] Fatih Inci, Chiara Filippini, Murat Baday, Mehmet Ozgun Ozen, Semih Calamak, Naside Gozde Durmus, ShuQi Wang, Emily Hanhauser, Kristen S Hobbs, Franceline Juillard, Ping Ping Kuang, Michael L Vetter, Margot Carocci, Hidemi S Yamamoto, Yuko Takagi, Umit Hakan Yildiz, Demir Akin, Duane R Wesemann, Amit Singhal, Priscilla L Yang, Max L Nibert, Raina N Fichorova, Daryl T-Y Lau, Timothy J Henrich, Kenneth M Kaye, Steven C Schachter, Daniel R Kuritzkes, Lars M Steinmetz, Sanjiv S Gambhir, Ronald W Davis, and Utkan Demirci. Multitarget, quantitative nanoplasmonic electrical field-enhanced resonating device (NE2RD) for diagnostics. *Proceedings of the National Academy of Sciences of the United States of America*, 112(32):E4354–63, aug 2015. ISSN 1091-6490. doi: 10.1073/pnas.1510824112. URL http://www.ncbi.nlm.nih.gov/pubmed/26195743.

[111] Md. Azahar Ali, Shawana Tabassum, Qiugu Wang, Yifei Wang, Ratnesh Kumar, and Liang Dong. Integrated dual-modality microfluidic sensor for biomarker detection using lithographic plasmonic crystal. *Lab on a Chip*, 18(5):803–817, 2018. ISSN 1473-0197. doi: 10.1039/C7LC01211J. URL http://dx.doi.org/10.1039/C7LC01211Jhttp://xlink.rsc.org/?DOI=C7LC01211J.

[112] Scott M Tabakman, Lana Lau, Joshua T Robinson, Jordan Price, Sarah P Sherlock, Hailiang Wang, Bo Zhang, Zhuo Chen, Stephanie Tangsombatvisit, Justin a Jarrell, Paul J Utz, and Hongjie Dai. Plasmonic substrates for multiplexed protein microarrays with femtomolar sensitivity and broad dynamic range. *Nature communications*, 2:466, 2011. ISSN 2041-1723. doi: 10.1038/ncomms1477. URL http://dx.doi.org/10.1038/ncomms1477.

[113] Maria Sánchez-Purrà, Marc Carré-Camps, Helena de Puig, Irene Bosch, Lee Gehrke, and Kimberly Hamad-Schifferli. Surface-Enhanced Raman Spectroscopy-Based Sandwich Immunoassays for Multiplexed Detection of Zika and Dengue Viral Biomarkers. *ACS Infectious Diseases*, page acsinfecdis.7b00110, 2017. ISSN 2373-8227. doi: 10.1021/acsinfecdis.7b00110. URL http://pubs.acs.org/doi/abs/10.1021/acsinfecdis.7b00110.

[114] Khondakar Kamil Reza, Jing Wang, Ramanathan Vaidyanathan, Shuvashis Dey, Yuling Wang, and Matt Trau. Electrohydrodynamic-Induced SERS Immunoassay for Extensive Multiplexed Biomarker Sensing. *Small*, 13(9):1602902, mar 2017. ISSN 16136810. doi: 10.1002/smll.201602902. URL http://doi.wiley.com/10.1002/smll.201602902.

[115] Yu Wang, Li-Juan Tang, and Jian-Hui Jiang. Surface-enhanced Raman spectroscopy-based, homogeneous, multiplexed immunoassay with antibody-fragments-decorated gold nanoparticles. *Analytical chemistry*, 85(19):9213–20, oct 2013. ISSN 1520-6882. doi: 10.1021/ac4019439. URL http://dx.doi.org/10.1021/ac4019439.

[116] Agnieszka Kamińska, Katarzyna Winkler, Aneta Kowalska, Evelin Witkowska, Tomasz Szymborski, Anna Janeczek, and Jacek Waluk. SERS-based Immunoassay in a Microfluidic System for the Multiplexed Recognition of Interleukins from Blood Plasma: Towards Picogram Detection. *Scientific Reports*, 7(1):10656, 2017. ISSN 2045-2322. doi: 10.1038/s41598-017-11152-w. URL http://www.nature.com/articles/s41598-017-11152-w.

[117] Jeremy Driskell. Surface-enhanced Raman scattering (SERS) for detection in immunoassays: applications, fundamentals, and optimization, 2006. URL http://lib.dr.iastate.edu/cgi/viewcontent.cgi?article=2931{&}context=rtd.

[118] N M Toriello, E S Douglas, N Thaitrong, S C Hsiao, M B Francis, C R Bertozzi, and R A Mathies. Integrated microfluidic bioprocessor for single-cell gene expression analysis. *Proc Natl Acad Sci U S A*, 105 (51):20173–20178, 2008. ISSN 1091-6490. doi: 10.1073/pnas.0806355106. URL http://www.ncbi.nlm.nih.gov/pubmed/19075237.

[119] Thermo Scientific. ELISA technical guide and protocols. *Thermo Scientific*, 65(815):1–14, 2010.

[120] Shahila Parween, Gaurav Singh, and Pradip Nahar. Ultrafast image-based ELISA for sensitive detection of cytokines in allergen-induced asthmatic samples. *Microchemical Journal*, 135:26–32, 2017. ISSN 0026265X. doi: 10.1016/j.microc.2017.07.013. URL http://linkinghub.elsevier.com/retrieve/pii/S0026265X1730406X.

[121] K. M. Koczula and A. Gallotta. Lateral flow assays. *Essays In Biochemistry*, 60(1):111–120, 2016. ISSN 0071-1365. doi: 10.1042/ebc20150012.

[122] Li Wu and Xiaogang Qu. Cancer biomarker detection: recent achievements and challenges. *Chemical Society reviews*, pages 2963–2997, 2015. ISSN 1460-4744. doi: 10.1039/c4cs00370e. URL http://pubs.rsc.org/en/Content/ArticleHTML/2015/CS/C4CS00370E.

[123] Malu Polanski and N Leigh Anderson. A list of candidate cancer biomarkers for targeted proteomics. *Biomarker insights*, 1(301):1–48, 2007. ISSN 1177-2719.

[124] Thomas D Pollard. A guide to simple and informative binding assays. *Molecular biology of the cell*, 21:4061–4067, 2010. ISSN 1059-1524. doi: 10.1091/mbc.E10-08-0683.

[125] David M Holtzman, John C Morris, and Alison M Goate. Alzheimer's disease: the challenge of the second century. *Science translational medicine*, 3(77):77sr1, 2011. ISSN 1946-6242. doi: 10.1126/scitranslmed.3002369. URL http://www.ncbi.nlm.nih.gov/pubmed/21471435{%}0Ahttp://www.pubmedcentral.nih.gov/articlerender.fcgi?artid=PMC3130546.

[126] David M Rissin, Cheuk W Kan, Todd G Campbell, Stuart C Howes, David R Fournier, Linan Song, Tomasz Piech, Purvish P Patel, Lei Chang, Andrew J Rivnak, Evan P Ferrell, Jeffrey D Randall, Gail K Provuncher, David R Walt, and David C Duffy. Single-molecule enzyme-linked immunosorbent assay detects serum proteins at subfemtomolar concentrations. *Nature Biotechnology*, 28(6):595–599, jun 2010. ISSN 1087-0156. doi: 10.1038/nbt.1641. URL http://dx.doi.org/10.1038/nbt.1641http://www.nature.com/doifinder/10.1038/nbt.1641.

[127] Han Wei Hou, Ali Asgar S Bhagat, Wong Cheng Lee, Sha Huang, Jongyoon Han, and Chwee Teck Lim. Microfluidic devices for blood fractionation. *Micromachines*, 2(3):319–343, 2011. ISSN 2072666X. doi: 10.3390/mi2030319.

[128] N Madaboosi, R R G Soares, V Chu, and J P Conde. A microfluidic immunoassay platform for the detection of free prostate specific antigen: A systematic and quantitative approach. *Analyst*, 140(13):4423–4433, 2015. ISSN 0003-2654. doi: 10.1039/c5an00364d. URL http://www.scopus.com/inward/record.url?eid=2-s2.0-84931050325{&}partnerID=40{&}md5=f4c4c564384cc878c635f247934a6778.

[129] Fei Fan, Haiying Shen, Guojun Zhang, Xingyu Jiang, and Xixiong Kang. Chemiluminescence immunoassay based on microfluidic chips for α-fetoprotein. *Clinica Chimica Acta*, 431:113–117, 2014. ISSN 00098981. doi: 10.1016/j.cca.2014.02.003. URL http://dx.doi.org/10.1016/j.cca.2014.02.003.

[130] Huashan Wang, Juanjuan Li, Xiaoqing Zhang, Binfeng Hu, Yang Liu, Lin Zhang, Ruitao Cha, Jiashu Sun, and Xingyu Jiang. A microfluidic indirect competitive immunoassay for multiple and sensitive detection of testosterone in serum and urine. *Analyst*, 141(3):815–819, 2016. ISSN 13645528. doi: 10.1039/c5an01835h.

[131] Pooja Sabhachandani, Noa Cohen, Saheli Sarkar, and Tania Konry. Microsphere-based immunoassay integrated with a microfluidic network to perform logic operations. *Microchimica Acta*, 182(9-10):1835–1840, 2015. ISSN 0026-3672. doi: 10.1007/s00604-015-1518-4.

[132] Wenying Pan, Wei Chen, and Xingyu Jiang. Letters to Analytical Chemistry Microfluidic Western Blot. *Society*, 82(10):3974–3976, 2010.

[133] Sha He, Yi Zhang, Pei Wang, Xingzhi Xu, Kui Zhu, Wenying Pan, Wenwen Liu, Kaiyong Cai, Jiashu Sun, Wei Zhang, and Xingyu Jiang. Multiplexed microfluidic blotting of proteins and nucleic acids by parallel, serpentine microchannels. *Lab on a Chip*, 15(1):105–112, 2015. ISSN 14730189. doi: 10.1039/c4lc00901k.

[134] Yi Zhang, Jiashu Sun, Yu Zou, Wenwen Chen, Wei Zhang, Jianzhong Jeff Xi, and Xingyu Jiang. Barcoded microchips for biomolecular assays. *Analytical Chemistry*, 87(2):900–906, 2015. ISSN 15206882. doi: 10.1021/ac5032379.

[135] Kentaro Shirai, Kazuma Mawatari, and Takehiko Kitamori. Extended nanofluidic immunochemical reaction with femtoliter sample volumes. *Small*, 10(8):1514–1522, 2014. ISSN 16136829. doi: 10.1002/smll.201302709.

[136] Stephanie Oyola-Reynoso, Andrew P. Heim, Julian Halbertsma-Black, C. Zhao, Ian D. Tevis, Simge Çinar, Rebecca Cademartiri, Xinyu Liu, Jean Francis Bloch, and Martin M. Thuo. Reprint of 'Draw your assay: Fabrication of low-cost paper-based diagnostic and multi-well test zones by drawing on a paper'. *Talanta*, 145:73–77, 2015. ISSN 00399140. doi: 10.1016/j.talanta.2015.09.042.

[137] Xuan Mu, Lin Zhang, Shaoying Chang, Wei Cui, and Zhi Zheng. Multiplex microfluidic paper-based immunoassay for the diagnosis of hepatitis C virus infection. *Analytical Chemistry*, 86(11):5338–5344, 2014. ISSN 15206882. doi: 10.1021/ac500247f.

[138] Yannick Rondelez, Guillaume Tresset, Kazuhito V Tabata, Hideyuki Arata, Hiroyuki Fujita, Shoji Takeuchi, and Hiroyuki Noji. Microfabricated arrays of femtoliter chambers allow single molecule enzymology. *Nature biotechnology*, 23(3):361–5, mar 2005. ISSN 1087-0156. doi: 10.1038/nbt1072. URL `http://www.ncbi.nlm.nih.gov/pubmed/15723045`.

[139] David M. Rissin and David R. Walt. Digital concentration readout of single enzyme molecules using femtoliter arrays and poisson statistics. *Nano Letters*, 6(3):520–523, mar 2006. ISSN 15306984. doi: 10.1021/nl060227d. URL `http://www.ncbi.nlm.nih.gov/pubmed/16522055`.

[140] Soo Hyeon Kim, Shino Iwai, Suguru Araki, Shouichi Sakakihara, Ryota Iino, and Hiroyuki Noji. Large-scale femtoliter droplet array for digital counting of single biomolecules. *Lab on a Chip*, 12(23):4986, dec 2012. ISSN 1473-0197. doi: 10.1039/c2lc40632b. URL `http://www.ncbi.nlm.nih.gov/pubmed/22961607`.

[141] Huaibin Zhang, Shuai Nie, Candice M. Etson, Raymond M. Wang, and David R. Walt. Oil-sealed femtoliter fiber-optic arrays for single molecule analysis. *Lab on a Chip*, 12(12):2229, jun 2012. ISSN 1473-0197. doi: 10.1039/c2lc21113k. URL `http://www.pubmedcentral.nih.gov/articlerender.fcgi?artid=3419529{&}tool=pmcentrez{&}rendertype=abstract`.

[142] Crispin Szydzik, Khashayar Khoshmanesh, Arnan Mitchell, and Christian Karnutsch. Microfluidic platform for separation and extraction of plasma from whole blood using dielectrophoresis. *Biomicrofluidics*, 9(6):1–16, 2015. ISSN 19321058. doi: 10.1063/1.4938391. URL `http://dx.doi.org/10.1063/1.4938391`.

[143] Francesca Volpetti, Jose Garcia-Cordero, and Sebastian J. Maerkl. A microfluidic platform for high-throughput multiplexed protein quantitation. *PLoS ONE*, 10(2), 2015. ISSN 19326203. doi: 10.1371/journal.pone.0117744.

[144] Dagan Zhang, Bingbing Gao, Yangtian Chen, and Hong Liu. Converting Colour to Length Based on Coffee-Ring Effect for Quantitative Immunoassays Using a Ruler as Readout. *Lab on a Chip*, 2017. ISSN 1473-0197. doi: 10.1039/C7LC01127J. URL `http://pubs.rsc.org/en/Content/ArticleLanding/2017/LC/C7LC01127J`.

[145] Hans H Gorris, David M Rissin, and David R Walt. Stochastic inhibitor release and binding from single-enzyme molecules. *Proceedings of the National Academy of Sciences of the United States of America*, 104(45):17680–17685, nov 2007. ISSN 0027-8424. doi: 10.1073/pnas.0705411104. URL `http://www.pubmedcentral.nih.gov/articlerender.fcgi?artid=2077050{&}tool=pmcentrez{&}rendertype=abstract`.

[146] Hans H Gorris and David R Walt. Mechanistic aspects of horseradish peroxidase elucidated through single-molecule studies. *Journal of the American Chemical Society*, 131(17):6277–82, may 2009. ISSN 1520-5126. doi: 10.1021/ja9008858. URL `http://pubs.acs.org/doi/abs/10.1021/ja9008858{%}5Cnhttp://www.ncbi.nlm.nih.gov/pubmed/19338338`.

[147] Lei Chang, David M Rissin, David R Fournier, Tomasz Piech, Purvish P Patel, David H. Wilson, and David C Duffy. Single molecule enzyme-linked immunosorbent assays: Theoretical considerations. *Journal of Immunological Methods*, 378(1-2):102–115, apr 2012. ISSN 00221759. doi: 10.1016/j.jim.2012.02.011. URL `http://linkinghub.elsevier.com/retrieve/pii/S0022175912000464`.

[148] Fabienne Courtois, Luis F. Olguin, Graeme Whyte, Ashleigh B. Theberge, Wilhelm T S Huck, Florian Hollfelder, and Chris Abell. Controlling the retention of small molecules in emulsion microdroplets for use in cell-based assays. *Analytical Chemistry*, 81(8):3008–3016, 2009. ISSN 00032700. doi: 10.1021/ac802658n.

[149] Sanchia S Goonewardene, Jaspal S Phull, Amit Bahl, and Raj A Persad. Interpretation of PSA levels after radical therapy for prostate cancer. *Trends in Urology & Men's Health*, 5(4):30–34, 2014. URL `http://10.0.3.234/tre.407{%}0Ahttp://search.ebscohost.com/login.aspx?direct=true{&}db=a9h{&}AN=97193612{&}site=ehost-live`.

[150] John R Prensner, Mark A Rubin, John T Wei, and Arul M Chinnaiyan. Beyond PSA: The Next Generation of Prostate Cancer Biomarkers. *Science Translational Medicine*, 4(127):127rv3–127rv3, 2012. ISSN 1946-6234. doi: 10.1126/scitranslmed.3003180. URL http://www.ncbi.nlm.nih.gov/pubmed/22461644{%}5Cnhttp://www.pubmedcentral.nih.gov/articlerender.fcgi?artid=PMC3799996http://stm.sciencemag.org/cgi/doi/10.1126/scitranslmed.3003180.

[151] David A. Giljohann and Chad A. Mirkin. Drivers of biodiagnostic development. *Nature*, 462(7272):461–464, 2009. ISSN 00280836. doi: 10.1038/nature08605.

[152] Charles R Pound, Alan W Partin, Mario A Eisenberger, Daniel W Chan, Jay D Pearson, and Patrick C Walsh. Natural History of Progression After PSA. *Journal of the American Medical Association*, 281(17):1591–1597, 1999. ISSN 0098-7484. doi: 10.1001/jama.281.17.1591.

[153] Daan Witters, Karel Knez, Frederik Ceyssens, Robert Puers, and Jeroen Lammertyn. Digital microfluidics-enabled single-molecule detection by printing and sealing single magnetic beads in femtoliter droplets. *Lab on a Chip*, 13(11):2047, jun 2013. ISSN 1473-0197. doi: 10.1039/c3lc50119a. URL http://xlink.rsc.org/?DOI=c3lc50119a.

[154] Khayriyyah Mohd Hanafiah, Norsyahida Arifin, Yazmin Bustami, Rahmah Noordin, Mary Garcia, and David Anderson. Development of Multiplexed Infectious Disease Lateral Flow Assays: Challenges and Opportunities. *Diagnostics*, 7(3):51, 2017. ISSN 2075-4418. doi: 10.3390/diagnostics7030051. URL http://www.mdpi.com/2075-4418/7/3/51.

[155] Younghoon Song, Yunjin Jeong, Taehong Kwon, Daewon Lee, Dong Yoon Oh, Tae-Joon Park, Junhoi Kim, Jiyun Kim, and Sunghoon Kwon. Liquid-capped encoded microcapsules for multiplex assays. *Lab Chip*, 17(3):429–437, 2017. ISSN 1473-0197. doi: 10.1039/C6LC01268J. URL http://xlink.rsc.org/?DOI=C6LC01268J.

[156] T. I. Godjevargova, Y. L. Ivanov, and D. D. Dinev. Multiplex fluorescent immunoassay device based on magnetic nanoparticles. 020018:020018, 2017. doi: 10.1063/1.4975433. URL http://aip.scitation.org/doi/abs/10.1063/1.4975433.

[157] Bong Hyun Jun, Jong Ho Kim, Hyunmi Park, Jun Sung Kim, Kyeong Nam Yu, Sang Myung Lee, Heejeong Choi, Seon Yeong Kwak, Yong Kweon Kim, Dae Hong Jeong, Myung Haing Cho, and Yoon Sik Lee. Surface-enhanced Raman spectroscopic-encoded beads for multiplex immunoassay. *Journal of Combinatorial Chemistry*, 9(2):237–244, 2007. ISSN 15204766. doi: 10.1021/cc0600831. URL http://pubs.acs.org/doi/abs/10.1021/cc0600831.

[158] David M. Rissin, Cheuk W. Kan, Linan Song, Andrew J. Rivnak, Matthew W. Fishburn, Qichao Shao, Tomasz Piech, Evan P. Ferrell, Raymond E. Meyer, Todd G. Campbell, David R. Fournier, and David C. Duffy. Multiplexed single molecule immunoassays. *Lab on a Chip*, 13(15):2902, 2013. ISSN 1473-0197. doi: 10.1039/c3lc50416f. URL http://xlink.rsc.org/?DOI=c3lc50416f.

[159] Chad Brocker, David Thompson, Akiko Matsumoto, Daniel W. Nebert, and Vasilis Vasiliou. Evolutionary divergence and functions of the human interleukin (IL) gene family. *Human Genomics*, 5(1):30–55, 2010. ISSN 14797364. doi: 10.1186/1479-7364-5-1-30.

[160] David H. Wilson, David M. Rissin, Cheuk W. Kan, David R. Fournier, Tomasz Piech, Todd G. Campbell, Raymond E. Meyer, Matthew W. Fishburn, Carlos Cabrera, Purvish P. Patel, Erica Frew, Yao Chen, Lei Chang, Evan P. Ferrell, Volker von Einem, William McGuigan, Marcus Reinhardt, Heiko Sayer, Claus Vielsack, and David C. Duffy. The Simoa HD-1 Analyzer. *Journal of Laboratory Automation*, 21(4):533–547, aug 2016. ISSN 2211-0682. doi: 10.1177/2211068215589580. URL http://journals.sagepub.com/doi/10.1177/2211068215589580.

[161] David M. Rissin and David R. Walt. Digital readout of target binding with attomole detection limits via enzyme amplification in femtoliter arrays. *Journal of the American Chemical Society*, 128(19):6286–6287, may 2006. ISSN 00027863. doi: 10.1021/ja058425e. URL http://www.ncbi.nlm.nih.gov/pubmed/16683771.

[162] Jong Wook Hong and Stephen R. Quake. Integrated nanoliter systems. *Nature Biotechnology*, 21(10):1179–1183, 2003. ISSN 10870156. doi: 10.1038/nbt871.

[163] S. Singh, N. Kumar, D. George, and A. K. Sen. Analytical modeling, simulations and experimental studies of a PZT actuated planar valveless PDMS micropump. *Sensors and Actuators, A: Physical*, 225:81–94, 2015. ISSN 09244247. doi: 10.1016/j.sna.2015.02.012. URL http://dx.doi.org/10.1016/j.sna.2015.02.012.

[164] Chun Hong Lee, Suz Kai Hsiung, and Gwo Bin Lee. A tunable microflow focusing device utilizing controllable moving walls and its applications for formation of micro-droplets in liquids. *Journal of Micromechanics and Microengineering*, 17(6):1121–1129, 2007. ISSN 09601317. doi: 10.1088/0960-1317/17/6/004.

[165] Yen Heng Lin, Chun Hong Lee, and Gwo Bin Lee. Droplet formation utilizing controllable moving-wall structures for double-emulsion applications. *Journal of Microelectromechanical Systems*, 17(3):573–581, 2008. ISSN 10577157. doi: 10.1109/JMEMS.2008.924273.

[166] Ascher H. Shapiro. Steady Flow in Collapsible Tubes, 1977. ISSN 01480731. URL http://biomechanical.asmedigitalcollection.asme.org/article.aspx?articleid=1393864.

[167] Dalin Tang, Chun Yang, Shunichi Kobayashi, and David N. Ku. Experiment-based numerical simulation of unsteady viscous flow in stenotic collapsible tubes. *Applied Numerical Mathematics*, 36(2-3):299–320, 2001. ISSN 01689274. doi: 10.1016/S0168-9274(00)00012-X.

[168] Matthew A. Holden, Saurabh Kumar, Ali Beskok, and Paul S. Cremer. Microfluidic diffusion diluter: Bulging of PDMS microchannels under pressure-driven flow. *Journal of Micromechanics and Microengineering*, 13(3):412–418, 2003. ISSN 09601317. doi: 10.1088/0960-1317/13/3/309.

[169] Kazuo Hosokawa, Kotaro Hanada, and Ryutaro Maeda. A polydimethylsiloxane (PDMS) deformable diffraction grating for monitoring of local pressure in microfluidic devices. *Journal of Micromechanics and Microengineering*, 12(1):1–6, 2002. ISSN 09601317. doi: 10.1088/0960-1317/12/1/301.

[170] Thomas Gervais, Jamil El-Ali, Axel Günther, and Klavs F Jensen. Flow-induced deformation of shallow microfluidic channels. *Lab on a chip*, 6(4):500–7, 2006. ISSN 1473-0197. doi: 10.1039/b513524a. URL `http://pubs.rsc.org.globalproxy.cvt.dk/en/content/articlehtml/2006/lc/b513524a`.

[171] Fabiana S. Felix and Lúcio Angnes. Electrochemical Immunosensors a Powerful Tool for Analytical Applications. *Biosensors and Bioelectronics*, 2017. ISSN 09565663. doi: 10.1016/j.bios.2017.11.029. URL `http://linkinghub.elsevier.com/retrieve/pii/S0956566317307583`.

[172] Brian S Hardy, Kawika Uechi, Janet Zhen, and H Pirouz Kavehpour. The deformation of flexible PDMS microchannels under a pressure driven flow. *Lab on a chip*, 9(7):935–938, 2009. ISSN 1473-0197. doi: 10.1039/b813061b. URL `http://xlink.rsc.org/?DOI=B813061B`.

[173] Ivan C. Christov, Vincent Cognet, Tanmay C. Shidhore, and Howard A. Stone. Flow ratepressure drop relation for deformable shallow microfluidic channels. *Journal of Fluid Mechanics*, 841: 267–286, apr 2018. ISSN 0022-1120. doi: 10.1017/jfm.2018.30. URL `http://arxiv.org/abs/1712.02687{%}0Ahttp://dx.doi.org/10.1017/jfm.2018.30https://www.cambridge.org/core/product/identifier/S0022112018000307/type/journal{_}article`.

[174] Perry Cheung, Kazumi Toda-Peters, and Amy Q. Shen. In situ pressure measurement within deformable rectangular polydimethylsiloxane microfluidic devices. *Biomicrofluidics*, 6(2):026501, 2012. ISSN 19321058. doi: 10.1063/1.4720394.

[175] A. Raj and A. K. Sen. Flow-induced deformation of compliant microchannels and its effect on pressureflow characteristics. *Microfluidics and Nanofluidics*, 20(2):1–13, 2016. ISSN 16134990. doi: 10.1007/s10404-016-1702-9.

[176] CM Pandey, Shine Augustine, Suveen Kumar, Suveen Kumar, Sharda Nara, Saurabh Srivastava, and BD Malhotra. Microfluidics Based Point-of-Care Diagnostics. *Biotechnology Journal*, pages 1–31, nov 2017. ISSN 18606768. doi: 10.1002/biot.201700047. URL http://doi.wiley.com/10.1002/biot.201700047.

[177] Michael W. Toepke and David J. Beebe. PDMS absorption of small molecules and consequences in microfluidic applications. *Lab on a Chip*, 6(12):1484, 2006. ISSN 1473-0197. doi: 10.1039/b612140c. URL http://xlink.rsc.org/?DOI=b612140c.

[178] Jack D. Wang, Nicholas J. Douville, Shuichi Takayama, and Mohamed Elsayed. Quantitative analysis of molecular absorption into PDMS microfluidic channels. *Annals of Biomedical Engineering*, 40(9):1862–1873, 2012. ISSN 00906964. doi: 10.1007/s10439-012-0562-z.

[179] P Menter. Acrylamide PolymerizationA Practical Approach. *Bio-Rad Tech Note*, page 1156, 2000. URL http://scholar.google.com/scholar?hl=en{&}btnG=Search{&}q=intitle:Acrylamide+Polymerization+?+A+Practical+Approach{#}0.

[180] Sebastian Seiffert and David A. Weitz. Microfluidic fabrication of smart microgels from macromolecular precursors. *Polymer*, 51(25):5883–5889, 2010. ISSN 00323861. doi: 10.1016/j.polymer.2010.10.034. URL http://dx.doi.org/10.1016/j.polymer.2010.10.034.

[181] Fei Chen, Paul W Tillberg, and Edward S Boyden. Expansion microscopy. *Science*, 347(6221):543–548, jan 2015. ISSN 0036-8075. doi: 10.1126/science.1260088. URL http://www.ncbi.nlm.nih.gov/pubmed/25592419http://www.pubmedcentral.nih.gov/articlerender.fcgi?artid=PMC4312537http://www.sciencemag.org/cgi/doi/10.1126/science.1260088.

[182] Laura MacDonald, Giulia Baldini, and Brian Storrie. Does Super-Resolution Fluorescence Microscopy Obsolete Previous Microscopic Approaches to Protein Co-localization? volume 1270 of *Methods in Molecular Biology*, pages 255–275. Springer New York, New York, NY, 2015. ISBN 978-1-4939-2308-3. doi: 10.1007/978-1-4939-2309-0_19. URL http://link.springer.com/10.1007/978-1-4939-2309-0http://link.springer.com/10.1007/978-1-4939-2309-0{_}19.

[183] Ralf Jungmann, Maier S Avendaño, Johannes B Woehrstein, Mingjie Dai, William M Shih, and Peng Yin. Multiplexed 3D cellular super-resolution imaging with DNA-PAINT and Exchange-PAINT. *Nature Methods*, 11 (3):313–318, 2014. ISSN 1548-7091. doi: 10.1038/nmeth.2835. URL http://www.nature.com/doifinder/10.1038/nmeth.2835.

[184] Joerg Schnitzbauer, Maximilian T Strauss, Thomas Schlichthaerle, Florian Schueder, and Ralf Jungmann. Super-resolution microscopy with

DNA-PAINT. *Nature Protocols*, 12(6):1198–1228, 2017. ISSN 1754-2189. doi: 10.1038/nprot.2017.024. URL http://www.nature.com/doifinder/10.1038/nprot.2017.024.

[185] Paul W Tillberg, Fei Chen, Kiryl D Piatkevich, Yongxin Zhao, Chih-Chieh (Jay) Yu, Brian P English, Linyi Gao, Anthony Martorell, Ho-Jun Suk, Fumiaki Yoshida, Ellen M DeGennaro, Douglas H Roossien, Guanyu Gong, Uthpala Seneviratne, Steven R Tannenbaum, Robert Desimone, Dawen Cai, and Edward S Boyden. Protein-retention expansion microscopy of cells and tissues labeled using standard fluorescent proteins and antibodies. *Nature Biotechnology*, 34(9):987–992, jul 2016. ISSN 1087-0156. doi: 10.1038/nbt.3625. URL http://www.nature.com/doifinder/10.1038/nbt.3625.

[186] Yufeng Hou, Isuru Jayasinghe, David J. Crossman, David Baddeley, and Christian Soeller. Nanoscale analysis of ryanodine receptor clusters in dyadic couplings of rat cardiac myocytes. *Journal of Molecular and Cellular Cardiology*, 80:45–55, 2015. ISSN 10958584. doi: 10.1016/j.yjmcc.2014.12.013. URL http://dx.doi.org/10.1016/j.yjmcc.2014.12.013.

[187] Isuru Jayasinghe, Alexander H. Clowsley, Ruisheng Lin, Tobias Lutz, Carl Harrison, Ellen Green, David Baddeley, Lorenzo Di Michele, and Christian Soeller. True Molecular Scale Visualization of Variable Clustering Properties of Ryanodine Receptors. *Cell Reports*, 22(2):557–567, 2018. ISSN 22111247. doi: 10.1016/j.celrep.2017.12.045. URL https://doi.org/10.1016/j.celrep.2017.12.045.

[188] Tanya R. Cully, Robyn M. Murphy, Llion Roberts, Truls Raastad, Robert G. Fassett, Jeff S. Coombes, Isuru D. Jayasinghe, and Bradley S. Launikonis. Human skeletal muscle plasmalemma alters its structure to change its Ca2+-handling following heavy-load resistance exercise. *Nature Communications*, 8:1–10, 2017. ISSN 20411723. doi: 10.1038/ncomms14266. URL http://dx.doi.org/10.1038/ncomms14266.

[189] Sven Truckenbrodt, Manuel Maidorn, Dagmar Crzan, Hanna Wildhagen, Selda Kabatas, and Silvio O Rizzoli. X10 expansion microscopy enables 25nm resolution on conventional microscopes. *EMBO reports*, 19 (9):e45836, 2018. ISSN 1469-221X. doi: 10.15252/embr.201845836.

[190] Venkata R. Yelleswarapu, Heon-Ho Jeong, Sagar Yadavali, and David Issadore. Ultra-high throughput detection (1 million droplets per second) of fluorescent droplets using a cell phone camera and time domain encoded optofluidics. *Lab Chip*, 2017. ISSN 1473-0197. doi: 10.1039/C6LC01489E. URL http://pubs.rsc.org/en/Content/ArticleLanding/2017/LC/C6LC01489Ehttp://xlink.rsc.org/?DOI=C6LC01489E.

[191] Kwi Nam Han, Cheng Ai Li, and Gi Hun Seong. Microfluidic chips for immunoassays. *Annu. Rev. Anal. Chem.*, 6(1):119–141, 2013. ISSN

1936-1335. doi: 10.1146/annurev-anchem-062012-092616. URL http://www.ncbi.nlm.nih.gov/pubmed/23495732.

[192] Skarphedinn Halldorsson, Edinson Lucumi, Rafael Gómez-Sjöberg, and Ronan M.T. Fleming. Advantages and challenges of microfluidic cell culture in polydimethylsiloxane devices. *Biosensors and Bioelectronics*, 63: 218–231, 2015. ISSN 18734235. doi: 10.1016/j.bios.2014.07.029. URL http://dx.doi.org/10.1016/j.bios.2014.07.029.

[193] Kimberly L. Berkowski, Kyle N. Plunkett, Qing Yu, and Jeffrey S. Moore. Introduction to Photolithography: Preparation of Microscale Polymer Silhouettes. *Journal of Chemical Education*, 82(9):1365, 2005. ISSN 0021-9584. doi: 10.1021/ed082p1365. URL http://pubs.acs.org/doi/abs/10.1021/ed082p1365.

[194] John L. Dektar and Nigel P. Hacker. Photochemistry of Triarylsulfonium Salts. *Journal of the American Chemical Society*, 112(16):6004–6015, 1990. ISSN 15205126. doi: 10.1021/ja00172a015.

[195] Daisuke Morita, Masashi Yamamoto, Kazuyuki Akaishi, Kousuke Matoba, Katsuhiro Yasutomo, Yoshio Kasai, Masahiko Sano, Shin Ichi Nagahama, and Takashi Mukai. Watt-class high-output-power 365 nm ultraviolet light-emitting diodes. *Japanese Journal of Applied Physics, Part 1: Regular Papers and Short Notes and Review Papers*, 43(9 A):5945–5950, 2004. ISSN 00214922. doi: 10.1143/JJAP.43.5945.

[196] Ph Wägli, B Y Guélat, A Homsy, and N F De Rooij. Microfluidic devices made of UV-curable glue (NOA81) for fluorescence detection based applications. *Proceeding of the 14th International Conference on Miniaturized Systems for Chemistry and Life Sciences (microTAS)*, (October): 1937–1939, 2010.

[197] M R Eftink. *Fluorescence Techniques for Studying Protein Structure*, volume 35. 2006. ISBN 0471513261. doi: 10.1002/9780470110560. URL http://www.ncbi.nlm.nih.gov/entrez/query.fcgi?cmd=Retrieve{&}db=PubMed{&}dopt=Citation{&}list{_}uids=2002770.

[198] Peter (Peter J.) Larkin. *Infrared and raman spectroscopy : principles and spectral interpretation*. Elsevier, 2011. ISBN 9780123869845.

[199] Daniel Hoffman. *Measuring the elastic modulus of polymers using the atomic force microscope*. PhD thesis, Michigan Technological University, 2010. URL https://digitalcommons.mtu.edu/cgi/viewcontent.cgi?article=1026{&}context=etds.

[200] B. Poon, D. Rittel, and G. Ravichandran. An analysis of nanoindentation in linearly elastic solids. *International Journal of Solids and Structures*, 45 (24):6018–6033, 2008. ISSN 00207683. doi: 10.1016/j.ijsolstr.2008.07.021. URL http://dx.doi.org/10.1016/j.ijsolstr.2008.07.021.

[201] D Tranchida, Z Kiflie, and S Piccarolo. Atomic force microscope nanoindentations to reliably measure the Young's modulus of soft matter. *Modern Research and Educational*, pages 1–10, 2007.

[202] R. Ferencz, J. Sanchez, B. Blümich, and W. Herrmann. AFM nanoindentation to determine Young's modulus for different EPDM elastomers. *Polymer Testing*, 31(3):425–432, 2012. ISSN 01429418. doi: 10.1016/j.polymertesting.2012.01.003. URL `http://dx.doi.org/10.1016/j.polymertesting.2012.01.003`.

[203] I. D. Johnston, D. K. McCluskey, C. K.L. Tan, and M. C. Tracey. Mechanical characterization of bulk Sylgard 184 for microfluidics and microengineering, 2014. ISSN 13616439.

[204] Rerngchai Arayanarakool, Lingling Shui, Servé W M Kengen, Albert van den Berg, and Jan C T Eijkel. Single-enzyme analysis in a droplet-based micro- and nanofluidic system. *Lab on a chip*, 13(10):1955–62, may 2013. ISSN 1473-0189. doi: 10.1039/c3lc41100a. URL `http://www.ncbi.nlm.nih.gov/pubmed/23546540`.

[205] Z J Huang. Kinetic fluorescence measurement of fluorescein di-beta-D-galactoside hydrolysis by beta-galactosidase: intermediate channeling in stepwise catalysis by a free single enzyme. *Biochemistry*, 30:8535–8540, 1991. ISSN 0006-2960. doi: 10.1021/bi00099a006.

[206] Franz FIEDLER and Heide HINZ. No intermediate channelling in stepwise hydrolysis of fluorescein di-beta-D-galactoside by beta-galactosidase. *European Journal of Biochemistry*, 222(1):75–81, may 1994. ISSN 0014-2956. doi: 10.1111/j.1432-1033.1994.tb18843.x. URL `http://doi.wiley.com/10.1111/j.1432-1033.1994.tb18843.x`.

[207] David M. Rissin, Hans H. Gorris, and David R. Walt. Distinct and long-lived activity states of single enzyme molecules. *Journal of the American Chemical Society*, 130(15):5349–5353, apr 2008. ISSN 00027863. doi: 10.1021/ja711414f. URL `http://www.ncbi.nlm.nih.gov/pubmed/18318491`.

[208] Levent Yobas, Stefan Martens, Wee-Liat Ong, and Nagarajan Ranganathan. High-performance flow-focusing geometry for spontaneous generation of monodispersed droplets. *Lab on a chip*, 6(8):1073–1079, 2006. ISSN 1473-0197. doi: 10.1039/b602240e.

[209] Rémi Dangla, François Gallaire, and Charles N. Baroud. Microchannel deformations due to solvent-induced PDMS swelling. *Lab on a chip*, 10 (21):2972–2978, 2010. ISSN 1473-0197. doi: 10.1039/c003504a. URL `http://xlink.rsc.org/?DOI=c003504a`.

[210] Jessamine Ng Lee, Cheolmin Park, and George M. Whitesides. Solvent Compatibility of Poly(dimethylsiloxane)-Based Microfluidic Devices. *Analytical Chemistry*, 75(23):6544–6554, 2003. ISSN 00032700. doi: 10.1021/ac0346712. URL `http://pubs.acs.org/doi/abs/10.1021/ac0346712`.

[211] Patrick J. Tighe, Richard R. Ryder, Ian Todd, and Lucy C. Fairclough. ELISA in the multiplex era: Potentials and pitfalls. *Proteomics - Clinical Applications*, 9(3-4):406–422, 2015. ISSN 18628354. doi: 10.1002/prca.201400130.

[212] C. V. Rumens, M. A. Ziai, K. E. Belsey, J. C. Batchelor, and S. J. Holder. Swelling of PDMS networks in solvent vapours; applications for passive RFID wireless sensors. *J. Mater. Chem. C*, 3(39):10091–10098, sep 2015. ISSN 2050-7526. doi: 10.1039/C5TC01927C. URL `http://pubs.rsc.org/en/content/articlehtml/2015/tc/c5tc01927c`.